The type IIb SN 2011dh - 2 years of observations and modelling of the bolometric and photometric lightcurves.

M. Ergon[1], A. Jerkstrand[2], J. Sollerman[1], N. Elias-Rosa[3], C. Fransson[1], M. Fraser[4,2], A. Pastorello[3], R. Kotak[2], S. Taubenberger[5], L. Tomasella[3], S. Valenti[6,7], S. Benetti[3], G. Helou[8], M.M. Kasliwal[9], S.J. Smartt[2], and J. Spyromilio[10]

[1] The Oskar Klein Centre, Department of Astronomy, AlbaNova, Stockholm University, 106 91 Stockholm, Sweden
[2] Astrophysics Research Centre, School of Mathematics and Physics, Queens University Belfast, Belfast, BT7 1NN, UK
[3] INAF, Osservatorio Astronomico di Padova, vicolo dell'Osservatorio n. 5, 35122 Padua, Italy
[4] Institute of Astronomy, University of Cambridge, Madingley Road, Cambridge, CB3 0HA
[5] Max-Planck-Institut für Astrophysik, Karl-Schwarzschild-Str. 1, D-85741 Garching, Germany
[6] Las Cumbres Observatory Global Telescope Network, 6740 Cortona Dr., Suite 102, Goleta, CA 93117, USA
[7] Department of Physics, University of California, Santa Barbara, Broida Hall, Mail Code 9530, Santa Barbara, CA 93106-9530, USA
[8] Infrared Processing and Analysis Center, California Institute of Technology, Pasadena, CA 91125, USA
[9] Observatories of the Carnegie Institution for Science, 813 Santa Barbara St, Pasadena, CA 91101, USA
[10] ESO, Karl-Schwarzschild-Strasse 2, 85748 Garching, Germany

ABSTRACT

We present optical and near-infrared (NIR) photometry and spectroscopy as well as modelling of the lightcurves of the Type IIb supernova (SN) 2011dh. The dataset spans 2 years and complemented with Spitzer mid-infrared (MIR) data we use it to build a 3-732 days optical to MIR bolometric lightcurve, although the absence of near-infrared (NIR) observations after 380 days adds uncertainty during the second year. To model the <100 days bolometric lightcurves we use a hydrodynamical model grid, which allows us to determine the errors in the derived quantities. To extend the coverage of the model grid to 400 days, we use a bolometric correction determined with steady-state NLTE modelling. We obtain almost identical results using the <100 and <400 days bolometric lightcurves and find a helium core mass of $3.4^{+0.6}_{-0.3}$ $M_\odot$ for SN 2011dh. Similar values are obtained for SNe 1993J and 2008ax using their <100 days bolometric lightcurves. We present 100-500 days bolometric and photometric lightcurves for the Jerkstrand et al. (2014) steady-state NLTE models and discuss the constraints derived from the those on the model parameters. The optimal 12 $M_\odot$ model, presented and found to give a good agreement with observed nebular spectra in Jerkstrand et al. (2014), shows a good overall agreement with the observed lightcurves, although some discrepancies exist. Time-dependent NLTE modelling shows that after 600 days a steady-state assumption is no longer valid. The radioactive energy deposition in this phase is likely dominated by the positrons emitted in the decay of ^{56}Co but what energy source is dominating the emitted flux is unclear. We find an excess in the K band and the MIR developing between 100 and 250 days, during which an increase in the optical tail decline rate is also observed. Steady-state NLTE models with a modest dust opacity in the core ($\tau = 0.44$), turned on during this period, reproduce the observed behaviour. The depth of the He I 20581 Å absorption suggest the emission to arise from within ~10000 km s^{-1}. A modest amount of CO first overtone band emission is detected at 206 days implying a contribution to the Spitzer 4.5 μm band from CO fundamental band emission. Examining the steady-state NLTE models neither complete CO cooling nor absence of CO cooling in the C/O zone well reproduce the observed Spitzer 4.5 μm flux, suggesting an intermediate scenario. Estimates of the sizes of the line emitting regions, ranging from ~3000 km s^{-1} for the oxygen lines to ~1500 km s^{-1} for the iron lines, suggest incomplete mixing of the nuclear burning zones. The profiles of the [O I] 6300 Å and Mg I] 4571 Å lines show a remarkable similarity, suggesting these lines to be emitted by the same material and to originate from the O/Ne/Mg zone. We use small scale fluctuations in the [O I] 6300 Å and Mg I] 4571 Å lines to estimate a filling factor of $\lesssim$0.07 for this material. This paper concludes our extensive observational and modelling work on SN 2011dh. The results from hydrodynamical modelling, steady-state NLTE modelling and stellar evolutionary progenitor analysis are all consistent and suggest an initial mass of ~13 $M_\odot$ for the progenitor. The initial masses of $\lesssim$15 $M_\odot$ found for SNe 2011dh, 1993J and 2008ax, by hydrodynamical modelling and steady-state NLTE modelling, suggest that all of these Type IIb SNe originates from binary systems, as previously established for SN 1993J.

Key words. supernovae: general — supernovae: individual (SN 2011dh) — supernovae: individual (SN 1993J) — supernovae: individual (SN 2008ax) — galaxies: individual (M51)

1. Introduction

Type IIb supernovae (SNe) are observationally characterized by a transition from Type II (with hydrogen lines) at early times to Type Ib (without hydrogen lines but with helium lines) at later times. The physical interpretation is that these SNe arise from stars that have lost most of their hydrogen envelope, either through stellar winds or interaction with a binary companion. Which of these production channels dominates is still debated but for SN 1993J, the prime example of such a SN, a companion star was detected by direct observations (Maund et al. 2004;

Fox et al. 2014). The evolution of this binary system has been successfully modelled (Podsiadlowski et al. 1993; Stancliffe & Eldridge 2009) and it is widely accepted that the companion was responsible for the removal of the hydrogen envelope. Bright, nearby Type IIb SNe as 1993J, 2008ax and the recent 2011dh are essential to improve our understanding of this class. Observations of the progenitor star in pre-explosion images, a search for the companion star when the SN has faded and multi-method modelling of high quality data, all provide important clues to the nature of Type IIb SNe and their progenitor stars.

In this paper we present an extensive optical and near-infrared (NIR) dataset, covering nearly two years, that we have obtained for SN 2011dh. The first 100 days of this dataset have been presented in Ergon et al. (2014a, hereafter E14a). Detailed hydrodynamical modelling of the SN using those data were presented in Bersten et al. (2012, hereafter B12) and steady-state NLTE modelling of nebular spectra in Jerkstrand et al. (2014, hereafter J14). Identification and analysis of the plausible progenitor star was presented in Maund et al. (2011, hereafter M11) and confirmation of the progenitor identification through its disappearance in E14a.

SN 2011dh was discovered on 2011 May 31.893 UT (Griga et al. 2011; Arcavi et al. 2011) in the nearby galaxy M51 at a distance of 7.8 Mpc (E14a). The SN has been extensively monitored from X-ray to radio wavelengths by several teams. Most observations cover the 3-100 days period, but late time data have been published in Tsvetkov et al. (2012), Van Dyk et al. (2013), Sahu et al. (2013), Shivvers et al. (2013) and Helou et al. (2013). As in E14a we focus on the ultra-violet (UV) to mid-infrared (MIR) emission. The explosion epoch (May 31.5 UT), the distance to M51 ($7.8^{+1.1}_{-0.9}$ Mpc) and the interstellar line-of-sight extinction towards the SN ($E(B-V)=0.07^{+0.07}_{-0.04}$ mag) used in this paper, are all adopted from E14a. The phase of the SN is expressed relative to this explosion epoch throughout the paper.

The nature of the progenitor star has been a key issue since the identification of a yellow supergiant in pre-explosion images, coincident with the SN (M11; Van Dyk et al. 2011). Recent progress in modelling of the SN (B12; J14; Shivvers et al. 2013) and the disappearance of the progenitor candidate (E14a; Van Dyk et al. 2013) strengthens the hypothesis that the progenitor was a yellow supergiant of moderate mass, as was originally proposed in M11. In this paper we present further modelling in support of this hypothesis. As shown in Benvenuto et al. (2013) a binary interaction scenario that reproduces the observed and modelled properties of the yellow supergiant is possible. Hubble Space Telescope (HST) observations that could detect or set useful constraints on the presence of a companion star are scheduled for Cycle 21.

The paper is organized as follows. In Sect. 2 and 3 we present and and analyse our photometric and spectroscopic observations, respectively, and compare these to SNe 1993J and 2008ax. In Sect. 4 we model the lightcurves and in Sect. 5 we discuss the MIR evolution, our results on the nature of the progenitor star and the implication of these on our understanding of Type IIb SNe. Finally, we conclude and summarize our results in Sect. 6.

2. Photometry

In E14a we presented our <100 days observations and analysis and comparison to SNe 1993J and 2008ax. Here we present further observations spanning 100-732 days in the optical, 100-380 days in the NIR and 100-1061 days in the MIR, and a continuation of the analysis and the comparison, focusing on the >100

days data. Hydrodynamical and steady-state NLTE modelling of these data are presented in Sect. 4. As discussed in E14a, the systematic errors stemming from the uncertainties in distance and extinction are large for all three SNe, which should be kept in mind when absolute quantities are compared. For SNe 1993J and 2008ax we adopt the same values and error bars for the distance and extinction as in E14a. The references for the photometric data of SNe 1993J and 2008ax used in the comparison are the same as specified in E14a. We note that the lack of S-corrected photometry for SN 1993J complicates the comparison, whereas for SN 2008ax the S-corrected JC photometry by Taubenberger et al. (2011) agrees reasonably well with the JC photometry by Tsvetkov et al. (2009).

2.1. Observations

The >100 days data were obtained with the Liverpool Telescope (LT), the Nordic Optical Telescope (NOT), Telescopio Nazionale (TNG), the Calar Alto 3.5m (CA 3.5m) and 2.2m (CA 2.2m) telescopes, the Asiago 67/92cm Schmidt (AS Schmidt) and 1.82m Copernico (AS 1.82m) telescopes, the William Herschel Telescope (WHT), the Albanova Telescope[1] (AT) and the United Kingdom Infrared Telescope (UKIRT). The late time dataset includes 61 epochs of optical imaging and 9 epochs of NIR imaging which, together with the early time observations, gives a total of 146 epochs of optical imaging and 32 epochs of NIR imaging. Spitzer has systematically been observing SN2011dh under program ID 70207 (PI Helou), 90240 (PI Kasliwal) and 10136 (PI Kasliwal) and Helou et al. (2013) presented Spitzer photometry between 18 days to 625 days. E14a presented Spitzer photometry between 18 and 85 days (using an independent procedure) and in this paper we present observations up to 1061 days. Here and throughout the paper we label the Spitzer 3.6 μm and 4.5 μm bands S_1 and S_2, respectively. The reductions and calibration procedures used for the late time data are the same as in E14a and are described in detail therein, where we also provide a thorough discussion on the accuracy of the photometry. In Appendix A we discuss data reduction and calbration issues specifically related to the >100 days data.

The S-corrected optical and NIR magnitudes and their corresponding errors are listed in Tables 4, 5 and 6 and the Spitzer S_1 and S_2 magnitudes and their corresponding errors in Table 7. For completeness we also include the magnitudes for the first 100 days already published in E14a. The magnitudes for the <800 days period (excluding the ~1000 days Spitzer observations), including the SWIFT magnitudes published in E14a and S-corrected magnitudes for the HST observations published in Van Dyk et al. (2013), are shown in Fig. 1. We also show cubic spline fits using 3-5 point knot separation, error weighting and a 5 percent error floor or, when the sampling is sparse, linear interpolations as well as extrapolations assuming a constant colour to adjacent bands. The extrapolation method used makes some sense in early phases when the SED is dominated by the continuum but less so in late phases when it is dominated by lines, which should be kept in mind. All calculations in Sects. 2.2 and 2.3, are based on these spline fits, interpolations and extrapolations. In these calculations the errors in the fitted splines have been estimated as the standard deviation and then propagated.

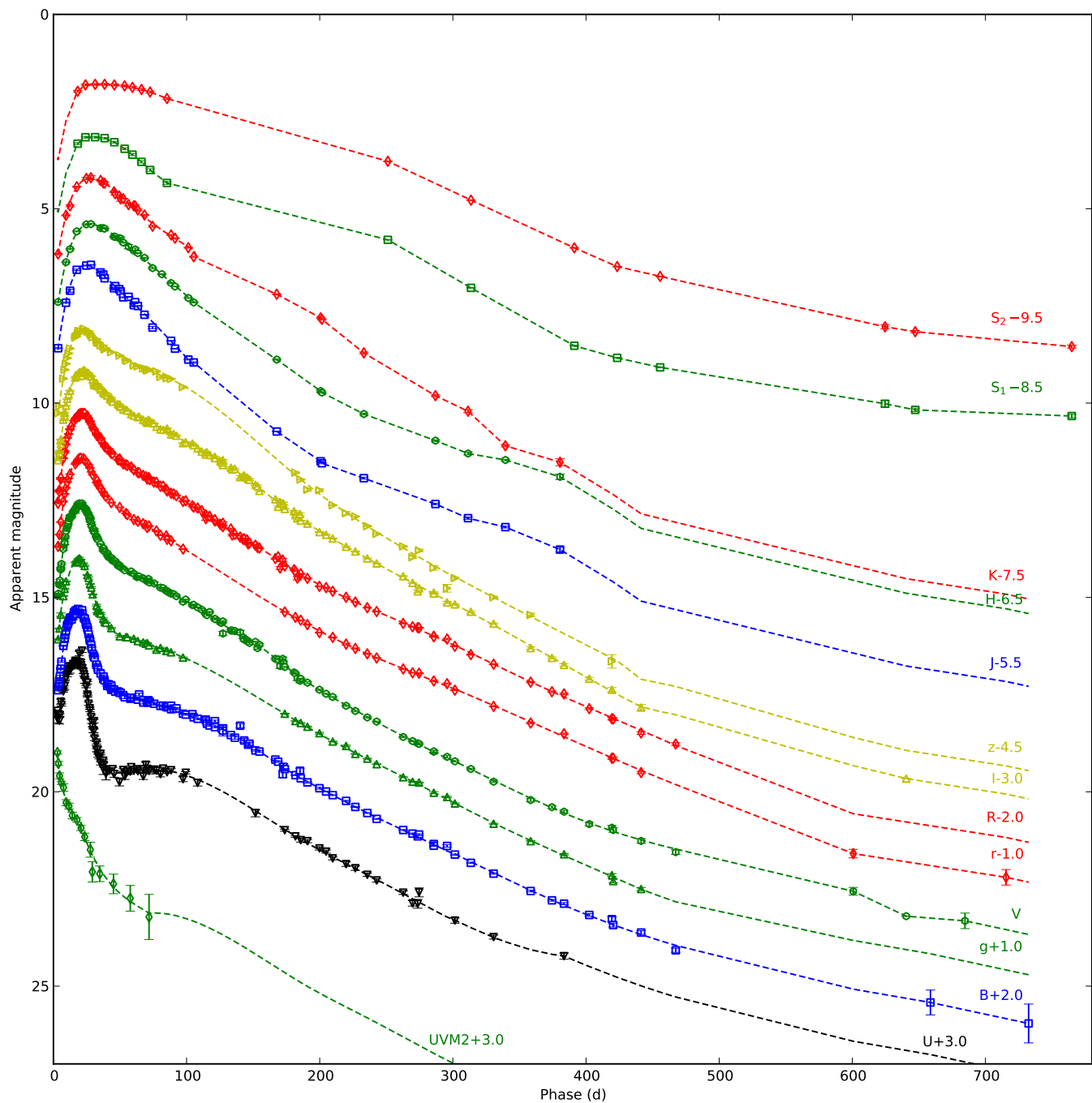[1] 1.0 m telescope at Albanova, Stockholm University.

Fig. 1. Photometric evolution of SN 2011dh in the UV, optical, NIR and MIR. For clarity each band has been shifted in magnitude. Each lightcurve has been annotated with the name of the band and the shift applied. We also show combinations of spline fits, interpolations and extrapolations described in Sect 2.1 (dashed lines).

2.2. Photometric evolution

In Fig. 2 we show absolute optical and NIR magnitudes for SN 2011dh as compared to SNe 1993J and 2008ax, and in Table 1 we tabulate the tail decline rates at 100, 200 and 300 days. Most striking is the similarity between the lightcurves, except for a shift towards higher luminosities for SNe 1993J and 2008ax, the shift being larger in bluer bands and negligible in the NIR and most pronounced for SN 2008ax. As discussed in E14a, this difference could be explained by errors in the adopted extinctions.

Given the caveat that SNe 1993J and 2008ax are only partly covered in *U* and NIR, we find the following general trends. At

100 days the *V*, *R* and *I* decline rates are roughly twice the decay rate of ^{56}Co, and subsequently decrease towards 300 days. The *U* and *B* decline rates are significantly lower at 100 days, subsequently approach the other optical decline rates and then evolve similarly. The *J* and *H* band decline rates are considerably higher than the optical at 100 days, subsequently approaches those and eventually become considerably lower. For SNe 2011dh and 1993J the *K* band behaves quite differently than the other NIR bands. At 100 days the decline rate is significantly lower, but as it remains roughly constant, it subsequently approaches the other NIR decline rates and eventually becomes
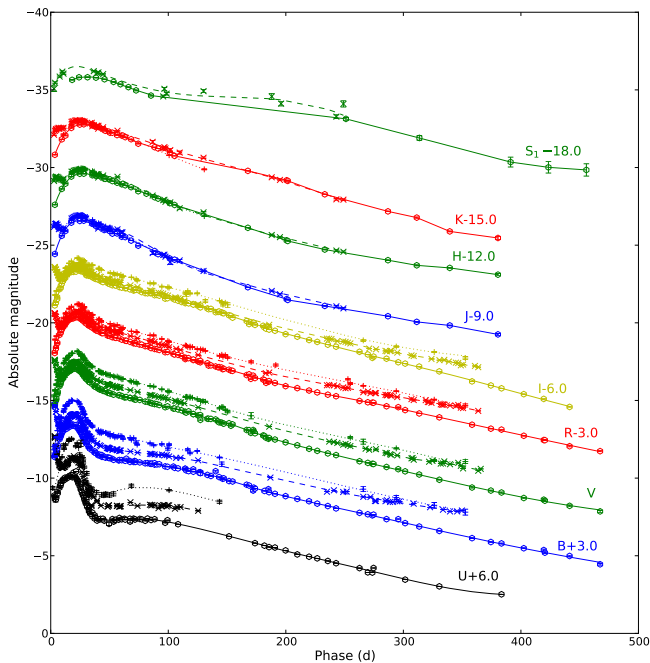
Fig. 2. Photometric evolution of SN 2011dh (dots) in the optical and NIR as compared to SNe 1993J (crosses) and 2008ax (pluses). For clarity each band has been shifted in magnitude. Each lightcurve has been annotated with the name of the band and the shift applied. We also show combinations of spline fits, interpolations and extrapolations described in Sect. 2.1 (dashed lines).

Table 1. Tail decline rates at 100, 200 and 300 days for SN 2011dh compared to SNe 1993J and 2008ax as measured from cubic spline fits.

SN	Band	Rate (100 d) (mag day^{-1})	Rate (200 d) (mag day^{-1})	Rate (300 d) (mag day^{-1})
2011dh	U	0.014	0.019	0.017
2011dh	B	0.014	0.019	0.017
2011dh	V	0.019	0.021	0.018
2011dh	R	0.021	0.018	0.016
2011dh	I	0.019	0.021	0.018
2011dh	J	0.036	0.018	0.011
2011dh	H	0.029	0.019	0.011
2011dh	K	0.020	0.020	0.024
1993J	U	0.006	...	...
1993J	B	0.011	0.017	0.012
1993J	V	0.019	0.019	0.017
1993J	R	0.022	0.015	0.013
1993J	I	0.022	0.019	0.013
1993J	J	0.041	0.016	...
1993J	H	0.033	0.018	...
1993J	K	0.023	0.022	...
2008ax	U	0.013	...	...
2008ax	B	0.015	0.018	0.016
2008ax	V	0.022	0.018	0.017
2008ax	R	0.023	0.016	0.015
2008ax	I	0.018	0.021	0.013
2008ax	J	0.035	...	...
2008ax	H	0.032	...	...
2008ax	K	0.033	...	...

considerably higher. As seen in Fig. 1, the optical lightcurves of SN 2011dh flatten considerably after ∼450 days, approaching a decline rate similar to, or lower than, the decay rate of ^{56}Co.

Both SNe 2011dh and 1993J were also monitored in the MIR, SN 2011dh in the S_1 and S_2 bands and SN 1993J in the L band, which is similar to the S_1 band. For both SNe a strong excess in the MIR develops between ∼100 and ∼250 days. For SN 1993J the MIR coverage ends at ∼250 days and for SN 2011dh the subsequent evolution is fairly similar to the evolution in the optical. After ∼400 days, a considerable flattening of the MIR lightcurves is seen, similar to, but more pronounced than the flattening of the optical lightcurves. After ∼750 days (not shown in Fig. 1) this trend continous and the MIR lighcurves becomes almost flat.

2.3. Bolometric evolution

As in E14a we have used a combination of the spectroscopic and photometric methods, applied to wavelength regions with and without spectral information respectively, when calculating the pseudo-bolometric lightcurves. The details of these methods have been described in E14a. Combinations of spline fits, interpolations and extrapolations, as described in Sect. 2.1 and shown in Figs. 1 and 2, have been used to calculate the magnitudes. Here and throughout the paper the wavelength regions over which the luminosity is integrated are specified as follows; UV (1900-3300 Å), optical (3300-10000 Å), NIR (10000-24000 Å) and MIR (24000-50000 Å).

Figure 3 shows the <500 days optical to NIR pseudo-bolometric lightcurves for SN 2011dh as compared to SNe 1993J and 2008ax as calculated with the photometric method, and in Table 2 we tabulate the decline rates at 100, 200 and 300 days. Given the caveat that SNe 1993J and 2008ax are not covered in

Table 2. Tail decline rates at 100, 200, and 300 days for the optical to NIR bolometric lightcurve of SN 2011dh compared to SNe 1993J and 2008ax.

SN	Rate (100 d) (mag day^{-1})	Rate (200 d) (mag day^{-1})	Rate (300 d) (mag day^{-1})
2011dh	0.021	0.021	0.017
2008ax	0.020	0.017	0.015
1993J	0.021	0.017	0.013

NIR after ∼250 and ∼150 days respectively, their optical to NIR pseudo-bolometric lightcurves are remarkably similar to the one of SN 2011dh, except for the shift towards higher luminosities discussed previously in Sect. 2.2. The decline rates decrease from ∼0.020 mag day^{-1}, roughly twice the decay rate of ^{56}Co, at 100 days to ∼0.015 mag day^{-1} at 300 days. There is however a significant increase in the decline rate between 150 and 200 days for SN 2011dh, even more pronounced in the optical pseudo-bolometric lightcurve, not seen for SNe 1993J and 2008ax. For SN 1993J the decline rate becomes increasingly lower towards 300 days as compared to SNe 2011dh and 2008ax, which is consistent with an increasing contribution from CSM interaction in this phase.
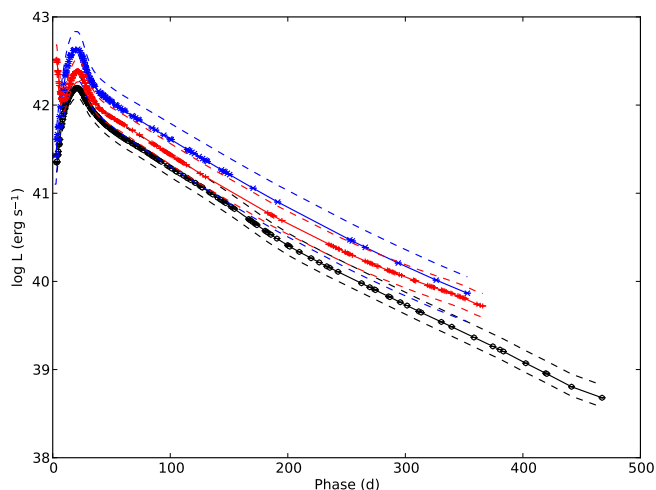
Fig. 3. Optical to NIR pseudo-bolometric lightcurve for SN 2011dh (black circles and solid line) calculated with the photometric method as compared to SNe 1993J (red crosses and solid line) and 2008ax (blue pluses and solid line). The upper and lower error bars for the systematic error arising from extinction and distance (dashed lines) are also shown.
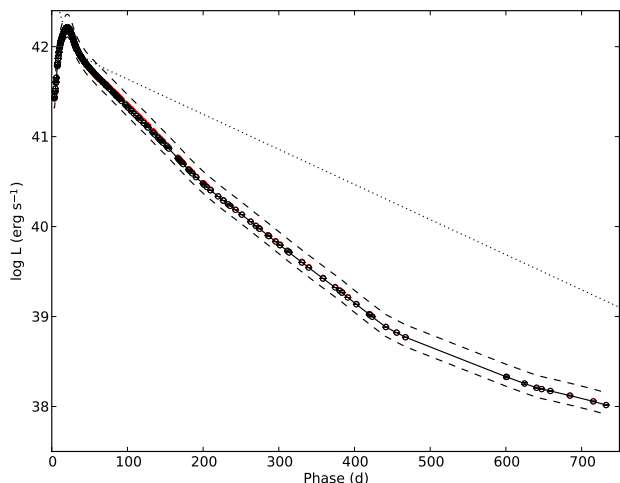

Fig. 4. UV to MIR pseudo-bolometric lightcurve for SN 2011dh calculated with the combined spectroscopic and photometric methods (black circles and solid line). The upper and lower error bars for the systematic error arising from extinction and distance (black dashed lines) and the radioactive decay chain luminosity of 0.075 $M_\odot$ of ^{56}Ni (black dotted line) are also shown.

Figure 4 shows the <750 days UV to MIR pseudo-bolometric lightcurve for SN 2011dh, as calculated with the combined spectroscopic and photometric methods, and in Table 9 we tabulate the 3-400 days period (for which we have full optical to MIR coverage) for reference. The decline rates at 100, 200, 300 and 400 days are 0.021, 0.022, 0.015 and 0.016 mag day^{-1}, respectively, but the increase in decline rate between 150 and 200 days is not as pronounced as in the optical to NIR pseudo-bolometric lightcurve. Given the caveats that the NIR coverage ends at ~400 days, and the sampling is sparse and the measurement errors large after ~500 days, the UV to MIR pseudo-bolometric lightcurve shows a significant flattening after ~500 days, when the decline rate decreases to a value similar to, but lower than, the decay rate of ^{56}Co.
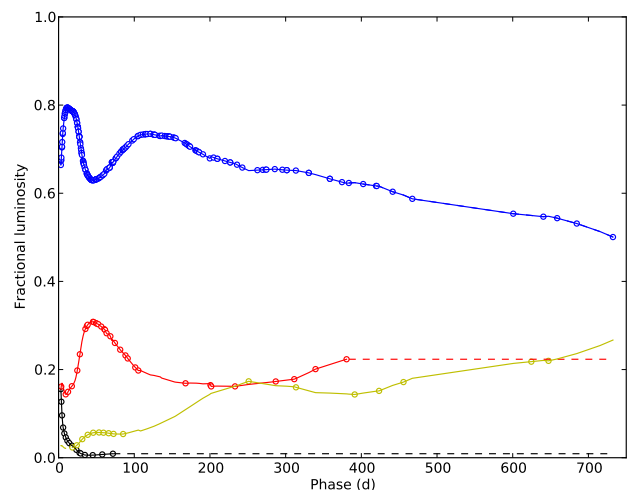

Fig. 5. Fractional UV (black dots), optical (blue dots), NIR (red dots) and MIR (yellow dots) luminosity for SN 2011dh. Interpolations and extrapolations are displayed as solid and dashed lines, respectively.

Figure 5 shows the fractional UV, optical, NIR and MIR luminosities for SN 2011dh. We assume the late-time extrapolated fractions to stay constant and do not use the adjacent colour based extrapolations applied elsewhere. The early evolution was discussed in E14a, and after 100 days the most notable is the strong increase in the MIR fraction between 100 and 250 days together with a simultaneous decrease in the optical fraction. Also notable is the increase in the NIR fraction between 200 and 350 days caused by the evolution in the *J* and *H* bands. The subsequent evolution becomes quite uncertain after ~400 days when the NIR coverage ends and ~500 days when the sampling and measurement errors become worse, but there seems to be a continuous increase in the MIR fraction, at the expense of the optical luminosity. Keeping the uncertainties in mind it is worth noting the dominance of the optical luminosity even at ~750 days.

Figure 6 shows the evolution of the SED as calculated with the photometric method, overplotted with blackbody fits to the *V*, *I*, *J*, *H* and *K* photometry as well as the observed (interpolated) spectra. The early evolution was discussed in E14a, and after 100 days the most notable is again the strong excess developing in the MIR between 100 and 250 days. There is also a similar excess developing in the *K* band between 100 and 200 days, gradually fading away towards 300 days.

3. Spectroscopy

In E14a we presented our <100 days observations and an analysis and a comparison to SNe 1993J and 2008ax. Here we present further observations spanning 100-415 days in the optical and 100-206 days in the NIR, and a continuation of the analysis and the comparison, focusing on the >100 days data. Steady-state NLTE modelling of these data, as well as a detailed analysis of the formation of the identified lines and the evolution of their fluxes, are presented in J14. Our analysis is complementary and focus mainly on the line profiles and what can be learned about the distribution of the material from the different nuclear burning zones. Following J14 we subdivide the ejecta into a Fe/Co/He core surrounded by the Si/S zone, the oxygen-rich O/Si/S, O/Ne/Mg and O/C zones and the helium and hydrogen envelopes. This onion-line structure corresponds to what is obtained in 1-D modelling (e.g. Woosley & Heger 2007), whereas in multi-D modelling hydrodynamical instabili-
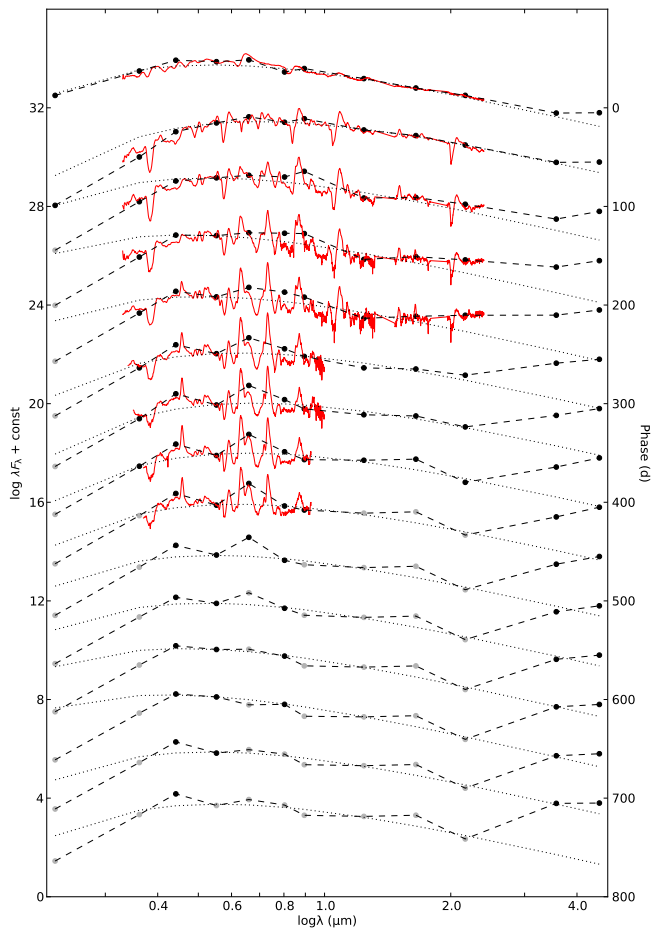
Fig. 6. The evolution of the SED as calculated with the photometric method (black dots and dashed lines) overplotted with blackbody fits to the *V*, *I*, *J*, *H* and *K* photometry (black dotted lines) as well as the observed spectra interpolated as described in Sect. **??** (red solid lines). Fluxes based on extrapolated magnitudes are displayed in shaded colour.

ties results in macroscopic mixing of these zones (e.g. Iwamoto et al. 1997). The references for the spectroscopic data of SNe 1993J and 2008ax used in the comparison are the same as specified in E14a, but in addition we also include spectra from Milisavljevic et al. (2010) for SN 2008ax and unpublished spectra for SN 1993J obtained with the WHT and the Isac Newton Telescope (INT) (P. Meikle; private communication), described in J14.

3.1. Observations

The <100 days data were obtained with the NOT, the TNG, the WHT, the CA 2.2m, the AS 1.82m and the Gran Telescopio Canarias (GTC). Details of the late time spectroscopic observations, the telescope and instrument used, epoch and instrument characteristics are given in Table 8. The late time dataset includes 21 optical spectra obtained at 16 epochs and 2 NIR spectra obtained at 2 epochs which, together with the early time observations, gives a total of 76 optical spectra obtained at 42 epochs and 20 NIR spectra obtained at 12 epochs. The reductions and calibration procedures used for the late time data are the same as in E14a and are described in detail therein.

All reduced, extracted and calibrated spectra will be made available for download from the Weizmann Interactive Supernova data REPository[2] (WISeREP) (Yaron & Gal-Yam 2012). Figure 8 shows the sequence of observed spectra where those obtained on the same night using the same telescope and instrument have been combined. For clarity some figures in this and the following sections are based on time-interpolations of the spectral sequence as described in E14a. To further visualize the evolution, the spectra have been aligned to a time axis at the right border of the panels. Interpolated spectra were used in the calculations of the bolometric lightcurve (Sect. 2.3) and S-corrections. Figure 7 shows the interpolated optical and NIR spectral evolution of SN 2011dh for 5−425 days with a 20-day sampling. All spectra in this and subsequent figures have been corrected for redshift and interstellar extinction.

3.2. Line evolution

Figure 9 shows the (interpolated) evolution for all the lines identified in J14 and below we discuss selected lines element by element. The evolution of the line fluxes were discussed in J14 and here we focus mainly on the sizes of the line emitting regions and asymmetries in the line profiles, which we will return to in Sects. 3.4 and 3.5. To measure the size of the line emitting regions we fit a simple model for optically thin line emission to the observed line profiles. The model includes an absorptive continuum opacity to mimic blue shifts casued by obscuration of receeding side emission. To measure asymmetries in the lines profiles we calculate the first wavelength moment of the flux (center of flux). The details of the methods are given in Appendix B, where we also describe how the [O I] 6300,6364 Å line is decomposed and the treatment of other blended lines.

Hydrogen Some Hα emission arising from the hydrogen-rich envelope is present in the optimal steady-state NLTE model, but is increasingly dominated by [N II] 6548,6583 Å emission arising from the helium zone after ∼150 days (J14). There is an emerging emission feature near the rest wavelength of Hα (Fig. 9) which we find to be well fitted by emission from a region with a radius of 5500 km s^{-1}, emitting mainly in the [N II] 6583 Å line, although the wings of the observed line profile may extend to ∼12000 km s^{-1} on the red side. Hα emission from the hydrogen-rich envelope is expected to result in a flat-topped line profile, at least 11000 km s^{-1} wide (E14a). The size of the line emitting region, as well as the extent of the wings, is instead consistent with emission from the helium zone, in agreement with the results in J14. Similar features exists in the spectra of SNe 1993J and 2008ax and for the latter Taubenberger et al. (2011) used a similar argument against a hydrogen envelope origin. No detectable absorption is found in any of the hydrogen lines after ∼150 days in the optimal steady-state NLTE model (J14). There is a dip in the [O I] 6300,6364 Å line profile after ∼150 days (Figs. 9 and 10), that corresponds well to the early time Hα absorption minimum at ∼11000 km s^{-1} (E14a). However, as discussed in Sect. 3.6, this feature repeats in a number of other lines and is rather due to clumping/asymmetries in the ejecta.

Helium The identified lines are the He I 5016 Å, He I 6678 Å, He I 7065 Å, He I 10830 Å and He I 20581 Å lines, although the He I 10830 Å line is blended with the [S I] 10820 Å line and
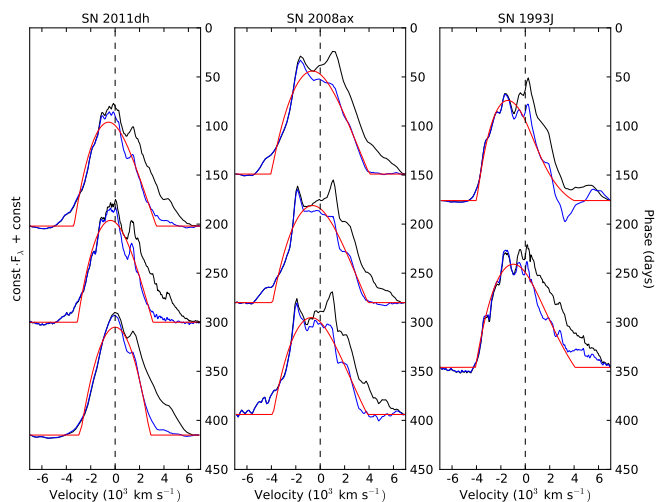
Fig. 10. [O I] 6300,6364 Å (black) and decomposed [O I] 6300 Å (blue) line profiles at selected epochs as compared to line profile fits (red) for SNe 2011dh (left panel), 2008ax (middle panel) and 1993J (right panel).

Fig. 11. Mg I] 4571 Å line profiles (black) at selected epochs as compared to line profile fits (red) for SNe 2011dh (left panel), 2008ax (middle panel) and 1993J (right panel).

the He I 6678 Å, He I 7065 Å lines quickly diminishes after 100 days (J14). Both the He I 10830 Å and He I 20581 Å lines have P-Cygni like profiles, suggesting a significant contribution from scattering, in agreement with the results in J14. The absorption extends to ~10000 km s^{-1} for the He I 20581 Å line and a bit further for the He I 10830 Å line. This is consistent with the ~11000 km s^{-1} estimated for size of the helium core in E14a. Although the unblended He I 20581 Å line has a quite broad peak it is not flat-topped, suggesting a contribution from helium at low velocities. This is consistent with the results in J14, where we find helium in the Fe/Co/He zone to contribute significantly at low velocities.

Oxygen   The identified lines are the [O I] 5577 Å, [O I] 6300,6364 Å, O I 7774 Å, O I 9263 Å, O I 11290,11300 Å and O I 13164 Å lines, although the O I 9263 Å line is blended with the [Co II] 9338,9344 Å line on the red side and the O I 13164 Å line with the [Fe II] 13210,13280 Å line on the red side (J14). The left panel of Fig. 10 shows line profile fits for the decomposed [O I] 6300 Å line for SN 2011dh. We measure the radius of the [O I] 6300,6364 Å line emitting region to 3400, 3100 and 2900 km s^{-1} at 202, 300 and 415 days, respectively. The line profile fits are quite good, but the observed emission is underestimated at low velocities and extends to at least ~5000 km s^{-1}, suggesting radially decreasing emissivity. The other oxygen lines are either too weak for a reliable measurement, optically thick or blended with other lines. The center of flux of the [O I] 6300,6364 Å line shows a blue-shift of ~1000 km s^{-1} at 100 days, decreasing towards zero at 400 days, whereas the center of flux of the [O I] 5577 Å line shows a blue-shift of ~1500 km s^{-1} at 100 days, decreasing towards ~1000 km s^{-1} at 200 days, when the line begins to fade away. We do not find any significant blue-shifts of the O I 11290,11300 Å and 13164 Å lines.

Magnesium   The identified lines are the Mg I] 4571 Å and Mg I 15040 Å lines (J14). The left panel of Fig. 11 shows line profile fits for the Mg I] 4571 Å line for SN 2011dh. We measure the radius of the Mg I] 4571 Å line emitting region to 3600, 2900
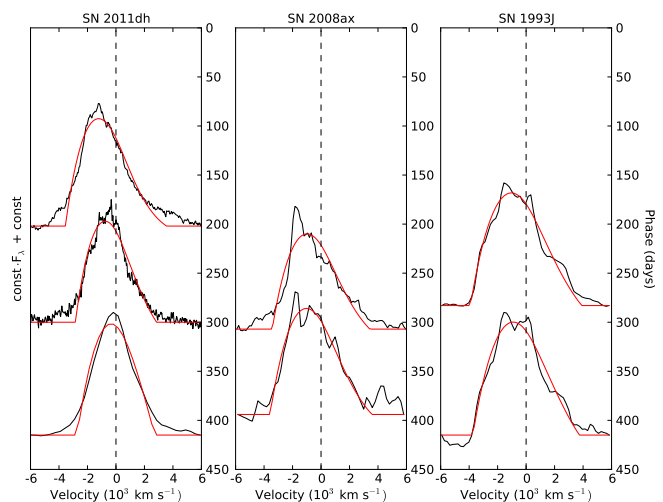
and 2700 km s^{-1} at 202, 300 and 415 days, respectively, and the radius of the Mg I 15040 Å line emitting region to 3500 and 3200 km s^{-1} at 89 and 206 days, respectively. The line profile fits of the Mg I] 4571 Å line are quite good, but the observed emission is underestimated at low velocities and extends to at least ~5000 km s^{-1}, suggesting radially decreasing emissivity. The center of flux of the Mg I] 4571 Å line shows a blue-shift of ~1000 km s^{-1} at ~200 days, decreasing towards a few hundred km s^{-1} at ~400 days. We do not find any significant blue-shift of the Mg I 15040 Å line.

Calcium   The identified lines are the Ca II 3934,3968 Å, Ca II 8498,8542,8662 Å and [Ca II] 7291,7323 Å lines, although the Ca II 8498,8542,8662 Å line is blended with the [C I] 8727 Å line (J14). The left panel of Fig. 12 shows two-component line profile fits for the [Ca II] 7291,7323 Å line for SN 2011dh. We measure the radii of the [Ca II] 7291,7323 Å line emitting regions to 2400/10000, 2100/9800 and 2400/8700 km s^{-1} at 202, 300 and 415 days respectively. The line profile fits are good in the inner region but worse in the wings, which are quite asymmetric and also blended with the [Fe II] 7155 Å line on the blue side. The center of flux for the Ca II 8498,8542,8662 Å line shows a red-shift increasing towards ~1000 km s^{-1} at 400 days. As the center of flux is calculated with respect to the rest wavelength of the Ca II 8662 Å line (Appendix. B) this suggests a significant contribution from the [C I] 8727 Å line to the flux.

Iron group   The identified lines are the [Fe II] 7155 Å, [Fe II] 12567 Å and [Fe II] 16440 Å lines, although the [Fe II] 16440 Å line is blended with the [Si I] 16450 Å line (J14). The identified cobalt lines are the [Co II] 9338,9344 Å, [Co II] 10190,10248,10283 Å and [Co II] 15475 Å lines, although the [Co II] 9338,9344 Å line is blended with the O I 9263 Å line on the blue side and the [Co II] 15475 Å line on the blue side with Fe II 15340 Å line (J14). We measure the radius of the [Fe II] 7155 Å line emitting region to 1600 and 1700 km s^{-1} at 300 and 415 days, respectively, and the radius of the [Fe II] 16440 Å line emitting region to 2300 and 2400 km s^{-1} at 89 and 206 days, re-
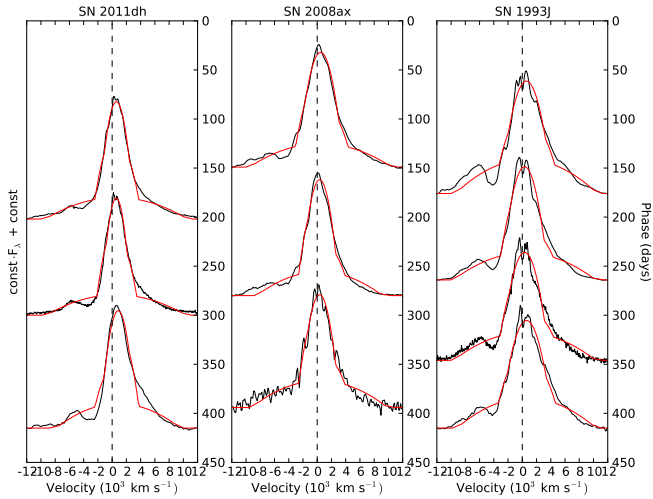
Fig. 12. [Ca ɪɪ] 7291,7323 Å line profiles (black) at selected epochs as compared to line profile fits (red) for SNe 2011dh (left panel), 2008ax (middle panel) and 1993J (right panel).
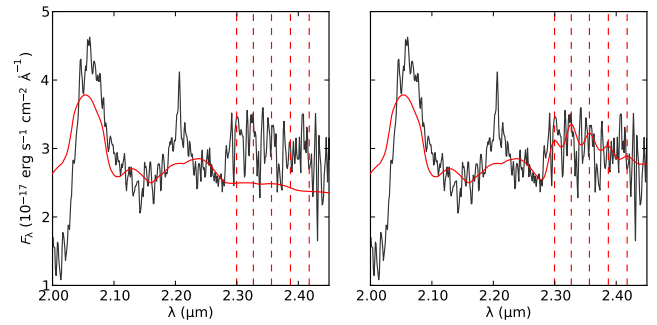

Fig. 13. Left panel: Observed (black solid line) and tweaked optimal steady-state NLTE model (red solid line) K band spectra at 206 and 200 days, respectively. Right panel: The same, but with CO LTE model emission added to the steady-state NLTE model spectra. The CO overtone band heads have been marked by red dashed lines and the steady-state NLTE model spectra flux calibrated with the observed K band flux at 206 days.

spectively. As mentioned, the latter is likely to be blended with the [Si ɪ] 16450 Å line. The [Fe ɪɪ] 12567 Å line is too weak for a reliable measurement. We measure the radius of the [Co ɪɪ] 10190,10248,10283 Å line emitting region to 1800 km s^{-1} at 89 and 206 days. The other cobalt lines are either too weak for a reliable measurement or blended with other lines.

3.3. CO emission

The left panel of Fig. 13 shows the observed K band spectrum at 206 days compared with a steady-state NLTE model spectrum at 200 days, flux calibrated with the observed K band flux at 206 days. The model (12F; see Appendix C and Sect. 4.2) includes dust but not the emission by CO. The CO first overtone ($\Delta v=2$) emits between 2.25 and 2.45 μm and we have marked the location of the band heads, which are not sharp due to the Doppler broadening of the individual transitions contributing. There is a strong excess in this region as compared to the model spectrum, the integrated flux being 9.3×10^{-14} erg s^{-1} cm^{-2}. The contribution from this flux to the K band flux is negligible though, due to the weak overlap with this band. We have used a simple LTE CO model described in Spyromilio et al. (1988) to provide a fit to the emission. The ratio of the band head emission is a diagnostic of the temperature of the CO and the shape of the band heads a diagnostic of the expansion velocity of the CO gas. In the right panel of Fig. 13 we show the combined CO model and steady-state NLTE model spectrum. The shape of the observed emission and the agreement with the simple CO model provides strong support for the identification of this feature with emission from the first overtone of CO. The temperature in the CO model is 2300 K and the emission region extends to 1500 km s^{-1}.

The region where we expect CO fundamental band emission overlaps with the S_2 band. As discussed in Sect. 2.3 there is a strong excess in this band as compared to blackbody fits to optical and NIR photometry. The total flux in the S_2 band, calculated using the zeropoint flux and the equivalent width of the band, was 1.7×10^{-13} erg s^{-1} cm^{-2} at 206 days. Note that this epoch lies in the gap of the Spitzer observations and has been linearly interpolated between 85 and 251 days. If all of the flux in the S_2 band was due to CO fundamental band emission this would correspond to a fundamental to first overtone band flux ra-

tio of 18 at 206 days. However, the SiO overtone band and dust may also contribute to the S_2 band so we cannot assume that all of the observed flux is due to CO fundamental band emission. Knowledge of the CO fundamental to first overtone band flux ratio would make an estimate of the contribution from CO fundamental band emission to the S_2 flux possible. For SN 1987A this ratio was ∼1 at 100 days, a few at 200 days, but increased dramatically to ∼100 towards 500 days (Bouchet & Danziger 1993). Assuming these flux ratios the contribution to the S_2 flux from CO fundamental band emission would be minor at 206 days.

3.4. Line emitting regions

The sizes of the line emitting regions are related to the distribution of the material from the different nuclear burning zones, determined by hydrodynamical instabilities in the explosion. In J14 we found the Mg ɪ lines to arise from the O/Ne/Mg zone, the O ɪ lines to arise from the O/Ne/Mg zone and, depending on the amount of molecule (CO and SiO) cooling, the O/C and O/Si/S zones. We also found the [Ca ɪɪ] 7291,7323 Å line to arise mainly from the Si/S zone and the Fe ɪɪ and Co ɪɪ lines to arise from the Fe/Co/He zone. In Sect. 3.2 we used our line profile model to estimate the sizes of the O ɪ, Mg ɪ, [Ca ɪɪ] 7291,7323 Å, Fe ɪɪ and Co ɪɪ line emitting regions for SN 2011dh. The estimated radii of the Mg ɪ and O ɪ line emitting regions of 2900-3400 and 2800-3800 km s^{-1}, respectively, were similar whereas the estimated radii of the [Ca ɪɪ] 7291,7323 Å and the Fe ɪɪ and Co ɪɪ line emitting regions of 2100-2400 and 1600-2400 km s^{-1}, respectively, were progressively smaller. This progression is consistent with the (unmixed) onion-like structure of the nuclear burning zones and suggests incomplete mixing of the oxygen, Si/S and Fe/Co/He material. This is in agreement with results from multi-D hydrodynamical modelling, e.g. the 2-D hydrodynamical modelling of SN 1993J by Iwamoto et al. (1997), which shows significant differences in the distribution of the oxygen and Fe/Co/He material.

The left panel of Fig. 14 shows mirrored blue-side line profiles for the [O ɪ] 6300 Å, Mg ɪ 4571 Å, [Ca ɪɪ] 7291 Å and [Fe ɪ] 7155 Å lines for SN 2011dh at 300 days. The blue side is less affected by obscuration as compared to the red side and contamination from the [O ɪ] 6364 Å and [Ca ɪɪ] 7323 Å lines to the [O ɪ] 6300 Å and [Ca ɪɪ] 7291 Å lines is probably modest. This figure nicely illustrates the different sizes of the line emitting regions
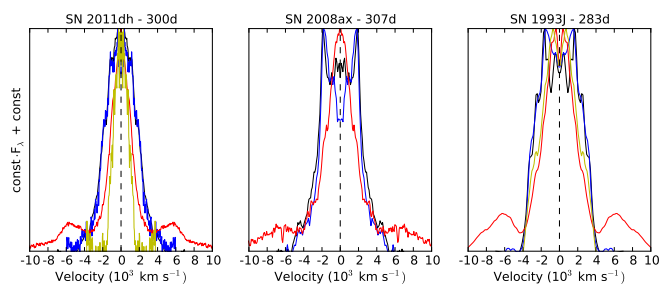
Fig. 14. Continuum subtracted mirrored blue-side profiles for the [O I] 6300,6364 Å (black), Mg I] 4571 Å (blue), [Ca II] 7291,7323 Å (red) and [Fe I] 7155 Å (yellow) lines for SNe 2011dh, 2008ax and 1993J at 300, 307 and 283 days respectively.

discussed above and also shows a remarkable similarity of the blue-side [O I] 6300 Å and Mg I] 4571 Å line profiles. This similarity persists also in small scale fluctuations (Sect. 3.6) and suggests these lines to arise mainly from the O/Ne/Mg zone and the contributions from the O/C and O/Si/S zones to the [O I] 6300 Å flux to be modest.

The middle and right panels of Figs. 10, 11, 12 and 14 show line profile fits and mirrored blue-side line profiles for SNe 2008ax and 1993J, respectively. For SN 1993J the estimated radii of the line emitting regions are 4000-4100 km s^{-1} for the [O I] 6300 Å line, 3700-3900 km s^{-1} for the Mg I] 4571 Å line and 3000-3400 km s^{-1} for the [Ca II] 7291,7323 Å line. For SN 2008ax the estimated radii of the line emitting regions are 3900-4000 km s^{-1} for the [O I] 6300 Å line, 3400-3600 km s^{-1} for the Mg I] 4571 Å line and 2600-3000 km s^{-1} for the [Ca II] 7291,7323 Å line. These radii are larger than those estimated for SN 2011dh and larger for SN 1993J than for SN 2008ax. The radii of the Mg I] 4571 Å and the [O I] 6300 Å line emitting regions are similar and the radius of the [Ca II] 7291,7323 Å line emitting region is smaller suggesting incomplete mixing of the oxygen and Si/S material. This is supported by Fig. 14 and the similarity of the blue-side Mg I] 4571 Å and the [O I] 6300 Å line profiles is striking, suggesting these to arise mainly from the O/Ne/Mg zone.

It is also evident from Fig. 14 that there are considerable differences in the shapes of line profiles between SNe 2011dh, 2008ax and 1993J. The profile of the [Ca II] 7291,7323 Å line is centrally peaked for all three SNe whereas the peaks of the [O I 6300] Å and Mg I] 4571 Å line are considerably flatter for SNe 1993J and 2008ax. A thourough discussion of this issue is outside the scope of the paper however, and has to be postponed to future works. It is worth noting though, that the double peaks of the [O I] 6300,6364 Å line profile for SN 2008ax (Fig. 10) seem to be well explained by a repetition of the blue peak, as suggested by Milisavljevic et al. (2010) and Taubenberger et al. (2011), and that this blue peak seems to repeat in the Mg I] 4571 Å line (Fig. 11), as pointed out by Milisavljevic et al. (2010). Maurer et al. (2010) suggested absorption by Hα to explain the double peaks which, given this and the negligible Hα absorbtion at late times found in J14, seems less likely. Our decomposition method assumes a [O I] 6300,6364 Å line ratio of 3 and is described in Appendix B.

3.5. Line asymmetries

Figure 15 shows the center of flux velocities for the [O I] 6300,6364 Å, [O I] 5577 Å, Mg I] 4571 Å and [Ca II] 7291,7323 Å lines for SNe 2011dh, 2008ax and 1993J. As discussed in Sect. 3.2 there is a blue-shift of the [O I] 6300,6364 Å, [O I] 5577 Å and Mg I] 4571 Å lines for SN 2011dh which, as seen in Fig. 15, is also present, and even more pronounced for SNe 2008ax and 1993J. For SN 2011dh this blue-shift disappears towards 400 days but for SNe 2008ax and 1993J the blue-shift saturates at ~500 km s^{-1} after 200 days. In J14 we provide a thorough discussion of these blue-shifts and suggest the cause to be line-blocking in the core based on results from the steady-state NLTE modelling. There is no significant blue shift in the O I 11300 Å, O I 13164 Å and [Mg I] 15040 Å lines for SNe 2011dh (Sect. 3.2) and 2008ax in support of this hypothesis, as line-blocking is less effective in the NIR (J14). Milisavljevic et al. (2010) find the [O I] 6300,6364 Å, [O I] 5577 Å and Mg I] 4571 Å lines to be either symmetric or asymmetric towards the blue for a sample of 18 stripped envelope SNe whereas Taubenberger et al. (2009) find a systematic blue-shift of the [O I] 6300,6364 Å line disappearing with time for another, partly overlapping, sample of 39 stripped envelope SNe. Both these results favours obscuration of the receding-side emission and disfavours ejecta asymmetries as the explanation. However, to explain the saturation of the blue-shifts for SNe 2008ax and 1993J the evolution of the core-opacity needs to be different for these SNe as compared to SN 2011dh.

As a further complication blue-shifts of the lines profiles can also be produced by dust in the ejecta. Using our line profile model and assuming a size of the line-emitting region of 3000 km s^{-1}, roughly corresponding to size of the oxygen zone for SN 2011dh, we find a blue-shift of the center of flux of 150-250 km s^{-1} for an optical depth of 0.25-0.44. This range of optical depths are found to reproduce the increase in the decline rates of the optical pseudo-bolometric lightcurve observed between 100 and 200 days (Appendix C.6). However, the change in optical depth due to dust and line blocking is hard to disentangle, most lines are either blends, do not arise solely from the core or are too weak and if the dust is located differently the effect on the line profiles would be different. At 415 days, when the effect from line-blocking would be the least, the center of flux for the [O I] 6300,6364 Å and Mg I] 4571 Å lines, which arises solely from the core, shows a blue-shift of ~50 and ~200 km s^{-1}, respectively. The small blue-shift of the former indicates that if dust is formed in the ejecta it is not homogeneously distributed within the core. However, the difference as compared to the expected value is only 100-200 km s^{-1} so this constraint is rather weak. For SNe 1993J and 2008ax dust in the ejecta provides an alternative explanation for the saturation of the blue-shifts. Using our line profile model and assuming a size of the line-emitting region of 4000 km s^{-1}, roughly corresponding to size of the oxygen zone for SNe 1993J and 2008ax, we find a blue shift of the center of flux of ~500 km s^{-1} to correspond to an optical depth of ~1. Neither SN 1993J nor SN 2008ax show a period with increased decline rates in the optical pseudo-bolometric lightcurve which disfavours dust as the explanation, although SN 1993J show a MIR excess developing between 100 and 250 days, similar to that observed for SN 2011dh.
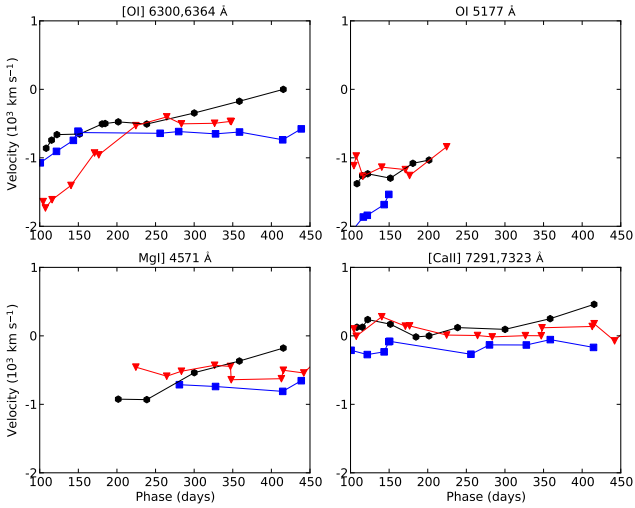
Fig. 15. Center of flux velocities for the [O I] 6300,6364 Å (upper left panel), [O I] 5577 Å (upper right panel) Mg I] 4571 Å (lower left panel), [Ca II] 7291,7323 Å (lower right panel) lines for SNe 2011dh (black dots), 2008ax (blue squares) and 1993J (red triangles).

3.6. Small scale fluctuations

Small scale fluctuations in the line profiles may provide evidence for a clumpy ejecta as previously demonstrated for SNe 1987A (Stathakis et al. 1991; Chugai 1994) and 1993J (Matheson et al. 2000). In a simplified way we may represent the material of some nuclear burning zone by a number of randomly distributed clumps, having a typical size and occupying some fraction of the ejecta volume (filling factor). The small scale fluctuations in the line profiles then arise from statistical fluctuations in the distribution of the clumps, the RMS (Root Mean Square) of the fluctuations increasing with decreasing number of clumps and/or filling factor and/or increasing size of the clumps. In the simplest case the ejecta is assumed to be a (globally) homogeneous sphere, which is in fact exactly how the core is represented in the steady-state NLTE modelling (Sect. 4.2).

Figure 16 shows small scale fluctuations in the [O I] 6300,6364 Å, [O I] 5577 Å, O I 7774 Å, Mg I] 4571 Å and Na I 5890,5896 Å lines at 202 and 300 days. The resolution is ~600 and ~250 km s^{-1} in the 202 and 300 days spectra respectively. A 1000 km s^{-1} box average of the line profile was repeatedly (3 times) subtracted to enhance the small scale fluctuations. The method has been tested on the product of synthetic large and small scale structures and the small scale structures are recovered with reasonable accuracy. In the upper left panel we show a comparison of the [O I] 6300 Å line profiles at 202 and 300 days. These are very similar and there is not much evolution of the small scale fluctuations in the line profile during this period. We identify 8 features marked A-H with an FWHM between 300 and 600 km s^{-1} present at both epochs. However, features G and H interpreted as belonging to the [O I] 6364 Å line match very well with the E and F features interpreted as belonging to the [O I] 6300 Å line so these are likely to be repetitions. Minimizing the RMS of the small scale fluctuations redwards 3000 km s^{-1} (G and H), where the [O I] 6364 Å flux was subtracted from the [O I] 6300,6364 Å line profile using the method described in Appendix. B, we find a line ratio of 2.9 at 202 and 300 days to give a complete removal of features G and H. This ratio is in agreement with the value of 3 expected for optically thin emission and also with the results from J14.
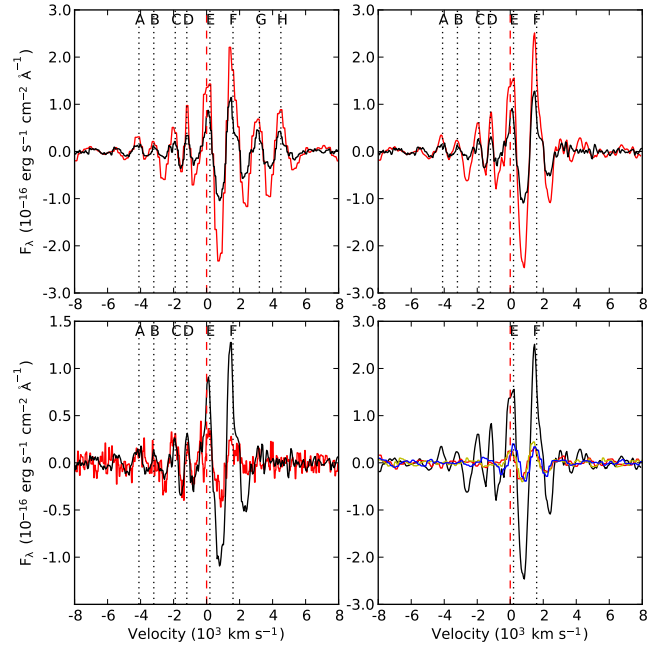
Fig. 16. Comparison of box average subtracted line profiles. The upper left panel shows the [O I] 6300 Å line profile at 202 (red) and 300 (black) days. The upper right panel shows the corrected [O I] 6300 Å line profile at 202 (red) and 300 (black) days. The lower left panel shows the corrected [O I] 6300 Å line profile (black) and the Mg I] 4571 Å line profile (red) at 300 days. The lower right panel shows the corrected [O I] 6300 Å line profile (black) and the [O I] 5577 Å (red), O I 7774 Å (green) and Na I 5890/5896 Å (blue) line profiles at 202 days.

In the upper right panel we show the corrected [O I] 6300 Å line profiles at 202 and 300 days and in the lower left panel we show a comparison to the Mg I] 4571 Å line profile at 300 days. All features except B are clearly identified and the agreement is good. The features on the red side are weaker for the Mg I] 4571 Å line, which is consistent with the larger red-side flux deficit for this line, but the relative (flux normalized) strength of all features are similar. The good agreement suggests that the [O I] 6300 Å and Mg I] 4571 Å lines arise from the same nuclear burning zones. Given the findings in J14 this, in turn, suggests that the Mg I] 4571 Å and [O I] 6300 Å lines arises mainly from the O/Ne/Mg zone and that the contributions from the O/Si/S and O/C zones to the [O I] 6300 Å flux are modest.

In the lower right panel we show a comparison of the corrected [O I] 6300 Å line profile and the [O I] 5577 Å, O I 7774 Å and Na I 5890,5896 Å line profiles at 202 days. The E and F features are clearly identified in all of these line profiles, but none of the other features are seen. Since the E and F features are also the strongest it is not clear if the absence of the other features is real or if the other features are just too faint to be seen. The relative strength of the E and F features are similar for the [O I] 5577 Å, O I 7774 Å and [O I] 6300 Å lines, suggesting that all these lines arise mainly from the same nuclear burning zones, whereas the relative strength of these features for the Na I 5890,5896 Å line is a bit (~50 percent) weaker, suggesting contributions from other nuclear burning zones. This is consistent with the results in J14, where all oxygen lines are found to arise from the oxygen zones and the Na I 5890,5896 Å line partly from the O/Ne/Mg zone.

The small scale fluctuations in the [Ca II] 7291,7323 Å line (not shown) do not match very well with those in the [O I] 6300 Å line and the relative strength of the features seen is weaker. We were not able to correct for blending using repetitions of the features, which makes the interpretation less clear, and removal of the [Ca II] 7323 Å flux assuming a line ratio of 1.5, as expected for optically thin emission, does not improve the agreement with the [O I] 6300 Å line. The result is consistent with the findings in J14, were we found this line to arise mainly from other nuclear burning zones (Si/S). This is also suggested by the different sizes of the line emitting regions discussed in Sect. 3.4.

Shivvers et al. (2013) presented an analysis of the line profiles of the [O I] 6300,6364 Å, O I 7774 Å and Mg I 4571 Å lines at 268 days. By decomposition of the [O I] 6300,6364 Å line profile into Gaussian profiles, assuming an [O I] 6300,6364 Å line ratio of 3, they found a good fit for one broad and two narrow profiles located at -400 and 1600 km s^{-1}. The two strongest features in our analysis, E and F, are located at ~0 and ~1500 km s^{-1} and likely correspond to the two features found by Shivvers et al. (2013). They also find these features to repeat in the O I 7774 Å and Mg I 4571 Å lines, in agreement with our analysis. The difference in velocity for the E feature is likely explained by the different methods used.

Matheson et al. (2000) presented an analysis of the small scale fluctuations in the line profiles of SN 1993J. They found a good agreement between the fluctuations in the [O I] 6300 Å, [O I] 5577 Å and O I 7774 Å line profiles, which is in agreement with our results for SN 2011dh. However, they did not find a good agreement between the fluctuations in the [O I] 6300 Å and Mg I] 4571 Å line profiles, which is a bit surprising since we find an excellent agreement for SN 2011dh. One possible explanation is that the [O I] 6300 Å line is dominated by flux from the O/Ne/Mg zone for SN 2011dh but not for SN 1993J (see above). Filippenko & Sargent (1989) presented an analysis of the small scale fluctuations in the line profiles of the Type Ib SN 1985F. Similar to our analysis they found repetitions of the identified features in the [O I] 6300 and 6364 Å lines and a line ratio close to 3 using the strongest feature.

Matheson et al. (2000) applied the statistical model by Chugai (1994) to their spectra of SN 1993J, giving a filling factor of ~0.06 for oxygen zone material, distributed within a sphere with 3800 km s^{-1} radius. Using their estimated typical clump size of 300 km s^{-1}, this corresponds to ~900 clumps. The model requires the radius of the sphere containing the clumps, the typical size of the clumps and the RMS of relative flux fluctuations in lines originating from the clumps. In the case of SN 2011dh we adopt a radius of the sphere containing the bulk of the oxygen zone material of ~3500 km s^{-1} based on the estimates of the O I and Mg I line emitting regions in Sect. 3.2. For SN 1987A a typical clump size of 120 km s^{-1} was estimated from the power spectrum of the [O I] 6300 Å line by Stathakis et al. (1991) using high-resolution spectroscopy, but it is not clear how this was done by Matheson et al. (2000). As we do not have access to high-resolution spectroscopy for SN 2011dh we can only estimate an upper limit on the typical clump size taken to be 300 km s^{-1}, the smallest size of the features seen. The RMS of the relative flux fluctuations in the inner part (±2000 km s^{-1}, see Chugai (1994)) of the sphere for both the corrected [O I] 6300 Å and the Mg I 4571 Å lines was ~0.09 at 300 days. Using these estimates and applying Chugai (1994, eq. 11), we find an upper limit on the filling factor of oxygen zone material within the sphere of ~0.07 and a lower limit on the number of oxygen zone clumps

of ~900. These values are in good agreement with the values estimated by Matheson et al. (2000) for the clumping of oxygen zone material in SN 1993J.

4. Lightcurve modelling

In this section we discuss modelling of the bolometric and photometric lightcurves with HYDE, a hydrodynamical code described in Ergon et al. (2014b, herafter E14b) and the steady-state NLTE code described in Jerkstrand et al. (2011, 2012) and J14. In J14 we present spectra for a set of steady-state NLTE models and here we present pseudo-bolometric and photometric lightcurves for the same models obtained through synthetic photometry. HYDE is aimed for bolometric lightcurve modelling and has the hydrodynamical and time-dependent capabilities needed to evolve the SN through the explosion and the diffusion phase, whereas the NLTE code can only be used at >100 days, when steady-state is satisfied. In this phase both codes have the capability to produce bolometric lightcurves and use the same radiative transfer model to calculate the deposition of the radioactive decay energy. So, as far as the lightcurves are concerned, the advantage of the steady-state NLTE code is the capability to produce pseudo-bolometric and photometric lightcurves or, equivalently, the corresponding bolometric corrections.

Given the extensive photometric coverage for SN 2011dh, both in time and wavelength, consistent modelling of the lightcurves is highly desirable. Ideally, HYDE would be used to evolve a grid of initial stellar models through a parametrized explosion and the photospheric phase, and the resulting ejecta models then fed into the steady-state NLTE code and subsequently evolved. For the <100 days evolution we use the grid of SN models, constructed with HYDE and MESA STAR (Paxton et al. 2011, 2013), presented in E14b, but to evolve this 15×10×9×9 grid further with the steady-state NLTE code is not computationally feasible. To partly circumvent this problem we try two different approaches. First, to extend the temporal coverage of the J14 steady-state NLTE models to early times, we evolve these through the <100 days period using HYDE in homologous mode. Secondly, to extend the temporal coverage of the hydrodynamical model grid to 400 days, we apply a bolometric correction determined with the steady-state NLTE code. Finally, after 500 days time-dependent effects becomes important (Sect. 4.4) and a steady-state assumption is no longer valid, so in this phase neither code apply.

4.1. Hydrodynamical modelling of the <100 days bolometric lightcurve

B12 presented a hydrodynamical model for SN 2011dh that well reproduced the observed <100 days bolometric lightcurve and photospheric velocity evolution. Here we use the grid of SN models constructed with HYDE and MESA STAR (Paxton et al. 2011, 2013), presented in E14b, and the procedure described therein to fit the <100 days UV to MIR pseudo-bolometric lightcurves and photospheric velocities of SNe 2011dh, 1993J and 2008ax. The UV to MIR bolometric correction is assumed to be negligible and is likely >-0.15 mag at <100 days (Appendix C). A detailed desciption of HYDE is provided in E14b and a summary in Appendix D. The strength of the method as compared to previous hydrodynamical modelling is the ability to determine the errors in the model parameters arising from the observed quantities and the degeneracy of the solutions, issues previously discussed in E14a from approximate considerations. The progenitor and SN parameters are the helium core

mass (M_{He}), the explosion energy (E), the mass of ejected ^{56}Ni (M_{Ni}) and the distribution of it (Mix_{Ni}). The stellar models consists of bare helium cores without a hydrogen envelope, which is sufficient to determine the explosion energy, helium core mass and mass and distribution of the ejected ^{56}Ni (E14b). The validity of the bare helium core approximation is discussed in E14b, depends on the mass of the hydrogen envelope and is most critical for the derived explosion energy. As described in E14b equal weights are given to the diffusion phase lightcurve, the early tail lightcurve and the early photospheric velocity evolution. To estimate the radius, as done in B12, modelling of the early cooling phase, which depends on the hydrogen envelope, would be necessary. The UV to MIR pseudo-bolometric lightcurves for SNe 1993J and 2008ax were constructed by assuming the same UV and MIR fractions as for SN 2011dh.

The upper and middle panels of Fig. 17 show the optimal model bolometric lightcurve and photospheric velocity evolution compared to the observed UV to MIR pseudo-bolometric lightcurve and velocity evolution for the absorption minimum of the Fe II 5169 Å line for SNe 2011dh, 2008ax and 1993J. Table 3 gives the helium core mass, explosion energy, mass of ejected ^{56}Ni and the distribution of it for the optimal models and the corresponding errors, calculated as described in E14b. A systematic error of 15 percent in the photospheric velocities has been assumed, which is similar to the average difference between the absorption minimum of the Fe II 5169 Å line and the thermalization radius as estimated from blackbody fits for SN 2011dh (E14a). This error mainly propagates to the helium core mass and explosion energy whereas the errors in the distance and extinction mainly propagate to the mass of ejected ^{56}Ni (E14b). The derived parameters for SN 2011dh are in good agreement with the results in B12. The helium core mass and explosion energy derived for SNe 1993J and 2008ax are similar to what is derived for SN 2011dh, whereas the mass of ejected ^{56}Ni differs significantly. The mixing of the ^{56}Ni is strong for all three SNe and for SN 2011dh the fraction of ^{56}Ni outside 3500 and 6000 km s^{-1} is 53 and 8 percent respectively. This is in rough agreement with the optimal steady-state NLTE model, although in this model the ^{56}Ni is confined within 6000 km s^{-1}. The derived explosion energy for SN 1993J is significantly lower as compared to previous hydrodynamical modelling (e.g. Shigeyama et al. 1994). This is likely a consequence of the bare helium core approximation, as the more massive hydrogen envelope for this SN takes up a significant fraction of the explosion energy (E14b). We note that the velocity evolution of SN 2008ax is not well fitted, which could be explained by a worse correspondence between the absorption minimum of Fe II 5169 Å and the photosphere as compared to SNe 2011dh and 1993J.

The lower panels of Fig. 17 show contour plots of the standard deviation in the fit, normalized to that of the optimal model, as a function of helium core mass and explosion energy. We also show the constraints M_{ej}^2/E=const and M_{ej}/E=const provided by the lightcurve and the photospheric velocity evolution, respectively (E14b). The less good fit of the photospheric velocity evolution for SN 2008ax is reflected in an extended degeneracy region, mainly along the M_{ej}^2/E=const curve. If we assume a good fit to correspond to a normalized standard deviation of <2 and also take into account the errors arising from the observed quantities (Table 3) we find an upper limit on the helium core mass for all three SNe of $\lesssim 4$ M$_\odot$, corresponding to an upper limit on the initial mass of $\lesssim 15$ M$_\odot$.
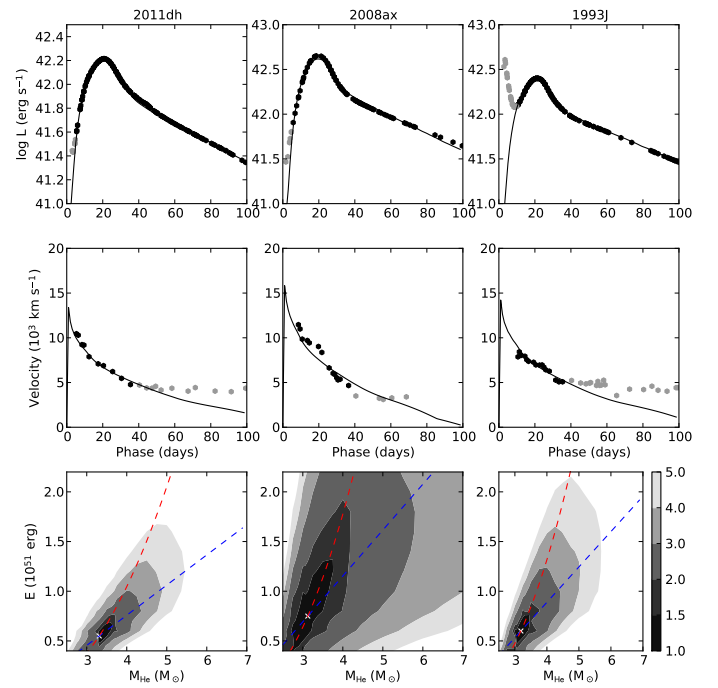
Fig. 17. Upper and middle panels: Bolometric lightcurve (upper panels) and photospheric velocity evolution (middle panels) for the optimal models as compared to the observed UV to MIR pseudo-bolometric lightcurve and velocity evolution for the absorption minimum of the Fe II 5169 Å line for SNe 2011dh (left panels), 2008ax (middle panels) and 1993J (right panels). Observations not included in the fit are displayed in gray. Lower panels: Contour plots showing the standard deviation in the fits, normalized to that of the optimal model, projected onto the E-M_{He} plane for SNe 2011dh (left panels), 2008ax (middle panels) and 1993J (right panels). We also show the constraints M_{ej}/E=const (blue) and M_{ej}^2/E=const (red) provided by the photospheric velocity evolution and the bolometric lightcurve, respectively.

4.2. NLTE modelling of the 100-500 days pseudo-bolometric and photometric lightcurves.

Here we compare the pseudo-bolometric and photometric lightcurves for the J14 steady-state NLTE models to the observed 100-500 days pseudo-bolometric and photometric lightcurves. These models span a restricted volume of parameter space and the degeneracy of the solution and the errors in the model parameters can not be quantified. The optimal model, presented in J14, has been chosen to give the best agreement with both nebular spectra and the bolometric and photometric lightcurves. In J14 we discuss the constraints on the model parameters provided by the nebular spectra and here we discuss the constraints provided by the pseudo-bolometric and photometric lightcurves. The set of models, listed in table 3 in J14, varies in the following parameters: initial mass (12, 13 or 17 M$_\odot$), degree of macroscopic mixing (medium or strong), density contrast (low or high), positron trapping (local or non-local), molecule cooling (complete or none) and dust (τ_{dust}=0, 0.25 and 0.44). In this work we restrict ourselfs to the model families differing in a single parameter listed in table 4 in J14 and two additional models 12E and 12F described in Appendix C.6, differing from the optimal model (12C) only in the absence (12E) and the properties (12F) of the dust. The effects of the model parameters on the model lightcurves are discussed in in Appendix C.

Table 3. Explosion energy, helium core mass, mass of the ejected ^{56}Ni and the distribution of it for the optimal models of SNe 2011dh, 1993J and 2008ax.

SN	E (10^{51} erg)	M_{He} (M$_\odot$)	M_{Ni} (M$_\odot$)	Mix$_{Ni}$
2011dh	0.55 (+0.40,-0.15)	3.44 (+0.70,-0.26)	0.075 (+0.028,-0.020)	1.10 (+0.06,-0.00)
2008ax	0.70 (+0.50,-0.30)	3.19 (+0.56,-0.39)	0.175 (+0.087,-0.099)	0.93 (+0.04,-0.00)
1993J	0.60 (+0.45,-0.20)	3.31 (+0.60,-0.25)	0.106 (+0.034,-0.028)	0.90 (+0.24,-0.08)

4.2.1. Model parameters

The initial mass is the primary parameter describing the J14 models. The 12, 13 and 17 M$_\odot$ models are constructed using results from 1-D stellar evolutionary and hydrodynamical modelling. The nucleosynthesis is taken from Woosley & Heger (2007) and the ejecta divided into a core, a helium envelope (density profile from B12; private communication) and a hydrogen envelope ($\rho \propto v^{-6}$). The interfaces between these are fixed in velocity space at 3500 and 11000 km s^{-1} based on observations and modelling (E14a, this paper). The mass of ejected ^{56}Ni (and thus the mass of the Fe/Co/He zone) is not varied in the models and is fixed to 0.075 M$_\odot$ based on hydrodynamical modelling (B12, this paper). The macroscopic mixing and density contrast parameters mimics effects on the ejecta structure arising in 3-D hydrodynamical modelling. Macroscopic mixing of the nuclear burning zones occurs in the explosion due to hydrodynamical instabilities, and is represented in a statistical sense as a fully mixed core of constant average density. Incomplete mixing of the core, as we found evidence for in Sect. 3.4, have not been investigated. The strong mixing models differs from the medium mixed models only in that 50 percent of the Fe/Co/He material is mixed into the helium envelope. Expansion of the Fe/He/Co clumps occurs at early times due to radioactive heating, and is represented as a density contrast between the Fe/Co/He clumps and the surrounding material. The positron trapping parameter mimics the effect of a strong magnetic field on the positron opacity, assumed to be high enough in the presence of a magnetic field for the positrons to be locally absorbed. The modelling does not include a self-consistent treatment of the formation of molecules and dust in the ejecta, but the effect of these are included in a simplified way as described in Appendices C.5 and C.6. The effect of molecules is represented as the fraction of the cooling in the O/C and O/Si/S zones going into molecule (CO and SiO) emission. Dust absorption is represented as a gray absorptive opacity in the core and the emission as blackbody emission, the temperature determined as described in Appendix C.6.

4.2.2. The optimal model.

The optimal model (12C) has an initial mass of 12 M$_\odot$, strong macroscopic mixing, local positron trapping, no molecule cooling, dust with τ_{dust}=0.25 and a high density contrast. We have also constructed a tweaked optimal model (12F), which differs from the optimal model only in the optical depth and temperature of the dust (Appendix C.6). Figures 18 and 19 show the 100-500 days optimal model, tweaked optimal model and observed pseudo-bolometric lightcurves. The pseudo-bolometric lightcurves for both models show a good agreement with observations until ~300 days, where our NIR coverage ends, the dif-
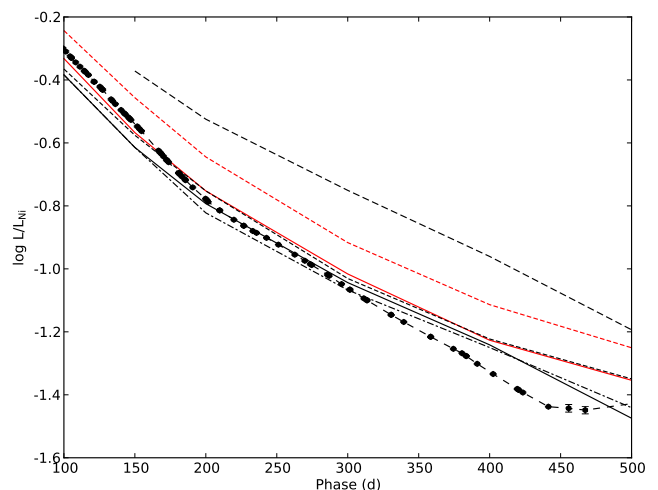

Fig. 18. 100-500 days observed (black circles) and J14 model optical to MIR pseudo-bolometric lightcurves normalized to the radioactive decay chain luminosity of 0.075 M$_\odot$ of ^{56}Ni. Selected representatives (12A,12C,13A,13C,17A) of the model families differing in initial mass and macroscopic mixing are shown and displayed as follows: 12 M$_\odot$ (solid lines), 13 M$_\odot$ (short dashed lines), 17 M$_\odot$ (long dashed lines), medium mixing (red), strong mixing (black). The tweaked optimal model (12F; black dashed-dotted line), which only differs from the optimal model (12C) in the properties of the dust, is also shown.

ferences being ≲0.2 mag. During the 300-500 days period there is a continued good agreement in the optical pseudo-bolometric lightcurve whereas the difference in the optical to MIR pseudo-bolometric lightcurve slowly increases to ~0.3 mag. Given the uncertainty in the extrapolations of the NIR photometry this is not too worrying. Figure 20 shows the J14 model and observed photometric lightcurves. The photometric lightcurves for the optimal models show an overall good agreement with observations, the differences being mostly ≲0.3 mag, but there are some notable exceptions as the U and MIR bands. The U band is particularly sensitive to the extinction so the underproduction of this band could be an indication that the adopted value needs to be revised. The discrepancy decreases with time though so the interpretation is not clear. The discrepancies in the MIR bands are much improved in the tweaked optimal model and are discussed further in Sect. 4.2.4.

4.2.3. Calculation of the <100 days bolometric lightcurves with HYDE

Only after ~100 days steady-state is satisfied and the NLTE code can be used. Therefore we use HYDE in homologous mode to
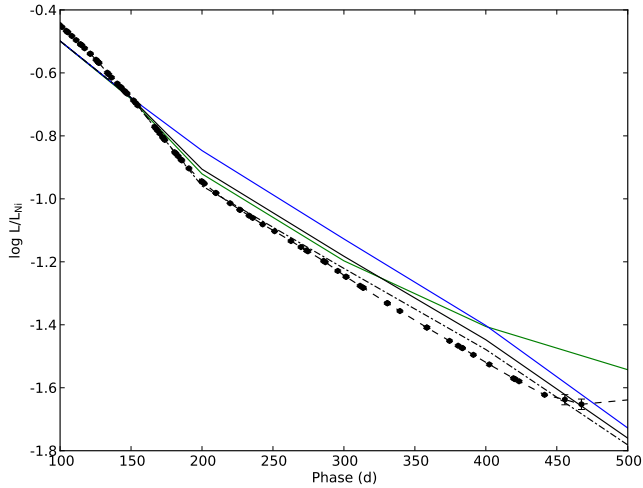
Fig. 19. 100-500 days observed (black circles) and J14 model optical pseudo-bolometric lightcurves normalized to the radioactive decay chain luminosity of 0.075 $M_\odot$ of ^{56}Ni. The optimal model (12C; black solid line), the tweaked optimal model (12F; black dashed-dotted line) and model 12E (blue solid line), which only differ in the amount of dust, are shown together with model 12B (green solid line) which differs from the optimal model only in the positron trapping.

Fig. 21. <100 days observed (black circles) and J14 model bolometric lightcurves as calculated with HYDE. The model families differing in initial mass and macroscopic mixing are shown and displayed as follows: 12 $M_\odot$ (solid lines), 13 $M_\odot$ (short dashed lines), 17 $M_\odot$ (long dashed lines), medium mixing (red), strong mixing (black).

produce 3-100 days bolometric lightcurves for the J14 models. The J14 models are first (homologously) rescaled to day one and then evolved with HYDE through the 1-100 days evolution. The initial temperature profile at 1 days is adopted from the optimal hydrodynamical model for SN 2011dh (Sect. 4.1), with the mixing of the ^{56}Ni adjusted to match that of the J14 models. The subsequent evolution is not sensitive to the choice of initial temperature profile, as it is powered by the continous injection of radioactive decay energy. Figure 21 shows the 3-100 days bolometric lightcurves for the J14 model families differing in initial mass and macroscopic mixing compared to the observed optical to MIR pseudo-bolometric lightcurve. The other steady-state NLTE model parameters have no or negligible influence on the bolometric lightcurve (Appendix C). The optical to MIR BC for the J14 models is likely >-0.15 mag during this period (Appendix C) so the comparison is justified. The bolometric lightcurve for the optimal model shows an overall agreement, although the peak is overproduced by ~0.2 mag.

4.2.4. Constraints on the model parameters

The effects of the model parameters on the lightcurves are discussed in Appendix C and here we summarize the results and discuss the constraints obtained from those on our choice of model parameters. As explained in Appendix C, a split of the lightcurve into a bolometric lightcurve and a bolometric correction (BC) is useful for the analysis. The bolometric lightcurve depends only on the energy deposition whereas the BCs depend on how this energy is processed. The energy deposition is independent of molecule cooling and dust and, within the parameter space covered by the J14 models, only weakly dependent on the density contrast and the positron trapping (Appendix C). Therefore the bolometric lightcurve depends significantly only on the initial mass and macroscopic mixing whereas the BCs may depend on all model parameters.

Observationally, the split into bolometric lightcurves and BCs is not straightforward as we do not know the former and can not calculate the latter. However, the spread in the optical to
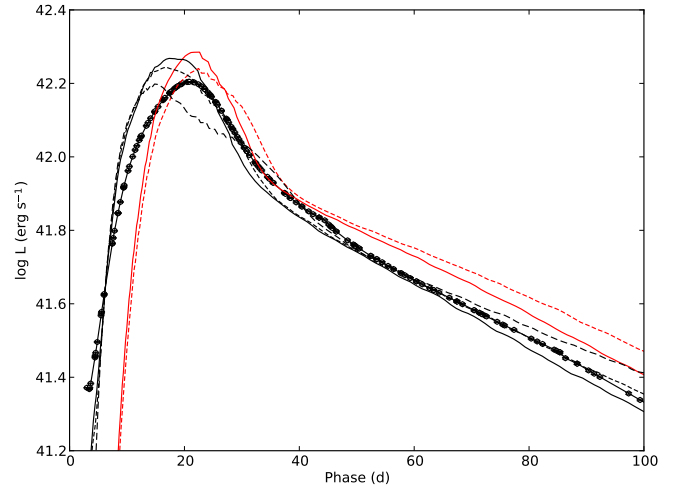
MIR BCs are <±0.1 mag during the 100-400 days period (Appendix C) and therefore the optical to MIR pseudo-bolometric lightcurve is well suited to trace the effects on the bolometric lightcurve. As M_X-M_Y=BC$_Y$-BC$_X$, a colour like quantity is well suited to constrain the parameters affecting the BCs. We prefer to use M_X-M$_{Bol,P}$, where M$_{Bol,P}$ is the optical to MIR pseudo-bolometric magnitude, but a quantity based only on photometric magnitudes is probably of more generic use. Figure 22 shows the M$_{Bol,P}$ normalized magnitudes for selected bands and selected parameter model families. The mass of ejected ^{56}Ni is not varied in the J14 models, mainly affects the bolometric lightcurve, and to first order corresponds to a scaling of the pseudo-bolometric and photometric lightcurves (Appendix C). Therefore we have normalized these in Figs. 18, 19 and 20 with the decay chain luminosity of the ejected mass of ^{56}Ni which, to first order, removes the dependence on this parameter.

Initial mass Affects both the bolometric lightcurve and the BCs. Comparison of the <500 days model and observed optical to MIR pseudo-bolometric lightcurves clearly exclude the 17 $M_\odot$ model (Figs. 18 and 21). Due to larger optical depths for the thermal radiation and the γ-rays in this model neither the diffusion peak (too wide) nor the late tail luminosity (too high) is well reproduced. There is no 17 $M_\odot$ model with medium mixing but this would only increase the discrepancy (see below). The [O I] 6300,6364 Å line, which is sensitive to the initial mass (J14), contributes ~50 percent of the R band flux and the effect on BC$_R$ is <0.41 mag. There is however a degeneracy with the effects of molecular cooling and positron trapping (Appendices C.4 and C.5) and neither R-M$_{Bol,P}$ nor the other M$_{Bol,P}$ normalized magnitudes show a clear separation of the model families differing in initial mass. The effect on the [O I] 6300,6364 Å flux is larger than on the BC and corresponds to a ~1 mag difference in the R band magnitudes. As seen in Fig. 20 there is a clear separation of the R band 17 $M_\odot$ and 12-13 $M_\odot$ model families. At <300 days the constraint from R band photometry on the initial mass is at least as good as the one obtained from the optical to MIR pseudo-bolometric lightcurve. The choice of the initial mass is mainly motivated by the agreement with nebular spectra
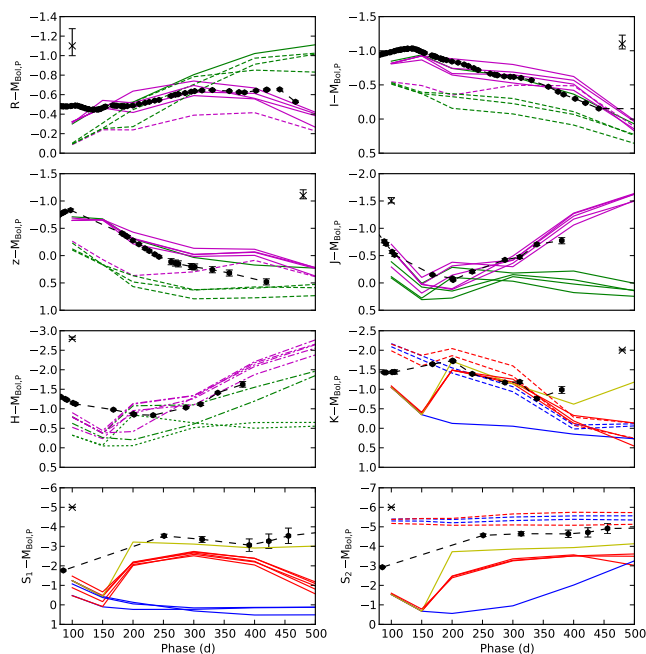
Fig. 22. 100-500 days observed (black circles) and J14 model $M_{Bol,P}$ normalized R, I, z, J, H, K, S_1 and S_2 magnitudes for selected parameter families. The model parameter families are displayed as follows: complete molecule cooling (solid lines), no molecule cooling (dashed lines), high density contrast (dotted lines), low density contrast (dashed-dotted lines), local positron trapping (magenta), non-local positron trapping (green), τ_{dust}=0 (blue), τ_{dust}=0.25 (red), τ_{dust}=0.44 (yellow). 17 $M_\odot$ and medium mixing models are not displayed. To help reading the figures we display fitted magnitudes (Sect. 2.1) for well sampled bands. The error bars arising from the extinction is marked in the upper left or right corner.

discussed in J14, but the optical to MIR pseudo-bolometric and R band lightcurves seem to exclude a 17 $M_\odot$ model.

Macroscopic mixing Affects both the bolometric lightcurve and the BCs. Comparison of the <500 days model and observed optical to MIR pseudo-bolometric lightcurves clearly exclude medium mixing models (Figs. 18 and 21). Due to the more centrally concentrated Fe/Co/He material in these models the rise to peak luminosity is much worse reproduced (too late) and the late tail luminosity also differ (too high). The effect on the BCs is mostly small (Appendix C.2) and none of the $M_{Bol,P}$ normalized magnitudes show a clear separation of the model families differing in macroscopic mixing. The choice of strong mixing is motivated by the optical to MIR pseudo-bolometric lightcurve and in particular the rise to peak luminosity. Naively this is in contradiction with the small size of the Fe/Co/He line emitting region estimated in Sect. 3.2. However, the amount of high velocity Fe/Co/He material does not necessarily need to be high to reproduce the rise to peak luminosity and further modelling is needed to resolve this issue.

Density contrast Only significantly affects the BCs. In general the effect on the BCs is small but there is a strong effect on BC_H at >300 days, caused by the [Si I] 16450 Å line. However, there is a degeneracy with a similar effect on BC_H caused by the positron trapping (see below) and it is not possible to constrain the density contrast alone. Our NIR coverage ends at ~400 days

but H-$M_{Bol,P}$ does not favour models with low density contrast and non-local positron trapping (Fig. 22). The choice of a high density contrast is mainly motivated by the agreement with nebular spectra discussed in J14 and is also consistent with the upper limit on the oxygen zone filling factor of ~0.07 derived from small scale fluctuations in the [O I] 6300,6364 Å and Mg I] 4571 Å lines in Sect. 3.6.

Positron trapping Only significantly affects the BCs. The effect is quite prominent at late times when the positrons start to dominate the energy deposition, because locally trapped positrons deposit all their energy in the low temperature Fe/Co/He zone. This results in redder emission and the luminosity of lines originating from this zone is boosted whereas the luminosity of lines originating from other zones is reduced. Due to this the pseudo-bolometric BCs, and thus the pseudo-bolometric lightcurves, decrease faster at >300 days for models with local trapping, which is in better agreement with the observed pseudo-bolometric lightcurves (Fig. 19). We find particularly strong line effects in BC_J and BC_H at >300 days caused by the [Fe II] 12567 Å and [Fe II] 16440 Å lines, respectively. As discussed above the effect on BC_H is degenerate with a similar effect caused by the density contrast. Our NIR coverage ends at ~400 days but J-$M_{Bol,P}$ seems to be in better agreement with models with local positron trapping (Fig. 22). The choice of local positron trapping is motivated by the better fit to the pseudo-bolometric lightcurves and the J-$M_{Bol,P}$ evolution at >300 days. The constraints obtained from nebular spectra are not conclusive (J14).

Molecule cooling Only affects the BCs and results in a redistribution of cooling emission from the O/C and O/Si/S zones to the CO and SiO molecular bands. Our simplified treatment is described in Appendix C.5. The effect is strong in the S_2 band, which overlaps with the CO fundamental and the SiO first overtone bands, and BC_{S_2} is 2-4 mag larger for models with complete molecule cooling. As compared to observations S_2-$M_{Bol,P}$ is 0.5-1.0 mag too bright for models with complete molecule cooling and 0.5-1.5 mag too faint for models without molecule cooling but with dust (Fig. 22). For models with neither molecule cooling nor dust S_2-$M_{Bol,P}$ is 2-4 mag too faint and these seem to be excluded. There is a significant effect also in the K band which overlaps partly with the CO first overtone band. This effect is degenerate with the effect of dust but as we have NIR spectra we can disentangle these contributions. The observed CO first overtone emission (Sect. 3.3) implies some amount of CO cooling in the O/C zone and some contribution to the S_2 flux from CO fundamental band emission. However, the observed emission at 206 days is ~3 mag fainter than in models with complete molecule cooling so either the amount of CO cooling is small or the CO fundamental to first overtone band ratio differs from that assumed in the models (Appendix C.5). The contribution from the observed CO first overtone emission to the K band flux is negligible (Sect. 3.3). We find particularly strong line effects in BC_I and BC_z at <300 days caused by the Ca II 8498,8542,8662 Å and [C I] 8727 Å lines. The former is affected by SiO cooling and the latter by CO cooling but as both contributes to both the I and z bands these effects can not be disentangled. The observed I-$M_{Bol,P}$ and z-$M_{Bol,P}$ show a better agreement with models without molecule cooling (Fig. 22). We have chosen no molecule cooling for the optimal model but neither this scenario nor complete molecule cooling shows a satisfactory agreement with observations.

Dust Only affects the BCs. As the dust absorbs the still quite hot radiation from the SN and re-emit it at a much lower temperature there is a general tendency for decreased optical emission and increased K and MIR emission. Our simplified treatment is described in Appendix C.6 where the optical pseudo-bolometric lightcurve is used to constrain the optical depth and fits to the K and S_1 bands is used to constrain the temperature. As we know that CO first overtone emission contributes negligible to the K band flux (see above) the observed excess can be solely attributed to dust emission. In models with dust, the optical BC becomes 0.2-0.3 mag smaller at 200 days, depending on the optical depth, and simultaneously, BC_K and the MIR BCs becomes ~1 and 2-3 mag larger, respectively, depending on the optical depth and the temperature. As explained in Appendix C.6 most models with dust, as the optimal model, have τ_{dust}=0.25 and the temperature is constrained to evolve as for optically thick, homologously expanding, dust clumps. These models show a reasonable (and much improved as compared to models without dust) agreement with observations (Figs. 19 and 22). The drop in the optical pseudo-bolometric lightcurve and S_1-$M_{Bol,P}$ are not fully reproduced however and the temperature evolution does not agree with observations (Appendix C.6). The tweaked optimal model (12F), for which τ_{dust} has been increased to 0.44, to fully reproduce the drop in the optical pseudo-bolometric lightcurve, and where the constraint on the temperature evolution has been relaxed, shows an improved and overall good agreement with observations however (Figs. 19 and 22). This shows, most importantly, that not only are the drop in the optical pseudo-bolometric lightcurve and the increase in BC_K and the MIR BCs simultaneous, the absorbed luminosity is also in good agreement with the emitted. S_2-$M_{Bol,P}$ is underproduced with 0.5-1.0 mag by the tweaked optimal model (and with more by the other models) which, as discussed above, suggests a contribution from molecule emission.

4.3. Hydrodynamical modelling of the <400 days bolometric lightcurve

Here we extend the temporal coverage of the hydrodynamical model grid to 400 days (which is the period for which we have full U to S_2 coverage), and make a fit of the observed optical to MIR pseudo-bolometric lightcurve of SN 2011dh to this extended model grid. The 100-400 days bolometric lightcurves are calculated using HYDE whereas the 100-400 days optical to MIR bolometric corrections are determined with the steady-state NLTE code. As in Sect. 4.1 we assume the bolometric correction to be negligible during the 0-100 days period. The fitting is done by minimization of the square of the relative residuals, giving equal weights to the diffusion phase lightcurve, the early tail lightcurve, the late tail lightcurve and the early photospheric velocity evolution. This weighting scheme gives less weight to the photospheric velocities, which makes some sense as we have additional information about the lightcurve.

To find how the bolometric correction varies in the parameter space of the hydrodynamical grid is not computationally feasible so we have to seek another solution. We take advantage of the fact that the optical to MIR bolometric correction varies with <±0.1 mag between the J14 steady-state NLTE models during the 100-400 days period (Appendix C), and use the correction for the optimal steady-state NLTE model for all hydrodynamical models. However, as the J14 models cover a restricted volume of the hydrodynamical parameter space, we need to justify this choice further. It is reasonable to assume that the bolometric correction depends mainly on the energy deposition per unit
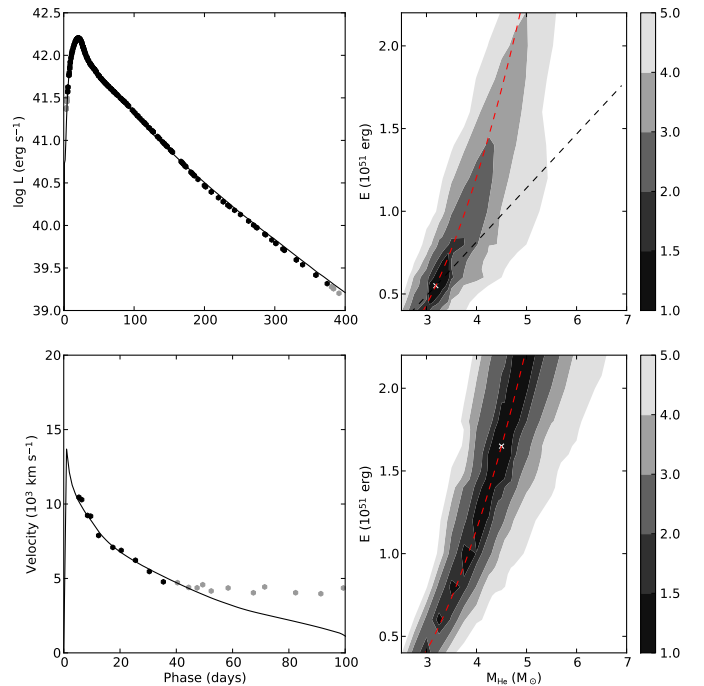
Fig. 23. Left panels: optical to MIR pseudo-bolometric lightcurve (upper right panel) and photospheric velocity evolution (lower right panel) for the optimal model as compared to the observed optical to MIR pseudo-bolometric lightcurve and velocity evolution for the absorption minimum of the Fe II 5169 Å line for SN 2011dh. Observations not included in the fit are displayed in grey. Right panels: Contour plots showing the standard deviation in the fit, normalized to that of the optimal model, projected onto the E-M_{He} plane for the case where the photospheric velocities were used (upper left panel) and not used (lower left panel). We also show the constraints M_{ej}/E=const (blue) and M_{ej}^2/E=const (red) provided by the photospheric velocity evolution and the bolometric lightcurve, respectively.

mass (determining the heating rate) and the density (determining the cooling rate). Furthermore, we know beforehand, that models giving a bad <100 days fit will not give a good <400 days fit. Inspecting the J14 models and the hydrodynamical models with a normalized standard deviation in the <100 days fit less than 3, we find that these hydrodynamical models do not span a wide range in mass averaged density or energy deposition per mass, and that the NLTE models cover about half of this region. Although these quantities evolve quite strongly with time, they scale in a similar way for all models and this conclusion holds for the full 100-400 days period. The effect of not varying the steady-state NLTE parameters that do not map onto the hydrodynamical parameter space (dust, molecule cooling, positron trapping and density contrast) is harder to constrain. The small spread in the optical to MIR bolometric correction for the J14 models during the 100-400 days period make this caveat less worrying though.

Figure 23 shows the optimal model optical to MIR pseudo-bolometric lightcurve and photospheric velocity evolution compared to the observed optical to MIR pseudo-bolometric lightcurve and velocity evolution for the absorption minimum of the Fe II 5169 Å line. The parameters of the optimal model are E=$0.55^{+0.42}_{-0.15}\times10^{51}$ erg, M_{He}=$3.31^{+0.72}_{-0.18}$ $M_\odot$, M_{Ni}=$0.075^{+0.028}_{-0.020}$ $M_\odot$ and Mix_{Ni}=$1.00^{+0.22}_{-0.03}$, in close agreement with the results from the <100 days bolometric lightcurve. The lower left panel of Fig. 23 shows a contour plot of the standard deviation in the fit,

normalized to that of the optimal model, as a function of helium core mass and explosion energy. The solution is slightly better constrained in helium core mass and slightly worse constrained in explosion energy, as compared to the <100 days fit, which probably just reflects the smaller weight given to the photospheric velocities. The lower right panel of Fig. 23 show the corresponding contour plot for the case when the fitting was done using the lightcurve alone. As discussed in E14b such a fit is completely degenerate along the M_{ej}^2/E=const curve using the <100 days lightcurve and apparently this is also the case using the <400 days lightcurve. The main achievement using the <400 days lightcurve is to prove that we get a good fit and similar best fit values as for the <100 days lightcurve. Among other things this shows that other isotopes than ^{56}Co does not contribute substantially before 400 days.

4.4. The 500-750 days bolometric lightcurve

Figure 24 shows the 200-750 days observed optical to MIR and optical pseudo-bolometric lightcurves compared to the bolometric lightcurve, deposited ^{56}Co γ-ray and positron luminosity and deposited ^{57}Co luminosity for the optimal steady-state NLTE model. The optimal hydrodynamical model produces very similar results. Between 467 and 601 days there is no observations and we can only speculate about the evolution but between 601 and 732 days there is both optical and MIR observations. It is evident from the figure, that the deposited ^{56}Co luminosity is dominated by the positron contribution after ~450 days, and that the observed 600-750 days pseudo-bolometric lightcurves are unlikely to be powered by the γ-rays emitted in the ^{56}Co decay. Shivvers et al. (2013) suggested that the SN has entered a phase powered by the positrons emitted in the ^{56}Co decay after 300-350 days. Given our results, this suggestion seems to be roughly correct in the sense that the positron contribution dominates the deposited luminosity after ~450 days. However, as we discuss below, it is not clear that the positron contribution dominates the emitted luminosity, because there is a number of processes that could provide additional energy sources.

There is observational evidence for additional energy sources from the observed pseudo-bolometric lightcurves. The decline rates of the pseudo-bolometric lightcurves, as measured between 467 and 732 days, is 0.007 mag day^{-1}, significantly lower than the decay rate of ^{56}Co. As discussed in Sect. 4.2, the optimal steady-state NLTE model has local positron trapping to best fit the >300 days photometric and pseudo-bolometric lightcurves. This implies an increasing contribution from the low temperature Fe/Co/He zone (Sect. 4.2), in turn implying an increasing bolometric correction. However, the ratio of the observed optical luminosity and the bolometric luminosity of the optimal steady-state NLTE model, increases from 0.33 to 0.65 between 467 and 732 days, in contradiction with this expectation.

If the recombination time scales become longer than the time scale of the ^{56}Co decay, the steady-state assumption required for the NLTE modelling is no longer valid. Some fraction of the deposited radioactive decay energy will then build up a reservoir of ionization energy, which through recombination emission could eventually dominate the emitted luminosity. This process, called freeze-out, is expected to occur first in the hydrogen and then in the helium envelope, and is an example of time-dependent effects that might violate the steady-state assumption in late phases. We use a time-dependent NLTE code (Kozma & Fransson 1992, 1998a,b) to test this assumption and find that time-dependent effects start to become important at ~600 days,
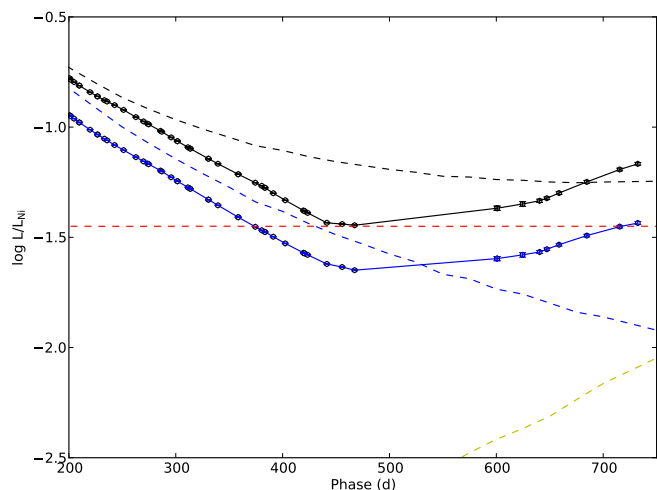
Fig. 24. Optical to MIR (black dots) and optical (blue dots) pseudo-bolometric lightcurves compared to the bolometric lightcurve (black dashed line), deposited ^{56}Co γ-ray (blue dashed line) and positron (red dashed line) luminosity and deposited ^{57}Co luminosity (yellow dashed line) for the optimal steady-state NLTE model (12C). The lightcurves have been normalized to the radioactive decay chain luminosity of 0.075 $M_\odot$ of ^{56}Ni.

and after ~800 days they provide a dominant and increasing contribution to the flux in these bands. The 678 day spectrum of SN 2011dh presented by Shivvers et al. (2013), shows features not present in our last optical spectra that could be identified as the He I 6678 Å and 7065 Å lines, whereas the strong feature identified as Na I 5890,5896 Å by the authors could have a significant contribution from, or be fed by, the He I 5876 Å line. This is consistent with a substantial contribution from helium recombination emission due to freeze-out in the helium envelope.

CSM interaction became the dominant energy source at ~300 days for SN 1993J, giving rise to broad box-like Hα and Na I 5890,5896 Å lines and a considerable flattening of the lightcurves. The 678 day spectrum of SN 2011dh presented by Shivvers et al. (2013) shows a feature that they interpret as broad box-like Hα emission, but no broad box-like Na I 5890,5896 Å emission is seen. The interpretation of the broad feature as Hα emission is far from clear, as a number of other lines may contribute in this wavelength range (including the [N II] 6548,6583 Å line discussed in Sect. 3.2 and the He I 6678 Å line mentioned above), and the feature is much weaker than for SN 1993J at a similar epoch. Additional energy sources could also be provided by the decay of radioactive isotopes other than ^{56}Co. In the optimal steady-state NLTE model, the fractional luminosity deposited by the ^{57}Co decay is ~10 percent at 700 days and increasing. A higher mass of ejected ^{57}Co than assumed in the optimal steady-state NLTE model would help explain the observed evolution and can not be excluded. In summary we find observational and theoretical evidence that the contribution from positrons emitted in the ^{56}Co decay may not dominate the observed 600-750 days luminosity. A substantial contribution from time-dependent effects in this phase is likely whereas contributions from CSM interaction and other radioactive isotopes can not be excluded.

5. Discussion

5.1. Dust, molecules and the MIR evolution

There is a strong increase in the fractional MIR luminosity between 100 and 250 days during which a decrease in the fractional optical luminosity and an increase in the decline rate of the optical pseudo-bolometric lightcurve is also observed (Sect. 2.3). The increase in fractional luminosity affects both MIR bands as well as the K band (Fig. 6). This behaviour is reminiscent of dust formation in the ejecta, where the dust would absorb the still quite hot radiation from the SN and re-emit it at a much lower temperature, and has previously been observed in SN 1987A (Suntzeff & Bouchet 1990). There is an excess in the S_2 band, as compared to blackbody fits, developing already during the first hundred days however (E14a). The S_2 band overlaps with both the CO fundamental band and the SiO first overtone band so in this band molecule emission provides an alternative or complementary explanation. We detect a modest amount of CO first overtone emission at 206 days (Sect. 3.3), which implies at least some contribution from CO fundamental band emission to the S_2 flux. The contribution from CO first overtone emission to the K band flux at these epochs is negligible though.

Our treatment of dust in the steady-state NLTE modelling (Sect. 4.2.4, Appendix C.6) is simplified and assumes the dust to reside in optically thick, homologously expanding clumps. This model fails to explain the temperature evolution however, and the temperature is determined from blackbody fits to the K and S_1 bands. The tweaked optimal model (12F), which has τ_{dust}=0.44 well reproduce both the drop in the optical pseudo-bolometric lightcurve and the increase in the fractional K and S_1 luminosities. This shows, most importantly, that the absorbed and emitted luminosities are in good agreement and suggests a scenario where the emission arise from nearby, newly formed dust, presumably in the ejecta. Further support for this scenario is gained from spectra. In Fig. 25 we show the observed NIR spectra from ~200 days compared to NIR spectra for the tweaked optimal model and model 12E (without dust) at 200 days as well as the dust emission component for the tweaked optimal model. The observed flux at the absorbtion minimum of the He I 20581 Å line is a factor of ~2 below the model dust emission level, which suggests this emission to originate from ≲10000 km s^{-1} and disfavours a thermal echo from heated CSM dust. Helou et al. (2013) showed that a thermal echo from heated CSM dust could explain the early (<100 days) MIR evolution but were unable to reproduce the late evolution. Regardless of the location of the dust, the behaviour of the K and S_1 lightcurves is hard to explain without dust emission. The contribution from CO overtone emission to the K band is negligible (Sect. 3.3) and at 250 days the discrepancy between observations and models without dust is ~1 and ~3 mag in the K and S_1 bands, respectively. Furthermore, the spectral comparison in Fig. 25 shows that the excess is mainly affecting the continuum and extends down to ~15000 Å at ~200 days. The small blue-shift in the [O I] 6300,6364 Å line at 415 days (Sect. 3.5) and the lack of a physical model for the temperature evolution are caveats though. A MIR excess developing between 100 and 250 days is also observed for SN 1993J (Sect. 2.3). The cause of this excess was suggested by Matthews et al. (2002) to be dust but the absence of an increase in the optical pseudo-bolometric decline rate indicates that, if this emission is due to dust, it would rather arise from heated CSM dust. Except for SNe 2011dh and 1993J we have found no reports of dust emission in Type IIb or stripped envelope SNe in the literature.
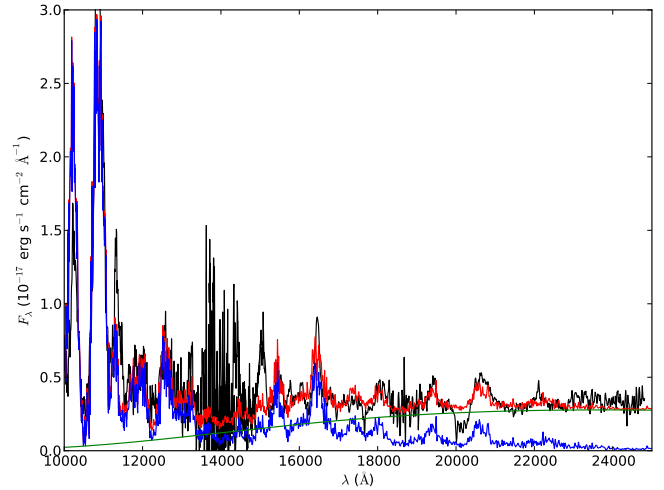
Fig. 25. Observed zJ and HK spectra at 198 and 206 days (black) compared to NIR spectra for the tweaked optimal model (12F; red) and model 12E (blue), which differs only in that τ_{dust}=0. The observed spectra were flux calibrated with the interpolated observed J, H and K magnitudes at 200 days and we also show the dust emission component for the tweaked optimal model (green).

Our treatment of molecules in the NLTE modelling (Sect. 4.2.4, Appendix C.5) only includes two extremes, no emission or complete dominance of the cooling in the O/C and O/Si/S zones by CO and SiO emission. This has some support in that molecules are efficient coolers and tend to dominate the cooling once formed, but is nevertheless simplified. Therefore it is not entirely surprising that the constraints derived do not give full support to either scenario. The dust contribution is found to be insufficient to explain the S_2 magnitudes and these are 0.5-1.0 mag too bright as compared to the tweaked optimal model (12F). On the other hand, as compared to models with complete molecule cooling, they are 0.5-1.0 mag too faint. The evolution of the I and z bands, which are sensitive to lines originating in the O/C and O/Si/S zones, suggests a modest amount of molecule cooling. The remarkable similarity between the [O I] 6300 Å and Mg I] 4571 Å line profiles, on the other hand, suggests the contributions to the [O I] 6300 Å flux from the O/C and O/Si/S zones to be modest (Sect. 3.4), in turn suggesting a considerable amount of molecule cooling. Some amount of CO cooling in the O/C zone and some contribution to the S_2 flux from CO fundamental band emission is implied by the observed CO first overtone emission at 206 days. CO emission has been reported for the Type Ic SNe 2002ew (Gerardy et al. 2002) and 2007gr (Hunter et al. 2009) but for Type Ib and IIb SNe we have found no reports of CO emission in the literature. There is a feature near 23000 Å however, in the NIR spectra of SN 1993J (Matthews et al. 2002), that could be interpreted as a modest amount of CO first overtone emission.

5.2. The nature of the progenitor star

In M11, B12, E14a, J14 and this paper we have investigated the nature of the progenitor star for SN 2011dh using a number of different and, at least partially, independent methods. In M11 we analyse direct observations of the putative progenitor by comparison of the observed magnitudes to predictions from stellar atmosphere and evolutionary models. The best match is found to be a yellow supergiant with an initial mass of 13±3 M$_\odot$ and

a radius of ~270 $R_{\odot}$. In E14a we present observations of the disappearance of this star, confirming that it was the progenitor of SN 2011dh, although the possible presence of dust in the SN ejecta (Sect 5.1) adds uncertainty to this result. In this paper we present hydrodynamical modelling, which shows that a star with a helium core mass of $3.3^{+0.6}_{-0.2}$ $M_{\odot}$, exploded with an energy of $0.50^{+0.42}_{-0.10} \times 10^{51}$ erg and ejecting $0.075^{+0.028}_{-0.013}$ $M_{\odot}$ of ^{56}Ni mixed out to high velocities, gives the best fit to the observed <400 days bolometric lightcurve and the photospheric velocity evolution. The use of a model grid allows us to determine the errors in the SN and progenitor parameters arising from the errors in the observed quantities and to constrain the degeneracy of the solution. Given this we find an upper limit on the initial mass of $\lesssim$15 $M_{\odot}$. In B12 we present hydrodynamical modelling, which shows that a low-mass (~0.1 $M_{\odot}$) and extended (200-300 $R_{\odot}$) hydrogen-rich envelope seems to be required to reproduce the observed g band lightcurve during the first 3 days. In E14a we estimate a hydrogen mass of 0.01-0.04 $M_{\odot}$ using a Monte-Carlo atmosphere code. This hydrogen mass is consistent with the B12 ejecta model, and we also find the interface between the helium core and the hydrogen rich envelope to be located at a velocity consistent with this model. In J14 and this paper we present steady-state NLTE modelling, which shows that a star with an initial mass of 12 $M_{\odot}$ well reproduces the observed 100-500 days spectral evolution and pseudo-bolometric and photometric lightcurves. Particular attention is paid to the [O I] 6300,6364 Å line, which is very sensitive to the initial mass of the star. To reproduce the flux in this line an initial mass of <17 $M_{\odot}$ seems to be required.

Overall the results obtained with the different methods are consistent and, even given the caveats of each individual method, it is likely that the progenitor star is of moderate initial mass ($\lesssim$15 $M_{\odot}$), and has a low-mass extended hydrogen rich envelope, most of which must have been lost either through stellar winds or interaction with a binary companion. The moderate mass suggests that interaction with a binary companion is needed, as stellar winds of stars in this mass range are not strong enough to expel the hydrogen envelope before core-collapse. As we show in J14 and in this paper, using steady-state NLTE modelling of nebular spectra and hydrodynamical modelling of the bolometric lightcurves, SNe 2008ax and 1993J are likely to be of similar initial mass and have similar explosion energy as SN 2011dh, although the mass of the ejected ^{56}Ni may differ significantly depending on the adopted distance and extinction. In particular, the upper bound on the initial mass for all three SNe is found to be $\lesssim$15 $M_{\odot}$, again suggesting that interaction with a binary companion have taken place. In the case of SN 1993J, this conclusion is supported by direct observations of the binary companion (Maund et al. 2004; Fox et al. 2014). Observations, that could detect or set useful constraints on the presence of a companion star for SN 2011dh, are scheduled for Cycle 21 at HST, whereas similar observations for SN 2008ax would not be feasible, due to the longer distance. Clearly there is growing evidence that the main production channel for Type IIb SNe are stars whose hydrogen envelope has been stripped by interaction with a binary companion. Modelling of the nebular spectra and hydrodynamical modelling of the bolometric lightcurves for a larger sample of Type IIb SNe, could provide further evidence for this hypothesis.

6. Conclusions

We present two years of optical and NIR photometric and spectroscopic observations for the Type IIb SN 2011dh. Together with SWIFT and Spitzer observations the data cover the UV to MIR wavelength range although the photometric coverage ends at ~100 days in UV and at ~400 days in NIR, and the spectral coverage ends at ~200 days in NIR and at ~450 days in the optical. Particular attention is paid to the bolometric and photometric lightcurves where we use steady-state NLTE modelling and hydrodynamical modelling to put constraints on the SN and progenitor parameters. We also provide a spectral analysis, mainly related to the line profiles, complementary to the steady-state NLTE modelling of nebular spectra presented in J14.

We analyse the <400 days pseudo-bolometric lightcurve of SN 2011dh using the grid of the hydrodynamical SN models presented in E14b and the fitting procedure described therein. To extend the temporal coverage of the model grid beyond 100 days we apply a bolometric correction determined with the steady-state NLTE modelling. This method allows us to determine the errors in the model parameters arising from the observed quantities and the degeneracy of the solution. The results for the <400 days period are very similar to those for the <100 days period and we find a helium core mass of $3.4^{+0.6}_{-0.3}$ $M_{\odot}$, an explosion energy of $0.55^{+0.40}_{-0.16} \times 10^{51}$ erg and a mass of ejected ^{56}Ni of $0.075^{+0.028}_{-0.017}$ $M_{\odot}$, in good agreement with our results in B12. The <100 days pseudo-bolometric lightcurves of SNe 2008ax and 1993J are also analysed and the best fit values of the helium core mass and explosion energy are similar to those of SN 2011dh. We find an upper limit on the helium core mass for all three SNe of $\lesssim$4 $M_{\odot}$, corresponding to an upper limit on the initial mass of $\lesssim$15 $M_{\odot}$. Strong mixing of the ejected ^{56}Ni is required for all three SNe to fit the rise to peak luminosity.

We analyse the 100-500 days pseudo-bolometric and photometric lightcurves of SN 2011dh using the restricted set of steady-state NLTE models presented in J14. To extend the temporal coverage of these models we construct <100 days bolometric lightcurves using HYDE (E14b) in homologous mode. The optimal 12 $M_{\odot}$ model, presented in J14 and chosen to give the best agreement with both spectra and lightcurves, shows an overall agreement with the observed photometric and pseudo-bolometric lightcurves. The optical to MIR pseudo-bolometric lightcurve seem to exclude 17 $M_{\odot}$ and medium mixing models and the optical pseudo-bolometric lightcurve and the fractional H and K luminosities at >300 days suggests local positron trapping. The simultaneous increase in the optical pseudo-bolometric decline rate and the fractional K and S_1 luminosities between 100 and 250 days is reproduced by models with a modest amount of dust in the core (τ_{dust} = 0.44). This scenario is supported by the depth of the He I 20581 Å absorption, which suggest the excess emission to arise from within ~10000 km s^{-1}. The fractional S_2 luminosity is intermediate as compared to models with no and complete molecule cooling whereas the observed CO first overtone emission at 206 days implies some amount of CO cooling in the O/C zone and some contribution to the S_2 luminosity from CO fundamental band emission.

The 500-750 days pseudo-bolometric and photometric lightcurves can not be analysed with the steady-state NLTE code as modelling with a time-dependent NLTE code (Kozma & Fransson 1992, 1998a,b) shows that the steady-state assumption is no longer valid. In the optimal steady-state NLTE model the positron contribution dominates the ^{56}Co energy deposition after ~450 days. However, there is both observational and theoretical evidence that the 500-750 days lightcurves are dominated by ad-

ditional energy sources. The decline rates are significantly lower than the decay rate of ^{56}Co and the observed optical pseudo-bolometric luminosity is ~50 percent of the bolometric luminosity in our optimal model, in contradiction with a scenario with locally trapped positrons. Modelling with the time-dependent NLTE code shows that after ~600 days time-dependent effects become important and contribute substantially to the observed luminosity. We find that a substantial contribution from CSM interaction and other radioactive isotopes is less likely but can not be excluded.

The line profiles of the important lines are analysed and we estimate progressively smaller sizes, ranging from ~3000 to ~1500 km s^{-1}, for the line emitting region of oxygen, magnesium, [Ca II] 7291,7323 Å and iron, in all compared cases smaller than those of SNe 1993J and 2008ax. Given the findings in J14, these regions would correspond to the oxygen, O/Ne/Mg, Si/S and Fe/Co/He nuclear burning zones and suggest incomplete mixing of the core material. The profiles of the [O I] 6300 Å and Mg I] 4571 Å lines show a remarkable similarity, suggesting that these lines arise from the O/Ne/Mg zone. We use repetitions of small scale fluctuations in the [O I] 6300 Å and [O I] 6364 Å lines to find a line ratio close to 3, consistent with optically thin emission, from 200 days and onwards. Applying the method of Chugai (1994) to these small scale fluctuations, we find an upper limit on the filling factor of the [O I] 6300 Å and Mg I] 4571 Å line emitting material of ~0.07 and a lower limit on the number of clumps of ~900.

This paper concludes our observational and modelling work on SN 2011dh presented in M11, B12, E14a and J14. We have applied stellar evolutionary progenitor analysis, hydrodynamical modelling, SN atmosphere modelling and steady-state NLTE modelling to our extensive set of observational data. Although a number of issues remains unsolved, the main characteristics of the SN and its progenitor star found by the different methods are consistent. The progenitor star appears to have been of moderate ($\lesssim$15 M$_\odot$) initial mass, and the 3-4 M$_\odot$ helium core surrounded by a low-mass (~0.1 M$_\odot$) and extended (200-300 R$_\odot$) hydrogen-rich envelope. In particular we have found the initial masses of SNe 2011dh, 1993J and 2008ax to be $\lesssim$15 M$_\odot$, from both hydrodynamical modelling of the early bolometric evolution and steady-state NLTE modelling of the late spectral evolution. This limit is also supported by stellar evolutionary progenitor analysis for SNe 2011dh and 1993J (Maund et al. 2004, 2011). Given that the mass-loss rates for stars in this mass range are probably not strong enough to expel the hydrogen envelope before core-collapse, a binary origin for these SNe is strongly suggested.

Appendix A: Data reductions and calibration

Appendix A.1: Imaging - 100-500 days observations

Comparison to photometry on template subtracted images shows that the background contamination is negligible before ~300 days after which we have used photometry on template subtracted images. The optical templates were constructed by PSF subtraction of the SN from observations acquired after 600 days and the NIR templates by PSF subtraction of the SN from the 339 days WHT observation, which is of excellent quality. For the last 380 days WHT observation we used PSF photometry. The accuracy of the late time photometry depends critically on the accuracy of the S-corrections. The late time Johnson-Cousins (JC) and Sloan Digital Sky Survey (SDSS) photometry were mainly obtained with the NOT but comparisons between S-corrected NOT, LT and CA 2.2m JC and SDSS observations

at ~300 days show differences at the 5 percent level suggesting that this precision is maintained. We note that in this phase S-corrections are absolutely necessary. For example the difference between the NOT and CA 2.2m *I* band observations are almost one magnitude at ~300 days if these are not applied, mainly because of the strong [Ca II] 7291,7323 Å and Ca II 8498,8542,8662 Å lines. AT S-corrections have been determined using filter response functions constructed as outlined in E14a. The late time 2MASS photometry was obtained with a number of different telescopes and although the sampling is sparse the shape of the lightcurves suggests that the errors in the S-corrections are modest.

Appendix A.1.1: Imaging - >600 days observations

The results for the post 600 days observations have been adopted from the pre-explosion difference imaging presented in E14a, assuming that the remaining flux at the position of the progenitor originates solely from the SN. The observations were S-corrected using the 678 day spectrum of SN 2011dh presented by Shivvers et al. (2013). Clearly the uncertainties arising from the procedure used could be significant but the ≲0.2 mag difference between the S-corrected NOT *V* and HST *F555W* (Van Dyk et al. 2013) observations gives some confidence in the results.

Appendix A.1.2: Imaging - Spitzer Telescope observations

For the >100 days photometry we used a small aperture with a 3 pixel radius and a correction to the standard aperture given in the IRAC Instrument Handbook determined from the images. The <700 days photometry previously published by Helou et al. (2013) agrees very well with our photometry, the differences being mostly ≲5 percent. The 391 days S_2 magnitude differs by ~0.5 mag, though.

Appendix B: Line measurements

Appendix B.1: Line emitting regions

To estimate the sizes of the line emitting regions we fit the line profile of a spherically symmetric region of constant line emissivity, optically thin in the line (no line scattering contribution) and with a constant absorptive continuum opacity, to the observed line profile. The fitting is done by an automated least-square based algorithm. The absorptive continuum opacity is included to reproduce the blue-shifts observed in some line profiles. This method gives a rough estimate of the size of the region responsible for the bulk of the line emission and is not applied if scattering appears to contribute significantly to the line profile. Some lines arise as a blend of more than one line which has to be taken into account. The [O I] 6300 Å flux was calculated by iterative subtraction of the [O I] 6364 Å flux, from the left to the right, using $F_{6300}(\lambda) = F_{6300,6364}(\lambda) - F_{6300}(\lambda - \Delta\lambda)/R$, where $\Delta\lambda$ is the wavelength separation between the [O I] 6300 Å and 6364 Å lines and R the [O I] 6300,6364 Å line ratio. This ratio was assumed to be 3, as is supported by estimates based on small scale fluctuations in the line profiles (Sect. 3.6). In all other cases, where the line ratios of the blended lines are not known, we make a simultaneous fit with the line ratios as free parameters, assuming a common size of the line emitting regions.

Appendix B.2: Line asymmetries

To estimate the asymmetry of the line profiles we calculate the first wavelength moment of the flux (center of flux). The continuum level is determined by a linear interpolation between the minimum flux levels on the blue and red sides within a region set to ±6000 km s^{-1} for most of the lines, ±10000 km s^{-1} for the Ca II 8662 Å line and ±3000 km s^{-1} for the [Fe II] 7155 Å line. The rest wavelength is assumed to be 6316 Å and 7304 Å for the [O I] 6300,6364 Å and [Ca II] 7291,7323 Å lines, respectively, as is appropriate for optically thin emission. The rest wavelength is assumed to be 5896 Å and 8662 Å for the Na I 5890,5896 Å and Ca II 8498,8542,8662 Å lines, respectively, as is appropriate for optically thick emission.

Appendix C: NLTE model parameters.

Here we discuss the steady-state NLTE model parameters and their effects on the model lightcurves. The treatment of molecule cooling and dust is described in detail whereas the other parameters are described briefly for convenience. Full details on these parameters are given in J14. To analyse the lightcurves we make use of a split into a bolometric lightcurve and a bolometric correction (BC). In terms of these quantities the photometric and pseudo-bolometric magnitudes are given by M=M$_{Bol}$-BC (where pseudo-bolometric magnitude refer to the pseudo-bolometric luminosity on the bolometric magnitude system). This split is most useful for the analysis of the model lightcurves as the bolometric lightcurve depends only on the deposition of radioactive decay energy whereas the BCs depend on how this energy is processed. There is a subtlety here though as even in steady-state the bolometric luminosity does not equal the energy deposition because some energy is lost due to scattering in the ejecta. This difference is small (<0.05 mag) and will be ignored in the subsequent discussion. As the bolometric lightcurves depend only on the energy deposition they are independent of molecule cooling and dust, which only affects the processing of the deposited energy. As discussed in Sects. C.3 and C.4, within the parameter space covered by the J14 models, the bolometric lightcurves are only weakly dependent of the density contrast and the positron trapping. Therefore the bolometric lightcurves depend significantly only on the initial mass and the macroscopic mixing, whereas the BCs may depend on all model parameters. Figure C.1 shows the 100-500 days bolometric lightcurves for the J14 model families differing in initial mass and macroscopic mixing. The bolometric lightcurves have been normalized with the decay chain luminosity of the mass of ejected ^{56}Ni. This is convenient as the bolometric lighcurves then becomes independent of this parameter. The mass of ejected ^{56}Ni is not varied in the J14 models as it mainly affects the bolometric lightcurve and, to first order, corresponds to a scaling of the pseudo-bolometric and photometric lightcurves. Figures C.2 and C.3 shows the pseudo-bolometric and photometric BCs for the J14 models. The optical to MIR BCs show small differences (<±0.1 mag) during the 100-400 days period, but these subsequently increase towards ±0.25 mag at 500 days. At 100 days the optical to MIR BC is >-0.15 mag and it is likely that this holds at <100 days as well. The optical BCs, on the other hand, show larger differences, mainly because molecule cooling and dust affects the distribution of the flux between the optical and the MIR.
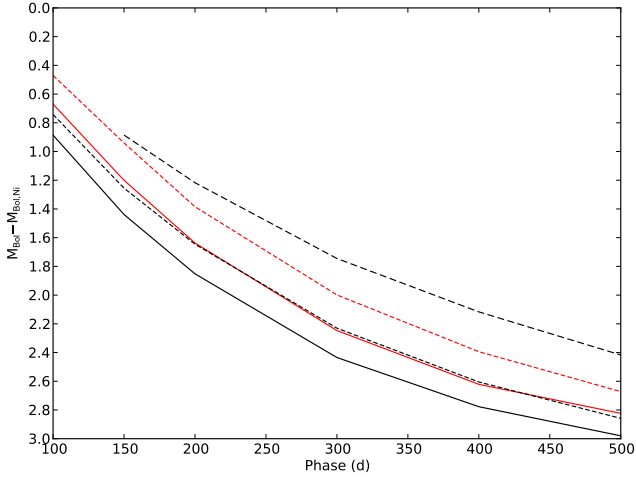
Fig. C.1. 100-500 days bolometric lightcurves for the J14 model normalized to the radioactive decay chain luminosity of 0.075 M$_\odot$ of ^{56}Ni. The model families differing in initial mass and macroscopic mixing are displayed as follows: 12 M$_\odot$ (solid lines), 13 M$_\odot$ (short dashed lines), 17 M$_\odot$ (long dashed lines), medium mixing (red), strong mixing (black).
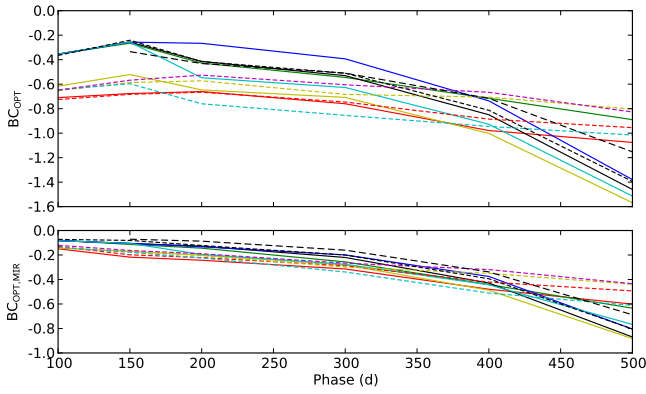
Fig. C.2. 100-500 days optical (upper panel) and optical to MIR (lower panel) BCs for the J14 models. The models are displayed as follows; 12A (red solid line), 12B (green solid line), 12C (black solid line), 12D (yellow solid line), 12E (blue solid line), 12F (black dashed-dotted line), 13A (red short-dashed line), 13C (yellow short-dashed line), 13D (cyan short-dashed line), 13E (magenta short-dashed line), 13G (black short-dashed line), 17A (black long-dashed line).

Fig. C.3. 100-500 days photometric BCs for the J14 models. The models are displayed as in Fig. C.2.

<0.49 and <0.67 in model 12C, 13G and 17A, respectively. The difference in BC$_{6300,6364}$ between model 12C and 17A is ∼1 mag and the corresponding difference in BC$_R$ is <0.41 mag. There is also a degeneracy with the effects of positron trapping and molecule cooling on BC$_R$ (Appendices C.4 and C.5), which are of similar magnitude. The difference in [O I] 6300,6364 Å flux between model 12C and 17A is ∼1.5 mag and the corresponding difference in the R band magnitudes ∼1 mag. This difference is larger than the difference in the bolometric lightcurve and, provided the mass of ejected ^{56}Ni is known, R band magnitudes might prove useful to constrain the initial mass.

Appendix C.1: Initial mass

The initial mass may affect both the energy deposition (bolometric lightcurve) and the way this energy is processed (BC). Comparing the bolometric lightcurves and the pseudo-bolometric BCs for the optimal model (12C) and models 13G and 17A, which differs only in the initial mass, we find that the average difference in the bolometric lightcurve is 0.62 mag, whereas the average differences in the optical to MIR and optical BCs are 0.08 and 0.11 mag, respectively. There is an increasing spread in the optical to MIR and optical BCs developing with time though and at 500 days the differences are 0.18 and 0.31 mag, respectively.

The average difference in the photometric BCs is 0.23 mag but varies quite a lot with band and phase and the maximum difference is 1.01 mag. As discussed in J14 the [O I] 6300,6364 Å line is particularly sensitive to the initial mass. The fraction of the R band flux originating from [O I] 6300,6364 Å line is <0.38,

Appendix C.2: Macroscopic mixing

The degree of macroscopic mixing may affect both the energy deposition (bolometric lightcurve) and the way this energy is processed (BC). Comparing the bolometric lightcurves and the pseudo-bolometric BCs for models 13A and 13C, which differ only in the degree of macroscopic mixing, we find that the average difference in the bolometric lightcurve is 0.29 mag, whereas the average differences in the optical to MIR and optical BCs are 0.04 and 0.12 mag, respectively.

The average difference in the photometric BCs is 0.14 mag but varies quite a lot with band and phase and the maximum difference is 0.42 mag. There is a general trend in the BCs corresponding to bluer emission for model 13C (strong mixing). This is a bit surprising as the lower energy deposition per mass in strongly mixed models naively would result in lower temperatures and redder emission. However, although the temperature decrease in the core zones, the increased energy deposition in

the helium envelope, which has a higher temperature and also bluer non-thermal emission, seems to counterweight this effect and the end result is bluer emission.

Appendix C.3: Density contrast

The density contrast may affect both the energy deposition (bolometric lightcurve) and the way this energy is processed (BC). However, in the J14 models the energy deposition is only weakly dependent of the contrast factor as the optical depths to γ-rays and non-locally trapped positrons for individual Fe/Co/He clumps are $\ll 1$ at times when these are contributing substantially to the energy deposition. Comparing models 13C and 13E, that differ only in the density contrast, the difference in energy deposition is <0.03 mag. Furthermore, there are reasons to suspect that the differences in the BCs are small as well as the fraction of the deposited energy going into heating, ionization and excitation is not particularly sensitive to the density (Kozma & Fransson 1992). Comparing the pseudo-bolometric BCs of models 13C and 13E, these are indeed very similar, but show a small (<0.08 mag) difference.

As discussed in J14 the Mg I 4571 Å line is sensitive to the density contrast and the fractional flux differs with ~1 mag at 300 days between model 13C and 13E. However, the fractional Mg I 4571 Å flux in the B band is <0.09 and <0.24 for model 13C and 13E, respectively, so the difference in BC_B is only <0.24 mag. As seen in Fig. C.3 there is a strong difference in BC_H developing at >300 days and at 500 days the difference is ~1.2 mag. Inspection of the models reveals that this difference is caused by the [Si I] 16450 Å line which becomes very strong in high density contrast models.

Appendix C.4: Positron trapping

The positron trapping may affect both the energy deposition (bolometric lightcurve) and the way this energy is processed (BC). However, in the J14 models the energy deposition is, in most cases, independent of the positron trapping as the optical depths to non-locally trapped positrons are, in most cases, $\gg 1$. Exceptions are the strongly mixed models with non-locally trapped positrons where a small (<0.05 mag) difference develops at late times. Positron trapping only affects the BCs when the fraction of radioactive decay energy deposited by the positrons becomes significant, and before this models with locally or non-locally trapped positrons are indistinguishable.

Comparing the optimal model (12C) and model 12B, which differs only in the positron trapping, the pseudo-bolometric BCs for the optimal model gets increasingly smaller after ~300 days, when the contribution from positrons to the energy deposition starts to become significant. The reason for this is that in the optimal model all positrons are trapped in the Fe/Co/He zone. This zone has a lower temperature than other zones because of efficient cooling from the large number of iron lines, and the emission arising from this zone is redder. At 500 days the differences in the optical to MIR and optical BCs are 0.24 and 0.57 mag, respectively.

At late times we also expect lines originating from the Fe/Co/He zone to be more luminous and lines originating from other zones to be less luminous in models with local positron trapping. As discussed in J14 the [O I] 6300,6364 Å, [N II] 6548,6583 Å, [Fe II] 12567 Å, [Fe II] 12700-13200 Å and the [Fe II] 16440 Å lines are particularly sensitive to the positron trapping. Therefore we would expect BC_R, BC_J and BC_H to

be particularly sensitive and, as seen in Fig. C.3, this is also the case. Comparing the optimal model (12C) and model 12B (non-local trapping) BC_R, BC_J and BC_H starts to diverge at >200 days and at 500 days they differ with ~0.8, ~1.5 and ~0.6 mag, respectively.

Appendix C.5: Molecule cooling

Molecule cooling is included in the modelling in a simplified way, and is represented as the fraction of the (radiative and radioactive) heating emitted as molecule (CO and SiO) emission in the O/C and O/Si/S zones. This energy is then emitted as CO and SiO fundamental and first overtone band emission, represented as box line profiles between 2.25-2.45 (CO first overtone), 4.4-4.9 (CO fundamental) and 4.0-4.5 (SiO first overtone) μm. The CO first overtone band overlaps partly with the K band and the CO fundamental and SiO first overtone bands overlaps with the S_2 band whereas the SiO fundamental band lies outside the U to S_2 wavelength range. The fundamental to first overtone band flux ratios are assumed to be the same as observed for CO in SN 1987A (Bouchet & Danziger 1993). We have used two configurations, one where the fraction of the heating emitted as molecule emission has been set to one, and one where this fraction has been set to zero.

Molecule cooling only affects the way the deposited energy is processed (BC). Comparing the optimal model (12C) and model 12D, which only differs in the amount of molecule cooling, the optical BC for model 12D (complete cooling) are 0.1-0.3 mag smaller. The optical to MIR BCs, on the other hand, are similar. This reflects the fact that most of the molecule emission falls within the U to S_2 wavelength range and the flux is mainly redistributed within this wavelength range.

The effect of molecule cooling is strong in the S_2 band, which overlaps with the CO fundamental band and the SiO first overtone band, but less so in the K band which overlap partly with the CO first overtone band. BC_{S_2} is 2-4 mag larger for model 12D (complete cooling) as compared to the optimal model (12C) whereas BC_K is less affected, being $\lesssim 1$ mag larger for model 12D at early times. Molecule cooling also determines the fraction of the (radiative and radioactive) heating going into line emission in the O/C and O/Si/S zones. Therefore we expect thermally excited lines in these zones to be sensitive to the amount of molecule cooling. In particular CO cooling affects the [O I] 6300,6364 Å and [C I] 8727 Å lines whereas SiO cooling affects the [Ca II] 7291,7323 Å and [S I] 10820 Å lines and, at early times, the Ca II 8498,8542,8662 Å line. BC_I and BC_z differ at <400 days and are ~0.5 mag smaller at <200 days for model 12D (complete cooling). BC_R differs throughout the evolution and is ~0.3 mag smaller at <300 days for model 12D.

Appendix C.6: Dust

Dust is included in the modelling in a simplified way, and is represented as a gray absorptive opacity in the core zones. The absorbed luminosity is re-emitted as blackbody emission from a homologously expanding surface, representing a number of optically thick dust clouds. The fractional area of this surface x_{dust}, as compared to the area of the core, is a free parameter in the modelling, and determines the temperature of the emitted blackbody radiation. Note that our treatment of dust absorption and emission is only self-consistent if the number of dust clouds is large and the filling factor of those is small. The dust emission

is treated separately from the modelling and is added by post-processing of the model spectra.

We find the presence of dust with an optical depth of 0.25 after 200 days to approximately match the behaviour of the optical pseudo-bolometric lightcurve while still producing negligible blue shifts in the line profiles. The value of x_{dust} was derived by minimization of the sum of squares of the relative flux differences of model and observed H, K and S_1 photometry at 200, 300 and 400 days (including H only at 200 days). The S_2 band was excluded as this band might have a contribution from molecule emission whereas we know that the contribution from CO first overtone emission to the K band at 89 and 202 days is negligible. This gives a value of x_{dust} of 0.011, which corresponds to temperatures of 2000, 1096 and 669 K at 200, 300 and 400 days respectively. However, assuming a large number of dust clouds and a small filling factor, it is possible to show from the assumptions made that $\tau_{dust} = 3/4 x_{dust}$, so this value of x_{dust} is not consistent with our assumptions. In other words, the fractional area needed to reproduce the observed temperature is ~20 times smaller than the fractional area needed to reproduce the optical depth. All J14 models with dust have τ_{dust}=0.25 and x_{dust}=0.11. In addition to the J14 models we have constructed a model 12E, differing from the optimal model (12C) only in the absence of dust, by scaling the unprocessed model 12C spectra with a factor corresponding to the difference in optical depth and adding no dust emission.

To fully reproduce the drop in the optical pseudo-bolometric lightcurve between 150 and 200 days an optical depth of 0.44 is needed. Using this optical depth and relaxing the constraint on the temperature imposed by our model, we find black body temperatures of 1222, 935 and 792 K at 200, 300 and 400 days respectively. So, in addition to the inconsistency between x_{dust} and τ_{dust} the temperature evolution is not well reproduced by our model. We have therefore constructed a tweaked version of the optimal model (12C) named 12F, differing from the optimal model in that the optical depth is set to 0.44 and the temperatures to those derived above. The tweaked optimal model (12F) was constructed by scaling the unprocessed model 12C spectra with a factor corresponding to the difference in optical depth and adding the dust emission using the revised values of the dust luminosities and temperatures.

Dust only affects the way the deposited energy is processed (BC). Comparing the optimal model (12C) and models 12E and 12F, which only differs in the presence of dust after 200 days, the optical BC for the models with dust (12C and 12F) becomes 0.2-0.3 mag smaller at 200 days, roughly corresponding to the optical depth of the dust. The optical to MIR BCs are the same until ~300 days and then slowly becomes smaller for the models with dust, reflecting the decreasing temperature of the dust. The effect of dust (emission) is strong on BC_K and the MIR BCs which at 200 days becomes ~1 and 2-3 mag larger, respectively, for the models with dust (12C and 12F) and then slowly evolve according to the decreasing temperature of the dust.

Appendix D: HYDE

Here we provide a summary of the HYDE code, used in Sect. 4 to model the bolometric lightcurve. A detailed desciption is provided in E14b, where we also provide tests and comparisons to other similar codes. HYDE is a one-dimensional Lagrangian hydrodynamical code based on the flux limited diffusion approximation, following the method described by Falk & Arnett (1977) and adopting the flux limiter given by Bersten et al. (2011). The opacity is calculated from the OPAL opacity tables (Iglesias &

Rogers 1996) complemented with the low temperature opacities given by Alexander & Ferguson (1994). In addition we use an opacity floor set to 0.01 cm^2 gram^{-1} in the hydrogen envelope and 0.025 cm^2 gram^{-1} in the helium core, following Bersten et al. (2012, private communication), who calibrated these values by comparison to the STELLA hydrodynamical code (Blinnikov et al. 1998). The electron density needed in the equation of state is calculated by solving the Saha equation using the same atomic data as in Jerkstrand et al. (2011, 2012). The transfer of the gamma-rays and positrons emitted in the decay chain of ^{56}Ni is calculated with a Monte-Carlo method using the same gray opacities, luminosities and decay times as in Jerkstrand et al. (2011, 2012). The homologous behaviour have been tested by comparison to analytical solutions, the deposition of radioactive decay energy by comparison to the steady-state NLTE code described in Jerkstrand et al. (2011, 2012) and the hydrodynamical behavior by comparison to the results obatined for SN 2011dh in B12.

References

Alexander, D. R. & Ferguson, J. W. 1994, ApJ, 437, 879
Arcavi, I., Gal-Yam, A., Yaron, O., et al. 2011, ApJ, 742, L18
Benvenuto, O. G., Bersten, M. C., & Nomoto, K. 2013, ApJ, 762, 74
Bersten, M. C., Benvenuto, O., & Hamuy, M. 2011, ApJ, 729, 61
Bersten, M. C., Benvenuto, O. G., Nomoto, K., et al. 2012, ApJ, 757, 31
Blinnikov, S. I., Eastman, R., Bartunov, O. S., Popolitov, V. A., & Woosley, S. E. 1998, ApJ, 496, 454
Bouchet, P. & Danziger, I. J. 1993, A&A, 273, 451
Chugai, N. N. 1994, ApJ, 428, L17
Ergon, M., Sollerman, J., Fraser, M., et al. 2014a, A&A, 562, A17
Ergon, M., Sollerman, J., Jerkstrand, A., & Fransson, C. 2014b, In preparation
Falk, S. W. & Arnett, W. D. 1977, ApJS, 33, 515
Filippenko, A. V. & Sargent, W. L. W. 1989, ApJ, 345, L43
Fox, O. D., Azalee Bostroem, K., Van Dyk, S. D., et al. 2014, ArXiv e-prints
Gerardy, C. L., Fesen, R. A., Nomoto, K., et al. 2002, PASJ, 54, 905
Griga, T., Marulla, A., Grenier, A., et al. 2011, Central Bureau Electronic Telegrams, 2736, 1
Helou, G., Kasliwal, M. M., Ofek, E. O., et al. 2013, ApJ, 778, L19
Hunter, D. J., Valenti, S., Kotak, R., et al. 2009, A&A, 508, 371
Iglesias, C. A. & Rogers, F. J. 1996, ApJ, 464, 943
Iwamoto, K., Young, T. R., Nakasato, N., et al. 1997, ApJ, 477, 865
Jerkstrand, A., Ergon, M., Smartt, S., et al. 2014, In preparation
Jerkstrand, A., Fransson, C., & Kozma, C. 2011, A&A, 530, A45
Jerkstrand, A., Fransson, C., Maguire, K., et al. 2012, A&A, 546, A28
Kozma, C. & Fransson, C. 1992, ApJ, 390, 602
Kozma, C. & Fransson, C. 1998a, ApJ, 496, 946
Kozma, C. & Fransson, C. 1998b, ApJ, 497, 431
Matheson, T., Filippenko, A. V., Ho, L. C., Barth, A. J., & Leonard, D. C. 2000, AJ, 120, 1499
Matthews, K., Neugebauer, G., Armus, L., & Soifer, B. T. 2002, AJ, 123, 753
Maund, J. R., Fraser, M., Ergon, M., et al. 2011, ApJ, 739, L37
Maund, J. R., Smartt, S. J., Kudritzki, R. P., Podsiadlowski, P., & Gilmore, G. F. 2004, Nature, 427, 129
Maurer, I., Mazzali, P. A., Taubenberger, S., & Hachinger, S. 2010, MNRAS, 409, 1441
Milisavljevic, D., Fesen, R. A., Gerardy, C. L., Kirshner, R. P., & Challis, P. 2010, ApJ, 709, 1343
Paxton, B., Bildsten, L., Dotter, A., et al. 2011, ApJS, 192, 3
Paxton, B., Cantiello, M., Arras, P., et al. 2013, ApJS, 208, 4
Podsiadlowski, P., Hsu, J. J. L., Joss, P. C., & Ross, R. R. 1993, Nature, 364, 509
Sahu, D. K., Anupama, G. C., & Chakradhari, N. K. 2013, MNRAS, 433, 2
Shigeyama, T., Suzuki, T., Kumagai, S., et al. 1994, ApJ, 420, 341
Shivvers, I., Mazzali, P., Silverman, J. M., et al. 2013, ArXiv e-prints
Spyromilio, J., Meikle, W. P. S., Learner, R. C. M., & Allen, D. A. 1988, Nature, 334, 327
Stancliffe, R. J. & Eldridge, J. J. 2009, MNRAS, 396, 1699
Stathakis, R. A., Dopita, M. A., Cannon, R. D., & Sadler, E. M. 1991, Supernovae, 649
Suntzeff, N. B. & Bouchet, P. 1990, AJ, 99, 650
Taubenberger, S., Navasardyan, H., Maurer, J. I., et al. 2011, MNRAS, 413, 2140
Taubenberger, S., Valenti, S., Benetti, S., et al. 2009, MNRAS, 397, 677
Tsvetkov, D. Y., Volkov, I. M., Baklanov, P., Blinnikov, S., & Tuchin, O. 2009, Peremennye Zvezdy, 29, 2
Tsvetkov, D. Y., Volkov, I. M., Sorokina, E., et al. 2012, Peremennye Zvezdy, 32, 6
Van Dyk, S. D., Li, W., Cenko, S. B., et al. 2011, ApJ, 741, L28
Van Dyk, S. D., Zheng, W., Clubb, K. I., et al. 2013, ApJ, 772, L32
Woosley, S. E. & Heger, A. 2007, Phys. Rep., 442, 269
Yaron, O. & Gal-Yam, A. 2012, PASP, 124, 668
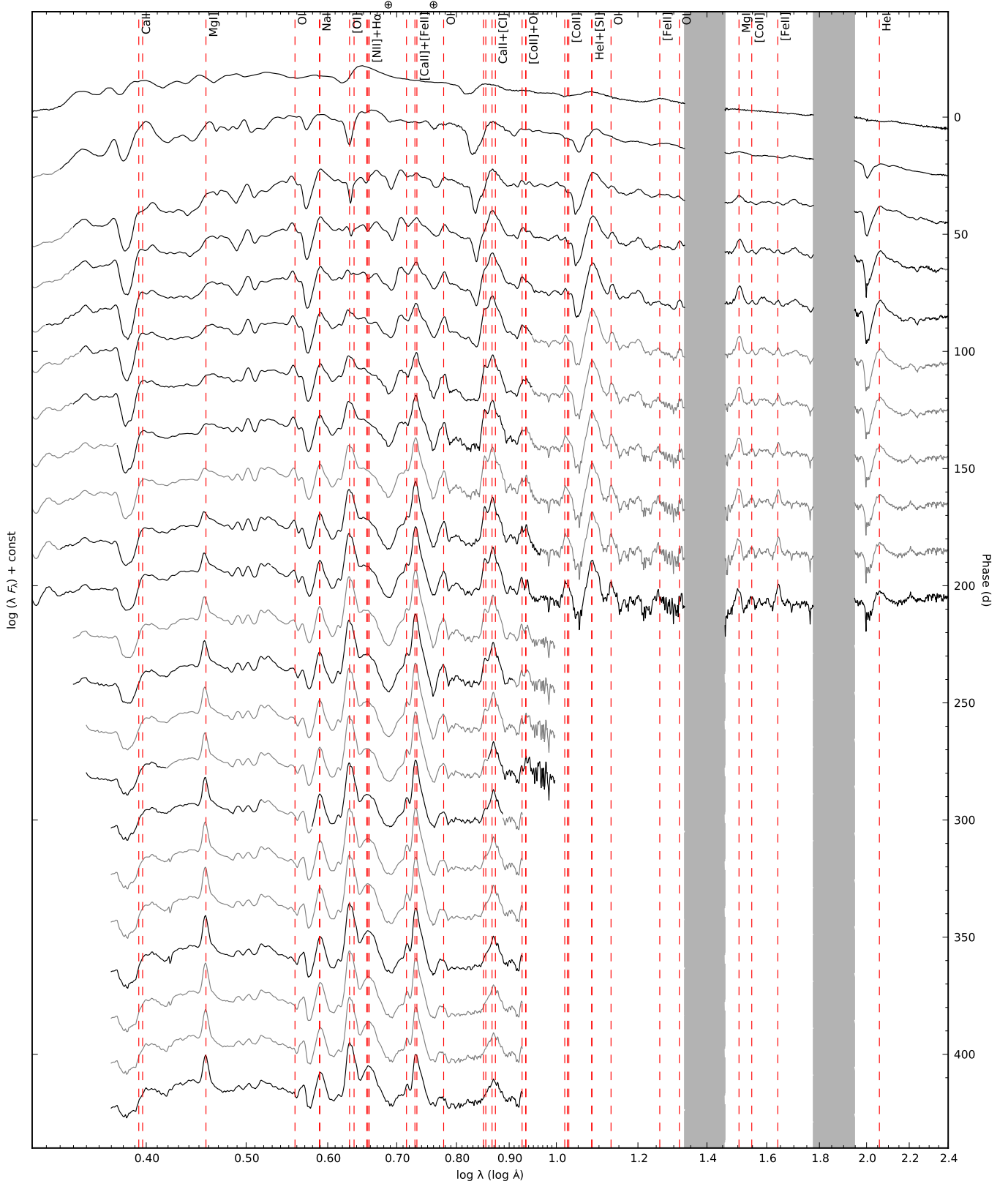
Fig. 7. Optical and NIR (interpolated) spectral evolution for SN 2011dh for days 5−425 with a 20-day sampling. Telluric absorption bands are marked with a ⊕ symbol in the optical and shown as grey regions in the NIR.
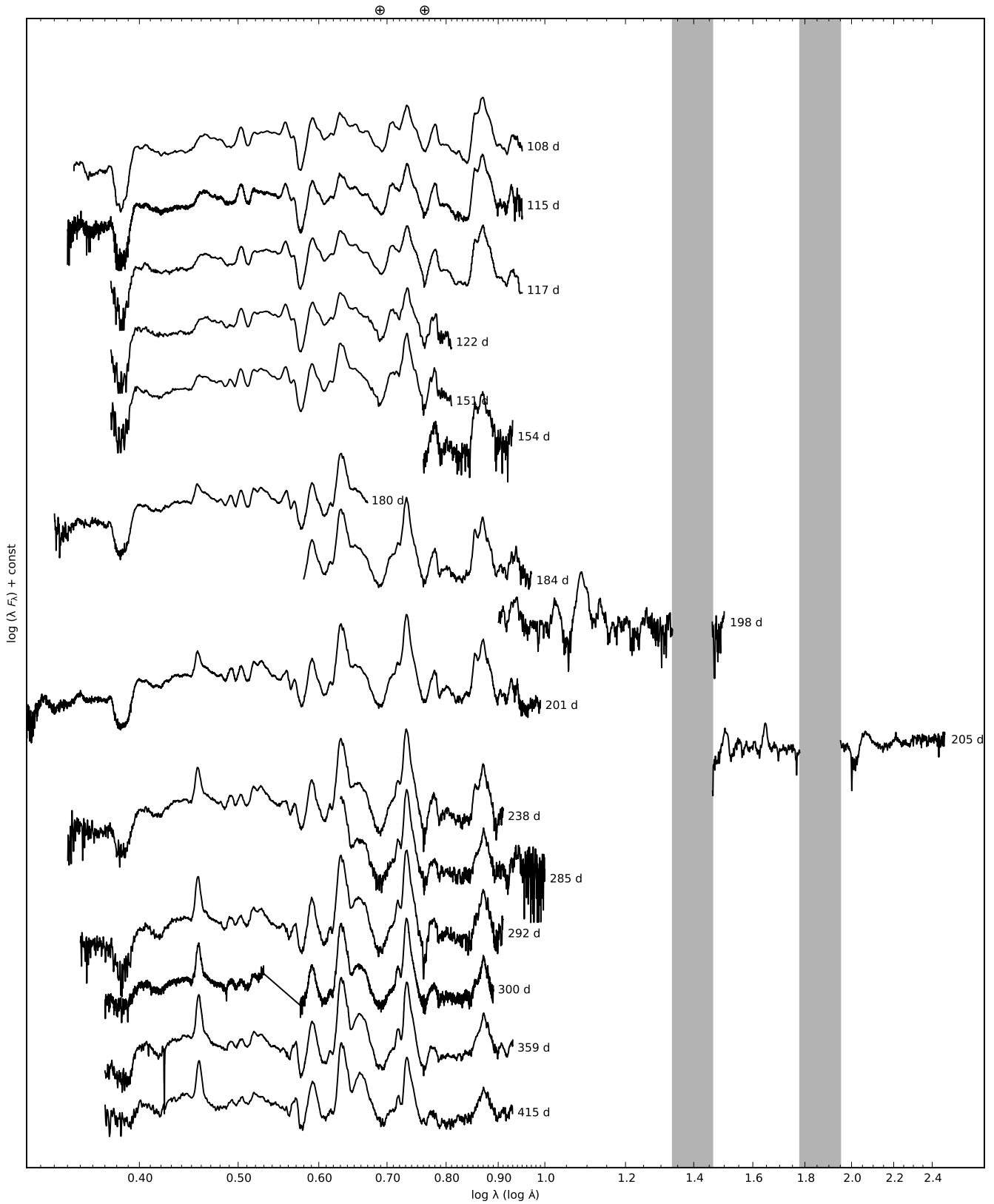
Fig. 8. Sequence of the observed late-time (100-415 days) spectra for SN 2011dh. Spectra obtained on the same night using the same telescope and instrument have been combined and each spectra have been labelled with the phase of the SN. Telluric absorption bands are marked with a ⊕ symbol in the optical and shown as grey regions in the NIR.
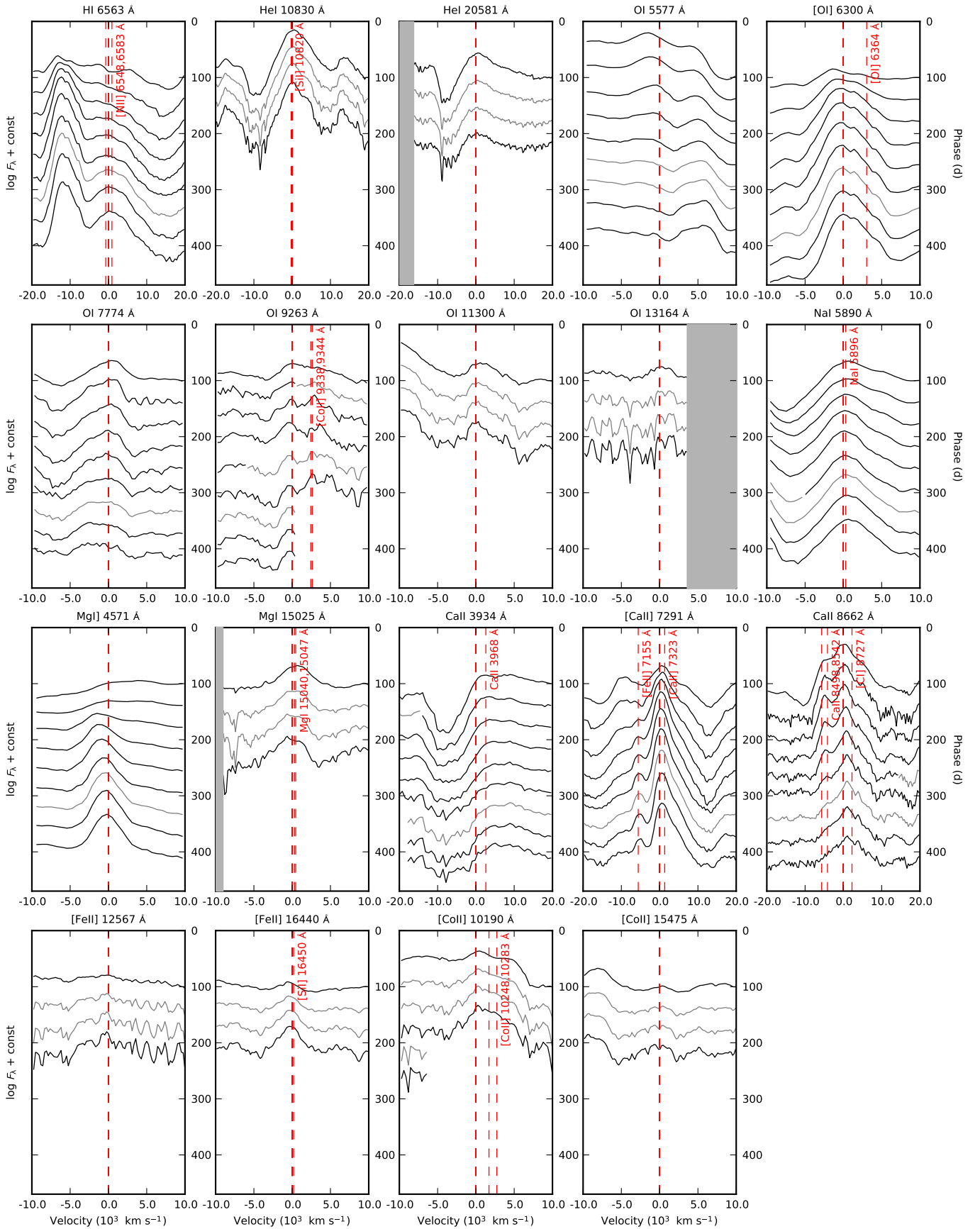
Fig. 9. Spectral evolution of all identified lines. Multiple or blended lines are marked with red dashed lines and telluric absorption bands in the NIR shown as grey regions.
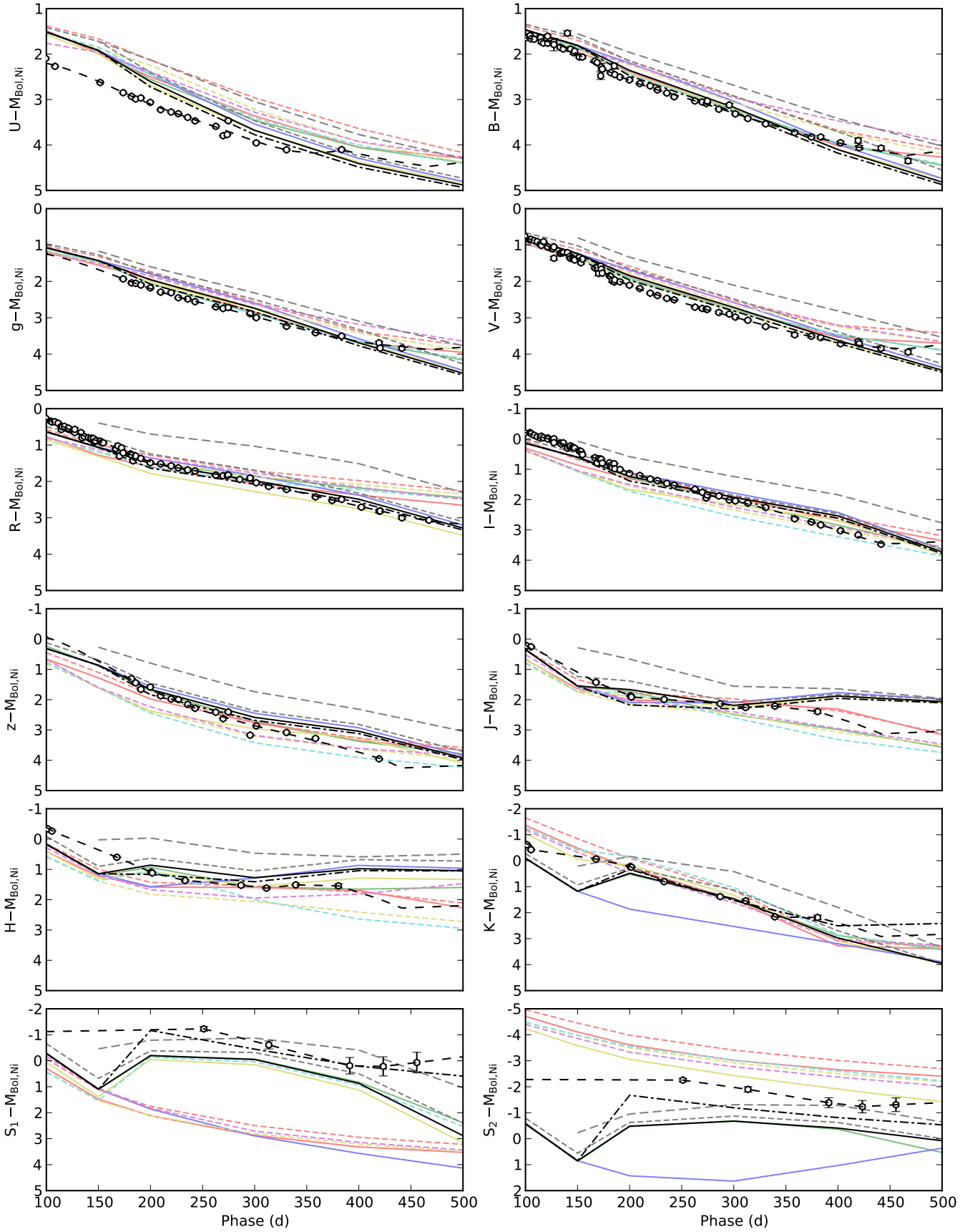
Fig. 20. 100-500 days observed (black circles) and J14 model optical, NIR and MIR magnitudes normalized to the radioactive decay chain luminosity of 0.075 $M_\odot$ of ^{56}Ni. The optimal model (12C) and the tweaked optimal model (12F) are shown in full colour and all other models in shaded colour. The models are displayed as follows; 12A (red solid line), 12B (green solid line), 12C (black solid line), 12D (yellow solid line), 12E (blue solid line), 12F (black dashed-dotted line), 13A (red short-dashed line), 13C (yellow short-dashed line), 13D (cyan short-dashed line), 13E (magenta short-dashed line), 13G (black short-dashed line), 17A (black long-dashed line).

Table 4. Optical colour-corrected JC *U* and S-corrected JC *BVRI* magnitudes for SN 2011dh. Errors are given in parentheses. For completeness data for the first 100 days already published in E14a are included.

JD (+2400000)	Phase	*U*	*B*	*V*	*R*	*I*	Telescope (Instrument)
(d)	(d)	(mag)	(mag)	(mag)	(mag)	(mag)	
55716.43	3.43	14.99 (0.03)	15.35 (0.02)	14.92 (0.02)	14.55 (0.01)	14.42 (0.02)	LT (RATCam)
55716.43	3.43	15.15 (0.08)	15.39 (0.02)	14.95 (0.02)	14.58 (0.01)	14.47 (0.01)	TNG (LRS)
55717.43	4.43	15.03 (0.03)	15.14 (0.02)	14.67 (0.03)	14.26 (0.01)	14.26 (0.03)	LT (RATCam)
55717.48	4.48	15.17 (0.09)	15.21 (0.03)	14.63 (0.03)	14.24 (0.01)	14.23 (0.02)	AS-1.82m (AFOSC)
55717.48	4.48	...	15.12 (0.03)	14.63 (0.02)	14.28 (0.01)	14.28 (0.02)	CANTAB (BIGST8)
55718.48	5.48	...	14.84 (0.01)	14.28 (0.02)	13.95 (0.01)	13.94 (0.01)	LT (RATCam)
55718.57	5.57	14.68 (0.06)	14.84 (0.02)	14.24 (0.02)	13.92 (0.01)	14.05 (0.01)	CA-2.2m (CAFOS)
55720.42	7.42	14.42 (0.02)	14.25 (0.01)	13.75 (0.03)	13.42 (0.01)	13.43 (0.02)	LT (RATCam)
55721.42	8.42	14.28 (0.10)	14.02 (0.01)	13.48 (0.01)	13.23 (0.01)	13.24 (0.02)	LT (RATCam)
55721.43	8.43	14.07 (0.07)	14.06 (0.01)	13.60 (0.04)	13.27 (0.02)	13.34 (0.02)	NOT (ALFOSC)
55722.42	9.42	...	13.86 (0.01)	13.29 (0.01)	13.06 (0.01)	13.07 (0.01)	LT (RATCam)
55723.41	10.41	13.98 (0.06)	13.71 (0.01)	13.16 (0.01)	12.89 (0.01)	12.89 (0.01)	LT (RATCam)
55724.41	11.41	13.91 (0.08)	13.61 (0.01)	13.03 (0.01)	12.80 (0.01)	12.77 (0.01)	LT (RATCam)
55725.39	12.39	...	...	12.94 (0.02)	12.67 (0.01)	...	MONTCAB (BIGST8)
55725.43	12.43	13.88 (0.07)	13.52 (0.02)	12.92 (0.04)	12.68 (0.01)	12.68 (0.01)	LT (RATCam)
55726.36	13.36	...	13.52 (0.01)	12.91 (0.02)	12.60 (0.01)	...	MONTCAB (BIGST8)
55728.40	15.40	...	13.39 (0.01)	12.78 (0.01)	12.45 (0.01)	...	MONTCAB (BIGST8)
55729.39	16.39	13.65 (0.01)	13.34 (0.01)	12.77 (0.06)	12.40 (0.01)	12.34 (0.02)	LT (RATCam)
55730.40	17.40	13.64 (0.03)	13.33 (0.01)	12.66 (0.01)	12.37 (0.01)	12.32 (0.01)	LT (RATCam)
55731.41	18.41	13.74 (0.09)	13.30 (0.01)	12.60 (0.02)	12.32 (0.01)	12.27 (0.01)	LT (RATCam)
55731.82	18.82	...	...	...	12.33 (0.02)	12.25 (0.01)	FTN (FS02)
55732.40	19.40	...	13.35 (0.03)	12.61 (0.01)	12.28 (0.01)	12.21 (0.01)	CANTAB (BIGST8)
55732.41	19.41	13.44 (0.06)	13.36 (0.02)	12.64 (0.02)	12.34 (0.02)	12.31 (0.02)	NOT (ALFOSC)
55732.46	19.46	13.71 (0.07)	13.31 (0.01)	12.58 (0.01)	12.29 (0.02)	12.22 (0.01)	LT (RATCam)
55733.45	20.45	13.67 (0.07)	...	...	12.27 (0.01)	12.20 (0.02)	LT (RATCam)
55734.52	21.52	13.37 (0.05)	13.33 (0.01)	12.58 (0.01)	12.26 (0.01)	12.29 (0.01)	CA-2.2m (CAFOS)
55735.44	22.44	13.91 (0.04)	...	...	12.27 (0.01)	12.15 (0.01)	LT (RATCam)
55736.44	23.44	14.13 (0.08)	...	...	12.27 (0.01)	12.16 (0.01)	LT (RATCam)
55737.39	24.39	...	13.65 (0.01)	12.73 (0.01)	...	...	LT (RATCam)
55738.42	25.42	14.50 (0.04)	13.78 (0.02)	12.81 (0.01)	12.33 (0.02)	12.22 (0.01)	LT (RATCam)
55738.51	25.51	14.20 (0.04)	13.77 (0.02)	12.83 (0.01)	12.39 (0.01)	12.26 (0.01)	NOT (ALFOSC)
55739.43	26.43	14.73 (0.04)	13.95 (0.02)	12.88 (0.01)	12.39 (0.01)	12.23 (0.01)	LT (RATCam)
55740.36	27.36	...	14.08 (0.04)	12.94 (0.01)	12.46 (0.01)	12.29 (0.01)	MONTCAB (BIGST8)
55740.43	27.43	14.91 (0.03)	14.11 (0.01)	12.98 (0.01)	12.49 (0.01)	12.29 (0.01)	LT (RATCam)
55740.44	27.44	...	...	12.97 (0.01)	12.48 (0.01)	...	TJO (MEIA)
55741.44	28.44	...	...	...	12.55 (0.01)	12.31 (0.01)	LT (RATCam)
55742.49	29.49	15.33 (0.01)	...	...	12.63 (0.01)	12.40 (0.01)	LT (RATCam)
55743.41	30.41	...	14.52 (0.01)	13.27 (0.02)	...	...	LT (RATCam)
55743.42	30.42	15.18 (0.05)	14.51 (0.02)	...	12.66 (0.01)	12.53 (0.01)	CA-2.2m (CAFOS)
55743.42	30.42	15.43 (0.05)	14.52 (0.01)	13.26 (0.03)	12.69 (0.01)	12.49 (0.01)	NOT (ALFOSC)
55745.39	32.39	15.74 (0.03)	14.73 (0.01)	13.44 (0.01)	12.79 (0.01)	12.56 (0.01)	NOT (ALFOSC)
55745.44	32.44	15.93 (0.04)	...	...	12.82 (0.01)	12.53 (0.01)	LT (RATCam)
55745.80	32.80	...	...	...	12.80 (0.01)	12.51 (0.01)	FTN (FS02)
55746.45	33.45	16.07 (0.04)	14.86 (0.03)	13.51 (0.01)	12.84 (0.01)	12.55 (0.02)	LT (RATCam)
55747.44	34.44	16.12 (0.04)	...	...	12.89 (0.01)	12.59 (0.01)	LT (RATCam)
55748.43	35.43	16.02 (0.02)	14.95 (0.01)	13.63 (0.01)	12.90 (0.01)	12.65 (0.01)	NOT (ALFOSC)
55748.44	35.44	16.27 (0.04)	...	...	12.95 (0.01)	12.62 (0.01)	LT (RATCam)
55750.40	37.40	16.20 (0.04)	15.09 (0.01)	13.74 (0.01)	13.04 (0.01)	12.73 (0.01)	NOT (ALFOSC)
55750.42	37.42	16.41 (0.14)	15.10 (0.02)	13.78 (0.03)	13.04 (0.01)	12.73 (0.02)	LT (RATCam)
55751.41	38.41	...	15.13 (0.01)	13.81 (0.01)	13.10 (0.01)	12.73 (0.01)	TJO (MEIA)
55751.43	38.43	...	...	...	13.12 (0.01)	12.76 (0.01)	LT (RATCam)
55752.45	39.45	16.54 (0.16)	...	...	13.14 (0.01)	12.74 (0.01)	LT (RATCam)

Table 4. Continued.

JD (+2400000) (d)	Phase (d)	U (mag)	B (mag)	V (mag)	R (mag)	I (mag)	Telescope (Instrument)
55753.42	40.42	...	15.28 (0.01)	13.91 (0.02)	...	...	LT (RATCam)
55753.46	40.46	16.45 (0.05)	15.23 (0.01)	13.86 (0.01)	13.17 (0.01)	12.81 (0.01)	NOT (ALFOSC)
55755.40	42.40	16.42 (0.04)	15.29 (0.01)	13.97 (0.01)	13.24 (0.01)	12.89 (0.01)	NOT (ALFOSC)
55756.44	43.44	...	15.26 (0.02)	13.99 (0.02)	13.30 (0.02)	12.86 (0.01)	AS-Schmidt (SBIG)
55756.45	43.45	...	15.37 (0.02)	13.98 (0.01)	13.28 (0.03)	12.92 (0.01)	LT (RATCam)
55757.43	44.43	16.42 (0.04)	15.37 (0.01)	14.05 (0.01)	13.30 (0.01)	12.97 (0.01)	NOT (ALFOSC)
55759.45	46.45	...	15.43 (0.01)	14.07 (0.02)	...	...	LT (RATCam)
55761.40	48.40	...	15.42 (0.01)	14.18 (0.01)	13.46 (0.01)	13.03 (0.01)	AS-Schmidt (SBIG)
55762.41	49.41	...	15.44 (0.01)	14.17 (0.01)	13.46 (0.01)	13.06 (0.01)	NOT (ALFOSC)
55762.78	49.78	...	...	...	13.44 (0.01)	13.03 (0.01)	FTN (FS02)
55763.44	50.44	...	15.45 (0.01)	14.22 (0.01)	13.49 (0.01)	13.10 (0.01)	AS-Schmidt (SBIG)
55765.43	52.43	16.44 (0.03)	15.51 (0.01)	14.26 (0.01)	13.57 (0.01)	13.17 (0.01)	NOT (ALFOSC)
55767.43	54.43	16.50 (0.05)	...	...	13.59 (0.01)	13.17 (0.02)	LT (RATCam)
55768.45	55.45	16.48 (0.04)	...	...	13.60 (0.02)	13.19 (0.02)	LT (RATCam)
55771.40	58.40	16.37 (0.03)	15.58 (0.01)	14.33 (0.01)	13.64 (0.01)	13.29 (0.01)	CA-2.2m (CAFOS)
55773.39	60.39	16.45 (0.04)	15.59 (0.01)	14.39 (0.01)	13.72 (0.01)	13.32 (0.01)	NOT (ALFOSC)
55776.38	63.38	16.47 (0.04)	15.63 (0.01)	14.46 (0.01)	13.79 (0.01)	13.36 (0.01)	NOT (ALFOSC)
55777.33	64.33	...	15.50 (0.03)	14.46 (0.02)	13.79 (0.02)	13.35 (0.02)	AS-Schmidt (SBIG)
55780.40	67.40	16.42 (0.03)	15.65 (0.01)	14.51 (0.01)	13.86 (0.01)	13.43 (0.01)	NOT (ALFOSC)
55782.38	69.38	16.31 (0.07)	...	...	13.89 (0.01)	13.47 (0.01)	LT (RATCam)
55783.43	70.43	16.41 (0.03)	15.70 (0.01)	14.58 (0.01)	13.95 (0.01)	13.51 (0.01)	NOT (ALFOSC)
55784.33	71.33	...	15.65 (0.02)	14.59 (0.01)	...	13.43 (0.02)	AS-Schmidt (SBIG)
55784.39	71.39	16.45 (0.04)	15.66 (0.01)	14.52 (0.02)	13.91 (0.01)	13.48 (0.02)	CA-2.2m (CAFOS)
55784.77	71.77	...	...	...	13.93 (0.02)	13.45 (0.01)	FTN (FS02)
55785.36	72.36	...	15.69 (0.02)	14.62 (0.01)	13.97 (0.01)	13.46 (0.01)	AS-Schmidt (SBIG)
55788.41	75.41	...	...	...	14.03 (0.02)	13.52 (0.01)	AS-Schmidt (SBIG)
55790.38	77.38	16.45 (0.09)	...	...	14.04 (0.01)	13.61 (0.01)	LT (RATCam)
55793.37	80.37	16.55 (0.07)	15.79 (0.01)	14.75 (0.01)	14.14 (0.01)	13.68 (0.01)	NOT (ALFOSC)
55795.35	82.35	16.40 (0.04)	15.78 (0.01)	14.76 (0.01)	14.14 (0.01)	13.69 (0.01)	CA-2.2m (CAFOS)
55797.37	84.37	...	15.81 (0.02)	14.82 (0.01)	...	...	AS-Schmidt (SBIG)
55797.76	84.76	...	...	...	14.22 (0.01)	13.68 (0.01)	FTN (FS02)
55798.36	85.36	16.50 (0.03)	15.83 (0.01)	14.84 (0.01)	14.26 (0.01)	13.65 (0.02)	NOT (ALFOSC)
55799.33	86.33	...	15.81 (0.01)	14.87 (0.01)	...	...	AS-Schmidt (SBIG)
55801.36	88.36	16.44 (0.04)	15.88 (0.01)	14.90 (0.01)	14.32 (0.01)	13.81 (0.01)	NOT (ALFOSC)
55801.40	88.40	...	15.79 (0.02)	14.90 (0.01)	...	...	AS-Schmidt (SBIG)
55803.35	90.35	...	15.86 (0.02)	14.91 (0.01)	14.34 (0.01)	13.80 (0.01)	AS-Schmidt (SBIG)
55805.33	92.33	...	15.85 (0.02)	14.97 (0.02)	14.38 (0.01)	13.84 (0.01)	AS-Schmidt (SBIG)
55810.34	97.34	16.68 (0.06)	15.99 (0.01)	15.11 (0.01)	14.53 (0.01)	14.03 (0.01)	NOT (ALFOSC)
55812.33	99.33	16.51 (0.03)	16.01 (0.01)	15.06 (0.01)	14.51 (0.01)	14.01 (0.01)	CA-2.2m (CAFOS)
55817.35	104.35	...	16.00 (0.03)	15.20 (0.02)	14.64 (0.02)	14.04 (0.02)	AS-Schmidt (SBIG)
55818.33	105.33	...	16.08 (0.02)	15.19 (0.02)	14.68 (0.01)	14.09 (0.01)	AS-Schmidt (SBIG)
55821.31	108.31	16.77 (0.08)	16.12 (0.02)	15.26 (0.01)	14.70 (0.01)	14.17 (0.01)	CA-2.2m (CAFOS)
55824.32	111.32	...	...	15.31 (0.02)	14.77 (0.03)	14.25 (0.03)	AS-Schmidt (SBIG)
55827.33	114.33	...	16.14 (0.03)	15.42 (0.01)	14.88 (0.02)	14.28 (0.01)	AS-Schmidt (SBIG)
55827.48	114.48	...	16.15 (0.06)	15.41 (0.03)	14.97 (0.05)	14.32 (0.05)	AT (ANDOR)
55828.27	115.27	...	16.25 (0.03)	15.46 (0.02)	14.91 (0.01)	14.27 (0.01)	AT (ANDOR)
55830.28	117.28	...	16.30 (0.02)	15.38 (0.01)	14.91 (0.01)	14.34 (0.01)	AS-1.82m (AFOSC)
55834.26	121.26	...	16.18 (0.03)	15.55 (0.03)	15.03 (0.01)	14.38 (0.02)	AT (ANDOR)
55834.31	121.31	...	16.34 (0.02)	15.56 (0.01)	15.00 (0.02)	14.42 (0.02)	AS-Schmidt (SBIG)
55838.34	125.34	...	...	15.64 (0.02)	15.12 (0.03)	14.49 (0.01)	AS-Schmidt (SBIG)
55839.28	126.28	...	16.37 (0.03)	15.65 (0.02)	15.13 (0.02)	14.52 (0.02)	AS-Schmidt (SBIG)
55840.26	127.26	...	16.37 (0.03)	15.62 (0.02)	15.18 (0.02)	14.47 (0.02)	AT (ANDOR)
55840.30	127.30	...	16.42 (0.14)	15.93 (0.06)	15.09 (0.04)	14.60 (0.04)	AS-Schmidt (SBIG)

Table 4. Continued.

JD (+2400000)	Phase	U	B	V	R	I	Telescope (Instrument)
(d)	(d)	(mag)	(mag)	(mag)	(mag)	(mag)	
55846.26	133.26	...	16.54 (0.03)	15.85 (0.03)	15.24 (0.02)	14.66 (0.02)	AT (ANDOR)
55847.30	134.30	...	...	15.85 (0.03)	15.39 (0.02)	14.71 (0.02)	AT (ANDOR)
55849.26	136.26	...	16.61 (0.04)	15.86 (0.03)	15.38 (0.02)	14.69 (0.02)	AT (ANDOR)
55853.27	140.27	...	16.30 (0.06)	15.90 (0.05)	15.45 (0.05)	14.91 (0.04)	AS-Schmidt (SBIG)
55855.38	142.38	...	...	16.02 (0.03)	15.50 (0.03)	14.89 (0.03)	AT (ANDOR)
55856.24	143.24	...	16.68 (0.05)	16.08 (0.03)	15.49 (0.02)	14.86 (0.02)	AT (ANDOR)
55858.29	145.29	...	...	16.10 (0.03)	15.52 (0.02)	14.92 (0.03)	AT (ANDOR)
55859.23	146.23	...	16.79 (0.04)	16.14 (0.03)	15.62 (0.03)	14.96 (0.03)	AT (ANDOR)
55860.22	147.22	...	16.76 (0.04)	16.17 (0.04)	15.60 (0.02)	14.97 (0.02)	AT (ANDOR)
55864.69	151.69	17.55 (0.09)	16.94 (0.02)	16.14 (0.01)	15.65 (0.01)	15.10 (0.01)	AS-1.82m (AFOSC)
55866.28	153.28	...	...	16.30 (0.03)	15.71 (0.02)	15.14 (0.02)	AT (ANDOR)
55867.70	154.70	...	16.97 (0.02)	16.22 (0.03)	15.73 (0.02)	15.26 (0.02)	CA-2.2m (CAFOS)
55879.66	166.66	...	17.17 (0.03)	16.58 (0.02)	16.00 (0.02)	15.48 (0.02)	AS-Schmidt (SBIG)
55881.74	168.74	...	17.23 (0.02)	16.59 (0.02)	15.95 (0.01)	15.67 (0.03)	CA-2.2m (CAFOS)
55883.24	170.24	...	...	16.76 (0.06)	16.24 (0.04)	15.55 (0.03)	AT (ANDOR)
55885.21	172.21	...	17.55 (0.08)	16.58 (0.04)	16.04 (0.04)	15.58 (0.03)	AT (ANDOR)
55885.73	172.73	...	17.36 (0.08)	16.67 (0.02)	...	15.59 (0.03)	AS-1.82m (AFOSC)
55886.75	173.75	17.99 (0.03)	17.42 (0.01)	16.79 (0.01)	16.19 (0.01)	15.72 (0.01)	NOT (ALFOSC)
55893.71	180.71	...	...	16.93 (0.02)	16.29 (0.01)	15.78 (0.02)	AS-Schmidt (SBIG)
55894.76	181.76	18.15 (0.02)	17.57 (0.01)	16.96 (0.01)	16.33 (0.01)	15.88 (0.01)	NOT (ALFOSC)
55896.20	183.20	...	...	17.08 (0.06)	16.50 (0.05)	15.97 (0.04)	AT (ANDOR)
55898.19	185.19	...	17.46 (0.06)	17.14 (0.05)	16.43 (0.04)	15.86 (0.03)	AT (ANDOR)
55898.73	185.73	18.24 (0.05)	17.65 (0.01)	17.09 (0.01)	16.39 (0.01)	16.03 (0.01)	NOT (ALFOSC)
55903.76	190.76	18.27 (0.04)	17.76 (0.02)	17.19 (0.02)	16.51 (0.02)	16.10 (0.02)	NOT (ALFOSC)
55912.79	199.79	18.46 (0.04)	17.91 (0.02)	17.37 (0.02)	16.72 (0.01)	16.32 (0.01)	NOT (ALFOSC)
55917.79	204.79	18.54 (0.04)	17.99 (0.01)	17.48 (0.01)	16.75 (0.01)	16.39 (0.01)	NOT (ALFOSC)
55922.76	209.76	18.71 (0.04)	18.09 (0.01)	17.56 (0.01)	16.84 (0.01)	16.48 (0.01)	NOT (ALFOSC)
55932.79	219.79	18.86 (0.06)	18.23 (0.01)	17.79 (0.02)	17.00 (0.02)	16.70 (0.02)	NOT (ALFOSC)
55939.73	226.73	18.97 (0.05)	18.39 (0.01)	17.92 (0.02)	17.12 (0.01)	16.82 (0.01)	NOT (ALFOSC)
55948.73	235.73	19.14 (0.04)	18.55 (0.01)	18.09 (0.02)	17.26 (0.01)	17.00 (0.01)	NOT (ALFOSC)
55955.76	242.76	19.28 (0.04)	18.70 (0.01)	18.19 (0.01)	17.36 (0.01)	17.13 (0.01)	NOT (ALFOSC)
55975.69	262.69	19.60 (0.05)	18.98 (0.01)	18.59 (0.01)	17.67 (0.01)	17.45 (0.01)	NOT (ALFOSC)
55982.74	269.74	19.87 (0.07)	19.08 (0.02)	18.69 (0.02)	17.75 (0.01)	17.62 (0.01)	NOT (ALFOSC)
55986.62	273.62	19.88 (0.11)	19.15 (0.03)	18.75 (0.03)	17.78 (0.02)	17.85 (0.03)	CA-2.2m (CAFOS)
55987.62	274.62	19.59 (0.12)	19.10 (0.02)	18.77 (0.02)	17.78 (0.01)	17.76 (0.01)	LT (RATCam)
55998.66	285.66	...	19.34 (0.04)	18.97 (0.04)	18.00 (0.02)	17.88 (0.02)	LT (RATCam)
55998.67	285.67	...	19.39 (0.02)	18.96 (0.02)	18.01 (0.01)	17.90 (0.01)	NOT (ALFOSC)
56008.66	295.66	...	19.39 (0.03)	19.10 (0.03)	18.07 (0.02)	18.13 (0.03)	LT (RATCam)
56014.51	301.51	20.34 (0.07)	19.64 (0.01)	19.24 (0.02)	18.27 (0.01)	18.19 (0.01)	NOT (ALFOSC)
56026.49	313.49	...	19.85 (0.02)	19.45 (0.02)	18.49 (0.01)	18.38 (0.02)	NOT (ALFOSC)
56043.59	330.59	20.77 (0.05)	20.14 (0.02)	19.78 (0.02)	18.74 (0.01)	18.70 (0.02)	NOT (ALFOSC)
56071.42	358.42	...	20.60 (0.02)	20.28 (0.04)	19.21 (0.02)	19.34 (0.03)	NOT (ALFOSC)
56087.43	374.43	...	20.85 (0.02)	20.48 (0.03)	19.46 (0.02)	19.60 (0.02)	NOT (ALFOSC)
56096.48	383.48	21.28 (0.08)	20.94 (0.03)	20.61 (0.04)	19.52 (0.02)	19.79 (0.03)	NOT (ALFOSC)
56115.44	402.44	...	21.25 (0.03)	20.96 (0.05)	19.92 (0.02)	20.17 (0.04)	NOT (ALFOSC)
56132.43	419.43	...	21.37 (0.06)	21.07 (0.06)	20.19 (0.03)	20.47 (0.05)	NOT (ALFOSC)
56133.40	420.40	...	21.54 (0.05)	21.13 (0.06)	20.20 (0.03)	...	NOT (ALFOSC)
56154.39	441.39	...	21.75 (0.05)	21.46 (0.06)	20.59 (0.04)	20.99 (0.08)	NOT (ALFOSC)
56180.37	467.37	...	22.29 (0.05)	21.82 (0.06)	20.91 (0.04)	...	NOT (ALFOSC)
56313.73	600.73	...	...	22.44 (0.10)	...	...	NOT (ALFOSC)
56353.50	640.50	...	...	23.02 (0.00)	...	22.58 (0.00)	HST (ACS)
56371.69	658.69	...	23.42 (0.32)	...	...	...	NOT (ALFOSC)
56397.64	684.64	...	...	23.20 (0.20)	...	...	NOT (ALFOSC)
56445.43	732.43	...	23.96 (0.50)	...	...	...	NOT (ALFOSC)

Table 5. Optical colour-corrected SDSS *u* and S-corrected SDSS *griz* magnitudes for SN 2011dh. Errors are given in parentheses. For completeness data for the first 100 days already published in E14a are included.

JD (+2400000)	Phase	u	g	r	i	z	Telescope (Instrument)
(d)	(d)	(mag)	(mag)	(mag)	(mag)	(mag)	
55716.47	3.47	15.86 (0.04)	15.08 (0.01)	14.69 (0.01)	14.80 (0.01)	14.76 (0.02)	LT (RATCam)
55717.46	4.46	15.99 (0.03)	14.80 (0.01)	14.39 (0.01)	14.61 (0.01)	14.58 (0.02)	LT (RATCam)
55718.53	5.53	...	14.44 (0.04)	14.06 (0.01)	14.27 (0.01)	...	LT (RATCam)
55720.44	7.44	15.39 (0.02)	13.97 (0.01)	13.53 (0.01)	13.72 (0.02)	13.87 (0.01)	LT (RATCam)
55721.44	8.44	15.08 (0.02)	13.78 (0.01)	13.34 (0.01)	13.51 (0.01)	13.64 (0.01)	LT (RATCam)
55722.44	9.44	...	13.59 (0.01)	13.18 (0.01)	13.34 (0.01)	13.49 (0.01)	LT (RATCam)
55723.41	10.41	14.80 (0.03)	...	13.03 (0.01)	13.16 (0.01)	13.34 (0.01)	LT (RATCam)
55724.41	11.41	14.70 (0.02)	...	12.93 (0.01)	13.05 (0.01)	13.22 (0.01)	LT (RATCam)
55725.43	12.43	14.72 (0.04)	...	12.83 (0.01)	12.93 (0.01)	13.10 (0.01)	LT (RATCam)
55729.39	16.39	14.56 (0.03)	13.10 (0.01)	12.56 (0.01)	12.61 (0.01)	12.81 (0.01)	LT (RATCam)
55730.40	17.40	14.45 (0.03)	13.07 (0.01)	12.51 (0.01)	12.56 (0.01)	12.78 (0.01)	LT (RATCam)
55731.41	18.41	14.54 (0.04)	13.02 (0.01)	12.46 (0.01)	12.50 (0.01)	12.72 (0.01)	LT (RATCam)
55731.82	18.82	...	13.07 (0.01)	12.46 (0.01)	12.50 (0.01)	12.65 (0.01)	FTN (FS02)
55732.46	19.46	14.57 (0.02)	12.99 (0.03)	12.43 (0.01)	12.47 (0.01)	12.68 (0.01)	LT (RATCam)
55733.45	20.45	14.53 (0.05)	13.02 (0.01)	12.42 (0.01)	12.44 (0.01)	12.65 (0.01)	LT (RATCam)
55735.44	22.44	14.77 (0.04)	13.12 (0.01)	12.43 (0.01)	12.41 (0.01)	12.60 (0.01)	LT (RATCam)
55736.44	23.44	14.99 (0.03)	13.19 (0.02)	12.46 (0.01)	12.41 (0.01)	12.59 (0.02)	LT (RATCam)
55738.45	25.45	15.42 (0.03)	13.43 (0.01)	12.56 (0.01)	12.46 (0.01)	12.66 (0.01)	LT (RATCam)
55739.44	26.44	15.60 (0.03)	13.50 (0.03)	12.60 (0.01)	12.50 (0.01)	12.65 (0.01)	LT (RATCam)
55740.44	27.44	15.86 (0.03)	13.65 (0.01)	12.67 (0.01)	12.54 (0.01)	12.70 (0.01)	LT (RATCam)
55741.44	28.44	...	13.75 (0.02)	12.77 (0.01)	12.58 (0.02)	12.76 (0.01)	LT (RATCam)
55742.49	29.49	16.28 (0.04)	13.92 (0.01)	12.84 (0.01)	12.65 (0.01)	12.81 (0.01)	LT (RATCam)
55745.44	32.44	16.80 (0.06)	14.20 (0.02)	13.04 (0.01)	12.78 (0.01)	12.87 (0.03)	LT (RATCam)
55745.80	32.80	...	14.35 (0.04)	13.00 (0.01)	12.79 (0.01)	12.94 (0.01)	FTN (FS02)
55746.45	33.45	16.92 (0.05)	14.31 (0.01)	13.10 (0.01)	12.81 (0.01)	12.94 (0.01)	LT (RATCam)
55747.44	34.44	16.99 (0.05)	14.40 (0.02)	13.14 (0.01)	12.85 (0.01)	12.96 (0.01)	LT (RATCam)
55748.44	35.44	17.18 (0.06)	14.42 (0.02)	13.20 (0.01)	12.90 (0.01)	13.01 (0.01)	LT (RATCam)
55750.44	37.44	17.29 (0.11)	14.55 (0.02)	13.30 (0.01)	13.01 (0.02)	13.05 (0.04)	LT (RATCam)
55751.43	38.43	17.23 (0.04)	14.64 (0.03)	13.36 (0.01)	13.03 (0.01)	13.12 (0.01)	LT (RATCam)
55752.45	39.45	17.34 (0.08)	14.65 (0.01)	13.40 (0.01)	13.03 (0.01)	13.10 (0.01)	LT (RATCam)
55756.46	43.46	...	14.79 (0.01)	13.56 (0.01)	13.22 (0.01)	13.19 (0.01)	LT (RATCam)
55762.78	49.78	...	15.00 (0.02)	13.68 (0.01)	13.37 (0.01)	13.28 (0.01)	FTN (FS02)
55767.43	54.43	17.36 (0.03)	15.02 (0.01)	13.84 (0.01)	13.52 (0.01)	13.38 (0.02)	LT (RATCam)
55768.45	55.45	17.34 (0.03)	15.02 (0.01)	13.87 (0.01)	13.56 (0.01)	13.41 (0.01)	LT (RATCam)
55773.39	60.39	17.19 (0.04)	15.06 (0.01)	14.00 (0.01)	13.72 (0.01)	13.53 (0.02)	NOT (ALFOSC)
55776.38	63.38	17.27 (0.03)	15.12 (0.01)	14.04 (0.01)	13.76 (0.01)	13.55 (0.01)	NOT (ALFOSC)
55780.41	67.41	17.25 (0.03)	15.16 (0.01)	14.10 (0.01)	13.84 (0.01)	13.60 (0.01)	NOT (ALFOSC)
55782.38	69.38	17.17 (0.04)	15.19 (0.01)	14.15 (0.01)	13.86 (0.01)	13.62 (0.01)	LT (RATCam)
55783.44	70.44	17.19 (0.04)	15.18 (0.01)	14.20 (0.01)	13.94 (0.01)	13.66 (0.01)	NOT (ALFOSC)
55784.77	71.77	...	15.23 (0.02)	14.16 (0.01)	13.88 (0.01)	13.64 (0.01)	FTN (FS02)
55790.38	77.38	17.31 (0.03)	15.34 (0.04)	14.29 (0.01)	14.04 (0.01)	13.69 (0.02)	LT (RATCam)
55793.37	80.37	17.26 (0.03)	15.30 (0.01)	14.40 (0.01)	14.16 (0.01)	13.83 (0.01)	NOT (ALFOSC)
55797.76	84.76	...	15.38 (0.01)	14.42 (0.01)	14.18 (0.01)	13.82 (0.01)	FTN (FS02)
55798.37	85.37	17.28 (0.03)	15.37 (0.01)	14.51 (0.01)	14.26 (0.01)	13.86 (0.01)	NOT (ALFOSC)
55801.36	88.36	17.26 (0.02)	15.41 (0.01)	14.54 (0.01)	14.31 (0.01)	13.88 (0.01)	NOT (ALFOSC)
55810.34	97.34	17.41 (0.02)	15.55 (0.01)	14.76 (0.01)	14.56 (0.01)	14.09 (0.02)	NOT (ALFOSC)
55886.75	173.75	18.76 (0.04)	16.99 (0.01)	16.37 (0.01)	16.14 (0.01)	...	NOT (ALFOSC)
55894.76	181.76	18.92 (0.03)	17.18 (0.02)	16.51 (0.01)	16.27 (0.01)	16.29 (0.02)	NOT (ALFOSC)
55898.73	185.73	19.02 (0.04)	17.23 (0.01)	16.58 (0.01)	16.39 (0.01)	16.47 (0.02)	NOT (ALFOSC)
55903.76	190.76	19.13 (0.08)	17.33 (0.02)	16.70 (0.01)	16.45 (0.01)	16.73 (0.04)	NOT (ALFOSC)
55912.79	199.79	19.29 (0.06)	17.49 (0.02)	16.90 (0.01)	16.64 (0.01)	16.74 (0.04)	NOT (ALFOSC)

Table 5. Continued.

JD (+2400000)	Phase	u	g	r	i	z	Telescope (Instrument)
(d)	(d)	(mag)	(mag)	(mag)	(mag)	(mag)	
55922.77	209.77	19.47 (0.02)	17.71 (0.01)	17.03 (0.01)	16.79 (0.01)	17.13 (0.01)	NOT (ALFOSC)
55932.79	219.79	19.62 (0.05)	17.82 (0.02)	17.20 (0.02)	16.96 (0.02)	17.33 (0.04)	NOT (ALFOSC)
55939.74	226.74	19.76 (0.05)	18.03 (0.01)	17.31 (0.01)	17.07 (0.01)	17.42 (0.02)	NOT (ALFOSC)
55948.73	235.73	19.93 (0.03)	18.15 (0.01)	17.45 (0.01)	17.22 (0.01)	17.67 (0.01)	NOT (ALFOSC)
55955.76	242.76	20.08 (0.03)	18.29 (0.01)	17.56 (0.01)	17.34 (0.01)	17.86 (0.02)	NOT (ALFOSC)
55975.69	262.69	20.32 (0.04)	18.63 (0.01)	17.84 (0.01)	17.65 (0.01)	18.19 (0.02)	NOT (ALFOSC)
55982.74	269.74	20.68 (0.06)	18.74 (0.01)	17.94 (0.01)	17.83 (0.01)	18.47 (0.03)	NOT (ALFOSC)
55987.62	274.62	20.49 (0.11)	18.76 (0.01)	17.95 (0.01)	17.94 (0.01)	18.29 (0.03)	LT (RATCam)
55998.66	285.66	...	19.02 (0.03)	18.15 (0.02)	18.06 (0.02)	18.74 (0.06)	LT (RATCam)
56008.66	295.66	...	19.13 (0.02)	18.22 (0.01)	18.31 (0.03)	19.26 (0.10)	LT (RATCam)
56014.52	301.52	21.08 (0.05)	19.30 (0.01)	18.40 (0.01)	18.45 (0.01)	19.02 (0.02)	NOT (ALFOSC)
56043.60	330.60	21.53 (0.04)	19.82 (0.01)	18.82 (0.01)	18.96 (0.01)	19.52 (0.03)	NOT (ALFOSC)
56071.43	358.43	...	20.27 (0.02)	19.26 (0.02)	19.62 (0.03)	19.98 (0.05)	NOT (ALFOSC)
56096.49	383.49	22.07 (0.07)	20.61 (0.02)	19.55 (0.02)	20.09 (0.03)	...	NOT (ALFOSC)
56132.43	419.43	...	21.14 (0.03)	20.21 (0.03)	20.79 (0.05)	21.25 (0.17)	NOT (ALFOSC)
56133.41	420.41	...	21.30 (0.04)	20.21 (0.03)	20.95 (0.06)	...	NOT (ALFOSC)
56154.39	441.39	...	21.50 (0.04)	20.61 (0.03)	21.32 (0.07)	...	NOT (ALFOSC)
56313.75	600.75	...	...	22.46 (0.11)	...	...	NOT (ALFOSC)
56428.46	715.46	...	...	23.10 (0.20)	...	...	NOT (ALFOSC)

Table 6. NIR S-corrected 2MASS *JHK* magnitudes for SN 2011dh. Errors are given in parentheses. For completeness data for the first 100 days already published in E14a are included.

JD (+2400000)	Phase	*J*	*H*	*K*	Telescope (Instrument)
(d)	(d)	(mag)	(mag)	(mag)	
55716.51	3.51	14.09 (0.01)	13.90 (0.01)	13.68 (0.02)	TNG (NICS)
55722.40	9.40	12.89 (0.01)	12.87 (0.01)	12.67 (0.01)	TNG (NICS)
55725.50	12.50	12.61 (0.04)	12.54 (0.01)	12.43 (0.02)	NOT (NOTCAM)
55730.51	17.51	12.12 (0.01)	12.08 (0.01)	11.94 (0.01)	TNG (NICS)
55737.72	24.72	11.96 (0.01)	11.90 (0.01)	11.72 (0.03)	LBT (LUCIFER)
55741.13	28.13	11.94 (0.01)	11.90 (0.02)	11.70 (0.05)	TCS (CAIN)
55748.43	35.43	12.14 (0.01)	12.00 (0.02)	11.77 (0.01)	TCS (CAIN)
55750.42	37.42	12.19 (0.01)	12.00 (0.01)	11.84 (0.04)	TCS (CAIN)
55751.42	38.42	12.29 (0.01)	12.01 (0.01)	11.84 (0.03)	TCS (CAIN)
55758.45	45.45	12.55 (0.01)	12.22 (0.01)	12.06 (0.01)	TNG (NICS)
55759.41	46.41	12.49 (0.03)	12.22 (0.03)	12.11 (0.04)	TCS (CAIN)
55762.41	49.41	12.57 (0.01)	12.26 (0.01)	12.17 (0.03)	TCS (CAIN)
55763.42	50.42	12.62 (0.02)	12.27 (0.04)	12.25 (0.06)	TCS (CAIN)
55765.45	52.45	12.79 (0.01)	12.38 (0.01)	12.23 (0.01)	TNG (NICS)
55769.41	56.41	12.77 (0.01)	12.48 (0.06)	12.40 (0.03)	TCS (CAIN)
55773.37	60.37	12.94 (0.03)	12.58 (0.01)	12.42 (0.02)	TNG (NICS)
55774.40	61.40	12.90 (0.01)	12.55 (0.03)	12.43 (0.04)	TCS (CAIN)
55776.40	63.40	13.00 (0.01)	12.64 (0.01)	12.53 (0.02)	TCS (CAIN)
55781.41	68.41	13.23 (0.01)	12.76 (0.01)	12.66 (0.01)	WHT (LIRIS)
55787.44	74.44	13.56 (0.03)	13.03 (0.02)	12.95 (0.02)	NOT (NOTCAM)
55801.36	88.36	13.90 (0.02)	13.41 (0.02)	13.17 (0.01)	TNG (NICS)
55804.34	91.34	14.10 (0.01)	13.50 (0.01)	13.26 (0.01)	CA-3.5m (O2000)
55814.32	101.32	14.38 (0.01)	13.80 (0.01)	13.50 (0.01)	CA-3.5m (O2000)
55818.36	105.36	14.45 (0.02)	13.91 (0.01)	13.74 (0.01)	NOT (NOTCAM)
55880.72	167.72	16.23 (0.01)	15.38 (0.01)	14.70 (0.01)	CA-3.5m (O2000)
55913.68	200.68	17.00 (0.01)	16.19 (0.02)	15.31 (0.02)	CA-3.5m (O2000)
55914.66	201.66	17.05 (0.01)	16.23 (0.02)	15.35 (0.02)	CA-3.5m (O2000)
55946.13	233.13	17.43 (0.02)	16.78 (0.02)	16.21 (0.02)	UKIRT (WFCAM)
55999.91	286.91	18.10 (0.02)	17.47 (0.02)	17.31 (0.02)	UKIRT (WFCAM)
56024.38	311.38	18.46 (0.03)	17.80 (0.03)	17.71 (0.04)	WHT (LIRIS)
56052.47	339.47	18.69 (0.02)	17.96 (0.02)	18.60 (0.03)	WHT (LIRIS)
56093.48	380.48	19.71 (0.06)	18.71 (0.06)	19.21 (0.08)	WHT (LIRIS)

Table 7. MIR Spitzer S_1 and S_2 magnitudes for SN 2011dh. Errors are given in parentheses. For completeness data for the first 100 days already published in E14a are included.

JD (+2400000)	Phase	3.6 μm	4.5 μm	Telescope (Instrument)
(d)	(d)	(mag)	(mag)	
55731.21	18.21	11.83 (0.02)	11.48 (0.02)	SPITZER (IRAC)
55737.06	24.06	11.66 (0.02)	11.31 (0.02)	SPITZER (IRAC)
55744.32	31.32	11.66 (0.02)	11.30 (0.02)	SPITZER (IRAC)
55751.46	38.46	11.68 (0.02)	11.30 (0.02)	SPITZER (IRAC)
55758.75	45.75	11.79 (0.02)	11.32 (0.02)	SPITZER (IRAC)
55766.45	53.45	11.96 (0.02)	11.34 (0.02)	SPITZER (IRAC)
55772.33	59.33	12.11 (0.03)	11.38 (0.02)	SPITZER (IRAC)
55779.12	66.12	12.30 (0.03)	11.43 (0.02)	SPITZER (IRAC)
55785.60	72.60	12.50 (0.03)	11.50 (0.02)	SPITZER (IRAC)
55798.28	85.28	12.84 (0.04)	11.66 (0.03)	SPITZER (IRAC)
55964.14	251.14	14.30 (0.00)	13.28 (0.00)	SPITZER (IRAC)
56026.63	313.63	15.54 (0.01)	14.28 (0.00)	SPITZER (IRAC)
56104.23	391.23	17.02 (0.01)	15.51 (0.00)	SPITZER (IRAC)
56136.41	423.41	17.34 (0.01)	15.99 (0.01)	SPITZER (IRAC)
56168.69	455.69	17.58 (0.01)	16.24 (0.01)	SPITZER (IRAC)
56337.59	624.59	18.52 (0.08)	17.54 (0.06)	SPITZER (IRAC)
56360.27	647.27	18.67 (0.05)	17.66 (0.03)	SPITZER (IRAC)
56477.83	764.83	18.83 (0.05)	18.05 (0.04)	SPITZER (IRAC)
56742.28	1029.28	...	18.51 (0.09)	SPITZER (IRAC)
56742.30	1029.30	...	18.41 (0.08)	SPITZER (IRAC)
56771.67	1058.67	18.86 (0.08)	18.54 (0.07)	SPITZER (IRAC)
56773.84	1060.84	...	18.36 (0.06)	SPITZER (IRAC)

Table 8. List of late-time (100-415 days) optical and NIR spectroscopic observations.

JD (+2400000)	Phase	Grism	Range	Resolution	Resolution	Telescope (Instrument)
(d)	(d)		(Å)		(Å)	
55821.33	108.33	b200	3300-8700	...	12.0	CA-2.2m (CAFOS)
55821.33	108.33	r200	6300-10500	...	12.0	CA-2.2m (CAFOS)
55828.35	115.35	R300B	3200-5300	...	4.1	WHT (ISIS)
55828.35	115.35	R158R	5300-10000	...	7.7	WHT (ISIS)
55830.25	117.25	Grism 4	3500-8450	613	...	AS 1.82m (AFOSC)
55830.28	117.28	Grism 2	3720-10200	241	...	AS 1.82m (AFOSC)
55835.25	122.25	Grism 4	3500-8450	613	...	AS 1.82m (AFOSC)
55864.65	151.65	Grism 4	3500-8450	613	...	AS 1.82m (AFOSC)
55867.71	154.71	g200	?-?	...	?	CA-2.2m (CAFOS)
55893.76	180.76	Grism 3	3200-6700	345	12.4	NOT (ALFOSC)
55897.76	184.76	Grism 5	5000-10250	415	16.8	NOT (ALFOSC)
55911.20	198.20	zJ	8900-15100	700	...	WHT (LIRIS)
55914.70	201.70	R300B	3200-5300	...	8.2	WHT (ISIS)
55914.70	201.70	R158R	5300-10000	...	15.4	WHT (ISIS)
55918.69	205.69	HK	14000-25000	333	...	TNG (NICS)
55951.64	238.64	Grism 4	3200-9100	355	16.2	NOT (ALFOSC)
55998.68	285.68	r200	6300-10500	...	12.0	CA-2.2m (CAFOS)
56005.63	292.63	Grism 4	3200-9100	355	16.2	NOT (ALFOSC)
56013.14	300.14	R600B	?-?	...	5.7	WHT (ISIS)
56013.14	300.14	R316R	?-?	...	3.0	WHT (ISIS)
56071.56	358.56	R500B	3440-7600	322	15.0	GTC (OSIRIS)
56072.61	359.61	R500R	4800-10000	352	20.8	GTC (OSIRIS)
56128.47	415.47	R300B	3600-7000	270	16.7	GTC (OSIRIS)

Table 9. Pseudo-bolometric 3-400 days UV to MIR lightcurve for SN 2011dh calculated from spectroscopic and photometric data with a 1-day sampling between 3 and 50 days and a 5-day sampling between 50 and 400 days. Random errors are given in the first parentheses and systematic lower and upper errors (arising from the distance and extinction) respectively in the second parentheses.

JD (+2400000) (d)	Phase (d)	L (log erg s^{-1})	JD (+2400000) (d)	Phase (d)	L (log erg s^{-1})
55717.00	4.00	41.464 (0.001) (0.098,0.186)	55823.00	110.00	41.244 (0.002) (0.094,0.164)
55718.00	5.00	41.552 (0.001) (0.097,0.181)	55828.00	115.00	41.204 (0.002) (0.094,0.164)
55719.00	6.00	41.653 (0.001) (0.097,0.179)	55833.00	120.00	41.163 (0.002) (0.094,0.164)
55720.00	7.00	41.747 (0.001) (0.097,0.178)	55838.00	125.00	41.121 (0.002) (0.094,0.164)
55721.00	8.00	41.835 (0.001) (0.097,0.178)	55843.00	130.00	41.078 (0.002) (0.094,0.164)
55722.00	9.00	41.909 (0.001) (0.097,0.178)	55848.00	135.00	41.033 (0.002) (0.094,0.165)
55723.00	10.00	41.969 (0.001) (0.097,0.177)	55853.00	140.00	40.990 (0.002) (0.094,0.165)
55724.00	11.00	42.018 (0.001) (0.097,0.176)	55858.00	145.00	40.948 (0.002) (0.094,0.165)
55725.00	12.00	42.057 (0.001) (0.097,0.176)	55863.00	150.00	40.906 (0.002) (0.094,0.165)
55726.00	13.00	42.089 (0.001) (0.096,0.175)	55868.00	155.00	40.863 (0.002) (0.094,0.165)
55727.00	14.00	42.117 (0.001) (0.096,0.174)	55873.00	160.00	40.818 (0.002) (0.094,0.165)
55728.00	15.00	42.142 (0.001) (0.096,0.174)	55878.00	165.00	40.773 (0.002) (0.094,0.164)
55729.00	16.00	42.163 (0.001) (0.096,0.173)	55883.00	170.00	40.728 (0.002) (0.094,0.164)
55730.00	17.00	42.182 (0.001) (0.096,0.173)	55888.00	175.00	40.683 (0.002) (0.094,0.164)
55731.00	18.00	42.197 (0.001) (0.096,0.173)	55893.00	180.00	40.639 (0.001) (0.094,0.164)
55732.00	19.00	42.208 (0.001) (0.096,0.172)	55898.00	185.00	40.597 (0.001) (0.094,0.164)
55733.00	20.00	42.214 (0.001) (0.096,0.172)	55903.00	190.00	40.555 (0.001) (0.094,0.164)
55734.00	21.00	42.215 (0.001) (0.096,0.171)	55908.00	195.00	40.516 (0.001) (0.094,0.164)
55735.00	22.00	42.211 (0.001) (0.095,0.171)	55913.00	200.00	40.477 (0.001) (0.094,0.164)
55736.00	23.00	42.200 (0.001) (0.095,0.170)	55918.00	205.00	40.438 (0.001) (0.094,0.164)
55737.00	24.00	42.184 (0.001) (0.095,0.168)	55923.00	210.00	40.403 (0.001) (0.094,0.164)
55738.00	25.00	42.164 (0.001) (0.095,0.167)	55928.00	215.00	40.368 (0.001) (0.094,0.164)
55739.00	26.00	42.141 (0.001) (0.094,0.166)	55933.00	220.00	40.334 (0.001) (0.094,0.164)
55740.00	27.00	42.116 (0.001) (0.094,0.165)	55938.00	225.00	40.300 (0.001) (0.094,0.164)
55741.00	28.00	42.090 (0.001) (0.094,0.164)	55943.00	230.00	40.267 (0.001) (0.094,0.164)
55742.00	29.00	42.064 (0.001) (0.094,0.163)	55948.00	235.00	40.235 (0.001) (0.094,0.163)
55743.00	30.00	42.039 (0.001) (0.094,0.162)	55953.00	240.00	40.204 (0.001) (0.094,0.163)
55744.00	31.00	42.016 (0.001) (0.093,0.162)	55958.00	245.00	40.172 (0.001) (0.094,0.163)
55745.00	32.00	41.995 (0.001) (0.093,0.161)	55963.00	250.00	40.139 (0.001) (0.094,0.163)
55746.00	33.00	41.976 (0.001) (0.093,0.161)	55968.00	255.00	40.106 (0.001) (0.094,0.163)
55747.00	34.00	41.959 (0.001) (0.093,0.160)	55973.00	260.00	40.072 (0.001) (0.094,0.163)
55748.00	35.00	41.942 (0.001) (0.093,0.160)	55978.00	265.00	40.039 (0.002) (0.094,0.163)
55749.00	36.00	41.927 (0.001) (0.093,0.160)	55983.00	270.00	40.005 (0.002) (0.094,0.163)
55750.00	37.00	41.913 (0.001) (0.093,0.159)	55988.00	275.00	39.972 (0.002) (0.094,0.163)
55751.00	38.00	41.899 (0.001) (0.093,0.159)	55993.00	280.00	39.939 (0.002) (0.094,0.163)
55752.00	39.00	41.885 (0.001) (0.093,0.159)	55998.00	285.00	39.906 (0.002) (0.094,0.163)
55753.00	40.00	41.873 (0.001) (0.093,0.159)	56003.00	290.00	39.872 (0.002) (0.094,0.163)
55754.00	41.00	41.859 (0.001) (0.093,0.159)	56008.00	295.00	39.838 (0.002) (0.094,0.163)
55755.00	42.00	41.846 (0.001) (0.093,0.159)	56013.00	300.00	39.804 (0.002) (0.094,0.163)
55756.00	43.00	41.834 (0.001) (0.093,0.159)	56018.00	305.00	39.770 (0.002) (0.094,0.163)
55757.00	44.00	41.822 (0.002) (0.093,0.159)	56023.00	310.00	39.737 (0.002) (0.094,0.163)
55758.00	45.00	41.811 (0.002) (0.093,0.159)	56028.00	315.00	39.703 (0.002) (0.094,0.163)
55759.00	46.00	41.800 (0.001) (0.093,0.159)	56033.00	320.00	39.670 (0.002) (0.094,0.163)
55760.00	47.00	41.790 (0.001) (0.093,0.159)	56038.00	325.00	39.638 (0.002) (0.094,0.163)
55761.00	48.00	41.781 (0.001) (0.093,0.159)	56043.00	330.00	39.605 (0.002) (0.094,0.163)
55762.00	49.00	41.771 (0.002) (0.093,0.159)	56048.00	335.00	39.572 (0.002) (0.094,0.163)
55763.00	50.00	41.762 (0.002) (0.093,0.159)	56053.00	340.00	39.540 (0.002) (0.094,0.163)
55768.00	55.00	41.715 (0.002) (0.093,0.159)	56058.00	345.00	39.508 (0.002) (0.094,0.163)
55773.00	60.00	41.669 (0.002) (0.093,0.159)	56063.00	350.00	39.476 (0.002) (0.094,0.163)
55778.00	65.00	41.627 (0.002) (0.093,0.160)	56068.00	355.00	39.445 (0.002) (0.094,0.163)
55783.00	70.00	41.585 (0.002) (0.093,0.160)	56073.00	360.00	39.413 (0.002) (0.094,0.163)
55788.00	75.00	41.544 (0.002) (0.093,0.161)	56078.00	365.00	39.382 (0.002) (0.094,0.163)
55793.00	80.00	41.501 (0.002) (0.093,0.162)	56083.00	370.00	39.351 (0.002) (0.094,0.163)
55798.00	85.00	41.458 (0.002) (0.094,0.162)	56088.00	375.00	39.320 (0.002) (0.094,0.163)
55803.00	90.00	41.415 (0.002) (0.094,0.162)	56093.00	380.00	39.289 (0.002) (0.094,0.163)
55808.00	95.00	41.372 (0.002) (0.094,0.163)	56098.00	385.00	39.255 (0.002) (0.094,0.163)
55813.00	100.00	41.330 (0.002) (0.094,0.163)	56103.00	390.00	39.220 (0.002) (0.094,0.163)
55818.00	105.00	41.287 (0.002) (0.094,0.163)	56108.00	395.00	39.186 (0.002) (0.094,0.164)